

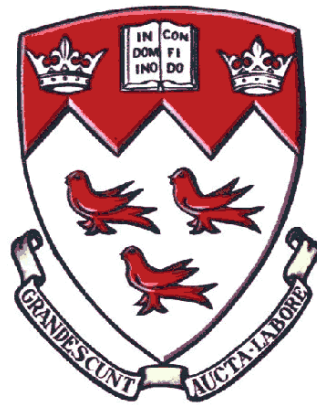
Bioinspired Design and Optimization of Materials for Dentures and Cellular Structures

Ammar Abdulkarim Alsheghri

Department of Mining and Materials Engineering

McGill University, Montreal, Quebec, Canada

November 2019



A thesis submitted to McGill University in partial fulfillment of the
requirements of the degree of Doctor of Philosophy

© A. A. Alsheghri 2019

For my parents.

Abstract

The remarkable and unique mechanical properties of natural structural designs have always been a source of inspiration for scientists to enhance material design. The integration of bioinspired design with topology optimization promises unprecedented possibilities in terms of improving the properties and functionalities of products. Recently, the advancement in additive manufacturing has enabled the sustainable and accurate fabrication of complex designs that were not possible a decade ago, which opened the door to implement and develop material design optimization methods.

Aiming to understand and enhance design optimization methods towards the advancement of sustainable product design, the present dissertation systematically examined various optimization techniques and their implementation in real-life applications with a focus on a bioinspired approach. The dissertation involves design optimization through both analytical modeling and finite element analysis (FEA). Uniaxial tension and compression experiments were conducted on additively manufactured specimens to validate the results obtained from the different investigated design optimization models.

The dissertation is manuscript-based containing three inherently connected articles (see the first page in chapters 3-5 for the interconnectivities). Chapter 3 covers design optimization through analytical modeling with a focus on optimizing the design of circumferential clasps in additively manufactured removable partial dentures. Chapter 4 presents bioinspired shape optimization with mesh adaptive direct search to improve strength and stiffness of metal/polymer interfaces in additively manufactured dental prostheses. Chapter 5 introduces an optimization framework for bioinspired topological design coupled with probability distribution models to generate the initial guess. Through this framework, bioinspired and optimized cellular structures

could be designed for various biomedical and engineering applications. The aforementioned studies offer new insights to leverage the potential of additive manufacturing and optimize the mechanical design of structures and interfaces.

Résumé

Les propriétés mécaniques remarquables et uniques des conceptions structurelles naturelles ont toujours été une source d'inspiration pour les scientifiques afin d'améliorer la conception des matériaux. L'intégration de la conception bioinspirée avec l'optimisation de la topologie promettent des possibilités sans précédent en termes d'amélioration des propriétés et des fonctionnalités des produits. Récemment, l'avancement de la fabrication additive a permis la fabrication durable et précise des conceptions complexes qui n'étaient pas possibles il y a une décennie, ce qui a ouvert la voie à la mise en œuvre et au développement de méthodes d'optimisation de la conception de matérielle.

Visant à comprendre et à améliorer les méthodes d'optimisation de la conception vers l'avancement de la conception de produits durables, la présente dissertation a systématiquement examiné diverses techniques d'optimisation et leur mise en œuvre dans des applications réelles en mettant l'accent sur une approche bioinspirée. La thèse comprend l'optimisation de la conception par la modélisation analytique et l'analyse par éléments finis (FEA). Des expériences de traction et de compression uni-axiales ont été menées sur des spécimens fabriqués additivement pour valider les résultats obtenus à partir des différents modèles d'optimisation de conception.

La thèse est basée sur un manuscrit contenant trois articles intrinsèquement liés (consultez la première page des chapitres 3-5 pour l'interconnectivité). Le chapitre 3 couvre l'optimisation de la conception à travers la modélisation analytique, en mettant l'accent sur l'optimisation de la conception des fermoirs circonférentiels dans les prothèses fabriquées de manière additive. Le chapitre 4 présente l'optimisation de forme bioinspirée avec une recherche directe d'engrenage adaptative pour améliorer la résistance et la rigidité des interfaces métal / polymère dans les prothèses dentaires fabriquées de façon additive. Le chapitre 5 présente un cadre d'optimisation

itératif pour la conception topologique bioinspirée, associé à des modèles de distribution de probabilité pour générer la supposition initiale. Grâce à ce cadre, des structures cellulaires bioinspirées et optimisées pourrait être conçu pour diverses applications d'ingénierie. Les études susmentionnées offrent des nouvelles idées pour tirer parti du potentiel de la fabrication additive et optimiser la conception mécanique des structures et des interfaces.

Acknowledgement

My Lord increase me in knowledge. I would first and foremost thank him, the most merciful and the most compassionate. The One who supplied me with the persistence to heal, wisdom to deal with many challenges during my PhD studies, and patience to complete this dissertation.

I am very grateful for my supervisor, Prof. Jun Song, for his invaluable guidance and support. His initial trust allowed me to take many risks and independent steps and truly make the dissertation my own. It was fun to work under his supervision and I learned from his knowledge, kindness, and high manners. I'm also especially thankful for the internship opportunity he allowed me to pursue which enabled me to collaborate with industry. I am also grateful for my co-supervisor Prof. Faleh Tamimi Marino who has been always supportive and available to discuss any challenges in life and research. I also learned from him to be humble and to aim to do my task in the best possible way. I learned from him to be optimistic, to simplify research problems, and to always remain up-to-date with recent scientific trends.

I would like to thank Dr. Natalie Reznikov for all the time and effort she made towards the success of the bone-inspired topological optimization component of this dissertation. Through the many discussions and meetings, she significantly contributed to the success of this project. I would like to thank Object Research Systems (ORS) family particularly Dr. Nicolas Piche, Dr. Mathieu Gendron, and Catherine Desrosiers for their help and support in image processing and graph analysis. I would like also to thank Prof. Marc D McKee for his support in coordinating funding and 3D printing of the bone-inspired lattice structures. I am also thankful for 3DRPD Inc. – Denis Theriault, Eric Fort, and Eric Caron – for their support related to 3D printing and designing removable partial dentures.

I'd like to thank members of the Song and Tamimi laboratories: Dr. Alaa Mansour, Dr. Omar Alageel, Dr. Amir El-Hadad, Hanan Mousa, Dr. Faez Al-Hamed, Rohan Chakrabarty, Dr. Ovidiu Ciobanu, Dr. Mohamed Amine Mezour, Qiman Gao, Dr. Yara Oweis, Dr. Iskandar Tamimi, and all who attended my practice sessions. I'd like also to thank Binhan Sun for his support with tensile testing

I'm extremely thankful for Barbara Hanley who answered thousands of my questions. I'd like to thank the numerous funding sources over the course of my PhD: The McGill Engineering Doctoral Award (MEDA), Fonds de recherche du Québec (FQRNT) – Bourses de doctorat en recherche, Graduate Research Excellence Award, Graduate Research Enhancement and Travel Award (GREAT), and Natural Sciences and Engineering Research Council (NSERC) Engage.

Furthermore, there were people who encouraged me to pursue PhD studies. My previous supervisor Prof. Rashid Abu Al-Rub who has been a great influencer and my undergraduate professors from Khalifa University of Science and Technology. In addition, I would like to thank my relatives. I will always remember the words of my grandfather Omar “put your goal in front of you and go directly to it”.

Most of all, I'd like to thank my wife Mounesa for the huge amount of support and patience during my studies. I'd also like to thank my brothers Bashar and Youssef and my sister Bushra for their steadfast support and encouragement. This dissertation is dedicated to my parents who have given me every opportunity to succeed in life. To my mother Dr. Sahar, who early-on planted in me the importance of knowledge, nutrition and persistence and to my father Eng. Abdulkarim who taught me not to be overwhelmed with being the first or the best, but to be contented and successful.

Contents

Abstract.....	i
Résumé.....	iii
Acknowledgement	v
Contents	vii
List of Figures.....	x
List of Tables	xv
Glossary of Abbreviations and Symbols.....	xvi
Contributions to Original Knowledge.....	xvii
Contribution of Authors.....	xix
1 General Introduction.....	1
2 Literature Review	5
2.1 Design Optimization	5
2.1.1 Gradient-based design optimization	5
2.1.2 Bioinspired design optimization (non-gradient-based).....	6
2.1.3 Trabecular bone as a marvel for bioinspired design	8
2.1.4 Continuum versus discrete design optimization	10
2.2 Cellular and Lattice Structures.....	12
2.3 Additive Manufacturing	15
2.4 Removable Partial Dentures (RPDs).....	16
2.4.1 Denture clasp	17
2.4.2 Acrylic/metal interface in dental prostheses	19
2.5 Failure Theories.....	22
2.5.1 Maximum Normal Stress Theory.....	22
2.5.2 Von Mises Stress and Maximum-Distortion-Energy Criterion	22
2.6 Finite Element analysis (FEA).....	23
3 Analytical Modeling for Optimization	26
3.1 Introduction	30
3.2 Materials and methods	32
3.2.1 Analytical model.....	33

3.2.2	FEA.....	36
3.2.3	Experimental Validation of Analytical Model.....	37
3.3	Results.....	38
3.3.1	Analytical model.....	38
3.3.2	FEA.....	41
3.3.3	Experimental Validation of Analytical Model.....	42
3.4	Discussion.....	43
3.5	Conclusion.....	46
3.6	Supplementary Material.....	46
3.6.1	Retention Force model.....	46
3.6.2	Relation between retention force, spring force and coefficient of friction.....	50
3.6.3	Mesh sensitivity analysis.....	50
3.6.4	Experimental validation of the analytical model.....	51
4	Shape Optimization.....	53
4.1	Introduction.....	56
4.2	Materials and Methods.....	58
4.2.1	2D FEA.....	58
4.2.2	Optimization procedures.....	59
4.2.3	3D FEA.....	60
4.2.4	Sample Preparation.....	61
4.2.5	Mechanical Testing.....	62
4.2.6	Surface Analysis.....	64
4.3	Statistical Methods.....	64
4.4	Results.....	64
4.4.1	Optimization and 2D FEA.....	64
4.4.2	Experimental Results.....	66
4.4.3	3D FEA.....	68
4.5	Discussion.....	71
4.6	Conclusion.....	75
4.7	Supplementary Material.....	76
4.7.1	Shape Optimization using Stress-Induced Material Transformation.....	76

4.7.2	Mesh adaptive direct search (MADS) optimization algorithm.....	78
4.7.3	General XPS survey spectra of control Co-Cr samples.....	79
4.7.4	Tensile experiments on Co-Cr/PMMA samples.....	80
5	Topology Optimization of Lattice Structures.....	84
5.1	Introduction.....	88
5.2	Methodology.....	95
5.2.1	General principle of iterative topological optimization and validation.....	95
5.2.2	CDC – a topological metric used for comparison of the reference lattice and biomimetic lattices at different stages of optimization.....	97
5.3	Results.....	97
5.3.1	Numerical reproducibility of the natural iterative topological refinement: Trade-off between mechanical stability (modulus) and architectural complexity.....	97
5.3.2	Independence of topological optimization on the directionality of loading, the exact coordinates of the nodes, and on the size of the lattice.....	100
5.3.3	Feasibility of additive manufacturing of topologically optimized lattices and the effect of manufacturing method and scale on the preservation of the observed numerical trends.....	103
5.4	Discussion.....	107
5.5	Conclusions.....	111
5.6	Supplementary Materials.....	112
5.6.1	Detailed methods.....	112
5.6.2	Sensitivity study on the effect of the optimization increment size.....	125
6	General Discussion.....	127
7	Conclusions and Future Perspectives.....	131
7.1	Conclusions.....	131
7.2	Future perspectives.....	132
8	Appendices.....	134
8.1	Appendix A: MATLAB and Abaqus UMAT codes for shape optimizing using Finite Element Analysis in Chapter 4.....	134
8.2	Appendix B: MATLAB function files used for MADS in Chapter 4.....	143
9	References.....	148

List of Figures

Figure 1-1: Ashby’s chart of Young’s modulus versus density .	3
Figure 2-1: Variation and anisotropy of trabecular bone texture within one bone specimen (human proximal femur). Morphological features such as trabecular size, alignment, plate- or rod-like shape, and coarseness of the fabric, all reflect the local adaptation of the tissue to local loading, the adaptation being governed by bone cells and implemented at the micrometer level. Scale bar refers to all circular insets .	10
Figure 2-2: Deformation behavior of strut-based lattice structures at different strains ϵ [59].	14
Figure 2-3: (Left) the mandibular partially edentulous arch before treatment. (Middle): the mandibular framework for the removable partial denture and its components of A: major connector; B: minor connector; C: rests; D: direct retainer; E: indirect retainer. (Right) the removable partial denture (RPD) on the edentulous arch.	16
Figure 2-4: I-bar clasps engaging on teeth in a mechanical retention experiment [105].	19
Figure 3-1: Schematic of a circumferential clasp showing the forces experienced by the clasp cross-section while being disengaged from the undercut.	33
Figure 3-2: Schematic of a circumferential clasp approximated as a curved beam extending from point A at the clasp shoulder to point B at the clasp tip, with the relevant variables illustrated.	36
Figure 3-3: Photographs showing (a) Dentoform teeth model and laser-sintered clasps; (b) measurement of retention forces using a universal testing machine (MTS, Eden Prairie, MN). Note that only circumferential clasps on molar and premolar teeth were considered in this study.	38
Figure 3-4: Retention force F_R versus tilt angle θ for a series of friction coefficients μ .	39
Figure 3-5: Design charts for laser-sintered Co-Cr clasps with a semicircular cross-section showing relation between clasp length and radius of cross-section with (a) stress and undercut for a molar; (b) stress and undercut for a premolar; (c) undercut and retention force for a molar; (d) undercut and retention force for a premolar. The solid green, yellow dashed and black short dashed lines correspond to the undercut in (a) and (b), and to the retention force in (c) and (d).	41
Figure 3-6: FEA of a circumferential laser-sintered Co-Cr clasp for a premolar with semicircular cross-section showing (a) Tensile stress [MPa]; and (b) Deflection [mm] in the x’-direction.	42
Figure 3-7: Experimental validation of the analytical model showing measured retention force versus predicted retention force. The dashed line indicates when the measured force equals the model predicted one, while the symbols denote the retention forces on different teeth.	43
Figure 3-8: Retention force F_R versus spring/stiffness force F_S for a series of friction coefficients μ .	50
Figure 3-9: Mesh sensitivity analysis for clasp FE model showing convergence of von Mises stress after 50 elements.	51

Figure 4-1: Co-Cr/PMMA interlocking feature design inspired by (a) shape optimization through stress-induced material transformation (SMT), which looks similar to a branch of (b) mangrove prop roots, (c) 2D Y-shape geometry with design variables and boundary conditions, (d) 3D geometry with design variables, (e) digital microscope image of additively manufactured specimen using laser-sintering, and (f) SEM image of the feature cross-sectional area. 59

Figure 4-2: 2D FEA parametric study showing the effect of geometry on (a,c, & e) maximum von Mises stress in metal (solid line) and peak maximum principal stress in polymer (dotted line); and (b, d & f) stiffness of the structure (solid line) and polymer displacement at metal/polymer interface (dotted line): (a & b) effect of θ at $T = 0.55$ mm & $L = 1.8$ mm; (c & d) effect of L at $T = 0.55$ mm & $\theta = 76^\circ$; (e & f) effect of T at $\theta = 76^\circ$ & $L = 1.8$ mm. 66

Figure 4-3: Effect of (a) features' neck height (H) at $S = 1$ mm & $A = 0.09$ mm²; (b) spacing between features (S) at $H = 1$ mm & $A = 0.09$ mm²; and (c) feature's cross-sectional area (A) at $S = 0.09$ mm & $H = 1$ mm on experimental tensile nominal strength [MPa] of the Co-Cr/PMMA specimen. 67

Figure 4-4: Comparison between experimental (a) stiffness, (b) toughness and (c) tensile strength of PMMA, control specimen, Y interlock (A2S09H10), and bead designs with one-way analysis of variance (ANOVA) and Tukey HSD multiple comparison at significance level of $p < 0.05$; and (d) displacement of PMMA at interface generated by FEA for Y interlock (A2S09H10) and bead designs..... 68

Figure 4-5: Stereo microscope images for fracture surfaces of tensile specimens: (a) interlocking feature design A2H10S09 and (b) Bead design..... 69

Figure 4-6: Stereo microscope images of (a) bead design and (b) interlocking features A2H10S09 design; with 3D FEA showing the contours of (c & d) maximum principal stress in PMMA, (e & f) displacement contours, and (g & h) von Mises stress in Co-Cr..... 70

Figure 4-7: Results of 3D FEA showing the effect of interlocking features' neck height (H), spacing (S), and cross-sectional area (A) on (a, d & h) von Mises stress in metal; (b, e & h) stiffness; and (c, f & i) PMMA displacement at the interface of the Co-Cr/PMMA specimen. The considered design values were $S = 1$ mm and $A = 0.09$ mm² for (a, b & c); $H = 1$ mm and $A = 0.09$ mm² for (d, e & f); $H = 1$ mm and $S = 0.9$ mm for (g, h & i). 70

Figure 4-8: Comparison between stiffness values obtained from experiments with the ones calculated using 3D FEA. (a) Height (H) is varied at $S = 1$ mm & $A = 0.09$ mm²; (b) spacing between features (S) is varied at $H = 1$ mm & $A = 0.09$ mm²; (c) feature's cross-sectional area (A) is varied at $S = 0.09$ mm & $H = 1$ mm; (d) all data are considered. 71

Figure 4-9: (a) Initial geometry of a retention feature with loading (10 mm/min) and boundary conditions, where green represents Co-Cr with $E_{Co - Cr} = 200$ GPa and white represents PMMA with $E_{PMMA} = 2.4$ GPa. (b) Results of the shape optimization simulation model after 3 iterations, where red represents Co-Cr, blue represents PMMA, and green represents a modulus greater than E_{PMMA} and less than $E_{Co - Cr}$. (c) Results after 10 iterations. (d) Optimized shape after 36 iterations. 77

Figure 4-10: Performance History of the mesh adaptive direct search (MADS) optimization algorithm showing the objective function value (1/stiffness) versus the number of function evaluations. 78

Figure 4-11: General XPS survey spectra and surface elemental composition of control Co-Cr sample. 79

Figure 4-12: Experimental set-up of Co-Cr/PMMA sample’s tensile test. 80

Figure 4-13: Experimental load-displacement curves of interlocking feature design groups showing the effects of (a) Height (H) at $S = 1 \text{ mm}$ and $A = 0.09 \text{ mm}^2$; (b) feature's cross-section area (A) at $S = 0.09 \text{ mm}$ and $H = 1 \text{ mm}$; and (c) spacing between features (S) at $H = 1 \text{ mm}$ and $A = 0.09 \text{ mm}^2$ 81

Figure 4-14: Comparison between experimental tensile strength [MPa] of interlocking feature groups showing effect of (a) feature’s cross-section area; (b) spacing between features; (c) feature’s neck height, with one-way analysis of variance (ANOVA) and Tukey HSD multiple comparison at significance level of $p < 0.05$ 82

Figure 5-1: Bioinspired design and topological optimization – a general principle. (A) μ CT reconstruction of a human proximal femur. (B) Graph of trabecular bone (highlighted in blue in A) and (C) reference lattice. (D) Cloud of nodes from a graph of trabecular bone is reproduced using a probability distribution function, D' . The nodes are connected using a 3D Voronoi tessellation (E) to form a biomimetic lattice (F). The biomimetic lattice enters the optimization loop and generates three optimized lattices (G-I). All lattices are topologically analyzed in terms of the node connectedness decay coefficient, CDC (insets in C, and F-I)..... 95

Figure 5-2: Topological design iterative optimization; uniaxial compression. (A) While all mature trabecular bone lattices have remarkably similar CDC, the bioinspired naïve lattice starts with the higher CDC and approximates the reference CDC values in the process of iterative pruning. (B) The normalized elastic modulus first increases in a nonlinear fashion reaching the maximum in the optimized lattice Generation 1. Further iterations of element pruning result in a nearly linear decrease of the normalized modulus to the value of the reference lattice and lower. (C) Maximal von Mises stress values slowly increase in the process of iterative optimization, but the dramatic increase of the von Mises criterion occurs only when CDC drops beyond the reference lattice value and the optimized Generation 3 value. (D) Dependence between the normalized apparent modulus and the proportion of bend-dominated elements. 99

Figure 5-3: Topological design iterative optimization: triaxial compression. (A) The number of elements decreases with the optimization iterations. (B) Normalized bulk modulus follows a similar trajectory as the normalized elastic modulus in uniaxial compression (see Fig. 2B). (C) Increase in maximal von Mises stress with optimization, and (D) increase in proportion of bend-dominated elements (both panels C and D indicate that the optimized lattices have more homogeneous distribution of stresses). 101

Figure 5-4: Repeated iterative optimization using different populations of nodes of the same overall volume (generated using the same probability distribution function). (A) Normalized bulk

modulus versus CDC. (B) Normalized maximal von Mises stress versus CDC. (C) Normalized bulk modulus versus the proportion of bend-dominated elements.	102
Figure 5-5: Comparison of the optimization trajectories (uniaxial optimization) of biomimetic lattices designed at 2 different 3D sizes, using the different populations of nodes of the same mean density but different volumes. Note the same shape of the optimization trajectories.	103
Figure 5-6: Biomimetic lattice 3D rendering. (A) Surface mesh file used for 3D printing. (B) Micro-CT reconstruction of the 3D printed lattice. (C) Superimposition of the designed and manufactured lattices.	104
Figure 5-7: Comparison of experimentally measured and numerically predicted properties of the lattices printed at two different scales, 5 mm and 20 mm. (A) Measured and predicted mass for 5 mm lattice. (B) Measured and predicted mass for 20 mm lattice. (C) Measured and predicted stiffness for 5 mm lattice (linear fit revealed $stiffness_{measured} = stiffness_{predicted} - 3.3 N/mm$, with R-squared value of 0.99). (D) Measured and predicted stiffness for 20 mm lattice. Note the broader error bars for measured stiffness of 5 mm lattices (C) in comparison with the stiffness values of the 20 mm lattices (D).....	105
Figure 5-8: Framework of the bioinspired topological design; (a) natural material scan (i.e. femoral head of trabecular bone), (b) graph generation, (c) biomimetic node population, (d) Voronoi tessellation for biomimetic nodes, and (e) element generation for naïve lattice.	114
Figure 5-9: Comparison between the probability distribution functions of the radial coordinates obtained from (a) reference and (b) biomimetic naïve lattices showing agreement.	115
Figure 5-10: (a) Distribution of nodes from the reference cube compared with (b) distribution of nodes from the inscribed naïve biomimetic cube.	115
Figure 5-11: Histograms during the node generation process. Comparison between the spherical coordinates' distribution of the nodes from reference bone lattice (on the left) and naïve biomimetic lattice (on the right). (a & b) histograms showing count of spherical coordinate phi – units in Rad; (c & d) histograms showing count of spherical coordinate theta – units in Rad; (e & f) histograms showing count of spherical coordinate R.....	116
Figure 5-12: 2D representation of optimization procedure; after nodes are generated and connected by edges, the iterative optimization procedure starts with subjecting the naïve structure to a compressive loading using FEA. In each iteration the elements with the minimum equivalent stress were removed and a supporting element was inserted to strengthen regions of high stress and alleviate hot spots in the structure following the concept of triangulation with relatively short elements.	120
Figure 5-13: Augmentation of elements through the concept of triangulation: A new element is added between nodes A and C to support the highly stressed element AB forming triangle ABC.	121
Figure 5-14: Relationship between node type based on the number of neighbours and the connectedness decay coefficient of the abundance of each node type. The black curve represents	

an exponential decay with a positive decay coefficient whereas the red curve represents an exponential decay with a negative decay coefficient..... 121

Figure 5-15: Compressive loading of Contours of triaxial compression during topology optimization showing contours of maximum von Mises stress in [MPa] generated through finite element analysis for the biomimetic OptGen2 indicating uniform stress distribution, with black arrows indicating the direction of applied compressive displacements on the loading surfaces. Note that surfaces opposite to the loading surfaces were fixed in the direction of the compressive displacements..... 122

Figure 5-16: Normalized modulus versus volume fraction for (a) uniaxial-based optimization; (b) triaxial-based optimization..... 122

Figure 5-17: Generation of stereolithography (STL) mesh files for synthetic graphs (DragonflyTM, Object Research Systems, Montreal, QC, Canada). (a) Biomimetic graph; (b) every edge in the graph is replaced with a segment of one-voxel thick (voxel representation of a graph); (c) STL mesh file obtained from the voxel representation. 124

Figure 5-18: (a) images of 3D printed biomimetic lattices with different sizes; (b) image of scaled and 3D printed OptGen3 biomimetic lattice; (c) image of scaled and 3D printed reference lattice. 124

Figure 5-19: load-displacement curves for uniaxial compression of reference and biomimetic lattices generated from uniaxial-based optimization. 125

Figure 5-20: load-displacement curves for uniaxial compression of reference and biomimetic lattices generated from triaxial-based optimization. 125

List of Tables

Table 3-1: Values used for experimental validation of the analytical model.	51
Table 3-2: Measured and predicted retention forces for different tooth types.	52
Table 4-1: Design variables' values for each considered design group.....	63
Table 4-2: General XPS survey spectra of control Co-Cr samples	79
Table 4-3: Experimental tensile strength [MPa] of design groups	83
Table 5-1: Experimental results for uniaxial compression testing of reference and biomimetic lattices derived from uniaxial optimization.	106
Table 5-2: Experimental results for uniaxial compression testing of scaled reference and biomimetic lattices derived from uniaxial optimization	106
Table 5-3: Experimental results for uniaxial compression testing of scaled reference and biomimetic lattices derived from triaxial optimization.....	107
Table 5-4: The effect of number of elements to remove each iteration and the element removal increment on the speed of optimization and mechanical properties of the synthetic lattice.....	126

Glossary of Abbreviations and Symbols

FEA	Finite element analysis
3D	Three-dimensional
σ	Normal stress
τ	Shear stress
AM	Additive manufacturing
CAD	Computer-aided design
SMT	Stress-induced material transformation
RPDs	Removable partial dentures
MADS	Mesh adaptive direct search
Co-Cr	Cobalt-chromium
PMMA	Poly(methyl methacrylate)
CAM	Computer-aided-manufacturing
XPS	X-ray photoelectron spectroscopy
SKO	Soft killed option
SIMP	Solid isotropic material with penalization method
CDC	Connectedness decay coefficient
SLS	Selective laser-sintering
ROI	Region of interest
CT	Computed tomography
SEM	Scanning electron microscope
DMLS	Direct metal laser-sintering
STL	Stereolithography

Contributions to Original Knowledge

Recent advances in additive manufacturing (AM) enabled fabrication of complex and customized components. This has led to a progress in material design to accommodate geometrical design complexities. However, it is still required to unleash the full potential of AM through improving the design methodology. This dissertation explores various methodologies for structural design optimization of materials for different engineering applications. Chapter 3 introduced for the first time a closed-form analytical model for design optimization of circumferential clasps for removable partial dentures to avoid their plastic deformation or fatigue failure. The model enables the customized design of clasps to accommodate different materials as well as patient-specific tooth anatomy. It was demonstrated through the proposed optimization model that additively manufactured clasps – through selective laser sintering – could be placed safely in molar teeth, whereas they are susceptible to failure in premolars.

Chapter 4 highlights for the first time a coupling between biomimetic shape optimization based on stress analysis and mesh adaptive direct search (MADS) algorithm to reach optimal interlocking designs for enhancing the mechanical properties of metal/polymer interfaces in biomedical and dental prostheses. The ability to fabricate such bioinspired interlocking designs by commercial additive manufacturing techniques (i.e. selective laser sintering) was successfully demonstrated. It was an interesting finding that the bioinspired shape optimization technique suggested a Y-shaped interlocking feature design similar to the roots of mangrove trees.

While design optimization in Chapter 4 was concerned with overall morphology of objects (i.e. continuum approach), Chapter 5 focused on optimization of the topology of lattice structures, regardless of the thickness or cross-sectional shape of the struts. This approach aims at improvement of mechanical properties of structures by changing the connectivity of elements

without changing the material quality and quantity. The obtained lattice structures are scalable to serve various real-life engineering and biomedical applications.

Traditionally, in topology design optimization, the initial guess is provided as a uniform or random material distribution in the design space [1]. Chapter 5 proposes a novel start strategy based on distributing the material initially in the design space using a probability distribution function extracted from the distribution of material in a close-to-optimal design (such as a bioinspired natural design). This process could be automated for any shape by using probability distribution models. As a result, the iterative optimization procedure will be accelerated because convergence to good solutions is traditionally associated with large number of iterations. Hence, the proposed modification will enhance the efficiency and speed of topology optimization methods making the procedure more attractive for industrial real-life application.

Finally, the proposed bioinspired topological optimization method in Chapter 5 does not depend on the periodically-repeating unit cell approach [2, 3]. It offers a stochastic 3D cellular design independent of a unit cell building block allowing a customized control of anisotropy based on the direction of anticipated loading while offering a scalable design integrating stiffness with porosity.

Contribution of Authors

To all the co-authors, I am appreciative of your hard work that contributed to some manuscripts in this thesis. Following is the contribution of co-authors for each manuscript of this thesis.

First manuscript: “An analytical model to design circumferential clasps for laser-sintered removable partial dentures”

Ammar Alsheghri: Proposed the idea, developed the analytical model, performed the finite element analysis, and wrote the manuscript. Omar Alageel: Conducted with Ammar pullout experiments to measure retention forces of clasps. Ovidiu Ciobanu: Prepared some figures, discussed ideas for introduction and discussion, and revised the paper. Eric Caron: Designed and 3D printed the removable partial dentures (RPDs) used in the study. Jun Song and Faleh Tamimi: Assisted in the design of the workflow, discussed methodology and results, edited the manuscript and supervised the project.

Second manuscript: “Bioinspired and optimized interlocking features for strengthening metal/polymer interfaces in additively manufactured prostheses”

Ammar Alsheghri: Proposed the idea, wrote the bioinspired shape optimization algorithm, conducted finite element analysis and experimental testing, and wrote the manuscript. Omar Alageel and Mohamed Amine Mezour: Prepared the experimental samples and edited the paper. Stephen Yue and Binhan Sun: Helped with conducting experimental tensile testing and edited the manuscript. Jun Song and Faleh Tamimi: Assisted in the design of the workflow, discussed methodology and results, edited and manuscript and supervised the project.

Third manuscript: “Topological optimization of 3D lattice structures for bioinspired engineering of stiff and lightweight materials”

Ammar Alsheghri: Conceptualization, Data curation, Formal analysis, Investigation, Methodology, Resources, Software, Validation, Writing - original draft, Writing - review & editing. Natalie Reznikov: Conceptualization, Funding acquisition, Investigation, Methodology, Resources, Validation, Visualization, Writing - original draft, Writing - review & editing. Nicolas Piché: Funding acquisition, Methodology, Resources, Software, Supervision, Writing - review & editing. Marc D. McKee: Funding acquisition, Project administration, Resources, Writing - review & editing. Faleh Tamimi: Funding acquisition, Investigation, Supervision, Writing - review & editing. Jun Song: Funding acquisition, Investigation, Methodology, Resources, Supervision, Writing - review & editing.

1 General Introduction

Bioinspired design is perhaps one of the oldest design methodologies with examples from all over the architectural history [4]. It is neither a coincidence that the body shape of a duck looks like the external shape of a ship nor that airplanes have tails and wings as birds do. Engineers have increasingly been learning from natural architectures so that a variety of structures were built based on bioinspired designs and mechanical principles. An example of such bioinspiration could be found in bridges such as the Butterfly bridge in Bedford UK, which has twin inclined steel arches as a supporting system inspired from butterfly wings [4]. Another example is ductile and flaw-tolerant brick-and-mortar designs composed of sub-micrometer-thick ceramic platelets and ductile polymer matrix inspired by natural biomineralized tissues such as nacre, bone and tooth [5, 6]. Further advances in the area of bioinspired design will eventually lead to optimized materials and structures with unprecedented mechanical properties.

Advances in material design have been accompanied by a progress in computer-aided-manufacturing (CAM) to accommodate geometrical design complexities. For instance, additive manufacturing (AM) or 3D printing has revolutionized production in various industrial markets over the last ten years including aerospace, structural and biomedical businesses [7-9]. It has been replacing conventional manufacturing in several fields due to its higher accuracy allowing the manufacturing of complex designs and fine geometrical details as well as better sustainability due to its lower buy-to-fly ratio - the mass of raw material needed per unit mass of finished product [7]. For example, AM was utilized to reduce the mass of several aircraft components such as seat buckles, hinges, and brackets [7]. It has been adopted to provide high-strength porous prostheses for load-bearing orthopedic applications [8], to print ceramic and metallic constructs for crowns and bridges in dentistry [9], and even to produce concrete for construction industry [10]. However,

product design has been achieved through traditional computer-aided-design (CAD) to accommodate conventional manufacturing technologies, which limits the potential of AM. The major economic potential of AM could be leveraged by redesigning products and equipment based on this technology [11]. As AM becomes more dominant, design should focus more on functional optimization and less on manufacturability constraints [11]. Advances in design optimization will further the development of lightweight structures with enhanced functionality and mechanical properties.

The demand for lightweight and stiff materials has led to the development and advancement of the material design and optimization field. A commonly known simple example is the material selection charts developed by Ashby and Cebon [12], which offered design guidelines for optimal properties from the physical and mechanical aspects (see Figure 1-1). In orthopedics, similar design maps have been used to relate mechanical and morphological characteristics and derive tailored micro-architecture of porous solids to satisfy the stringent design functions in load-bearing bone replacement implants [13]. Further advancements in material design optimization involved an iterative natural adaptation process of development of an initial design until reaching an optimal design with uniform stress distribution within its structural elements [14-16]. However, there is still a need in industry to innovate new optimization techniques that could yield better structures especially for reducing weight while maintaining a good combination of mechanical properties. This need is always supported by the fact that scientists continue to discover new techniques and strategies in nature for material design optimization [17].

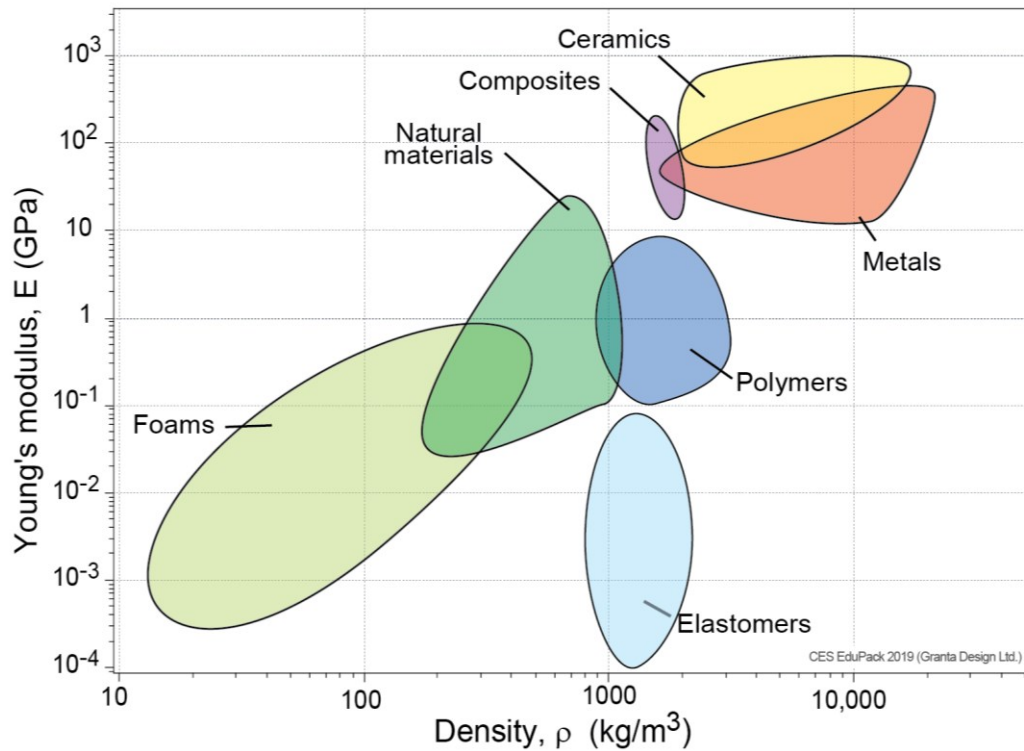


Figure 1-1: Ashby's chart of Young's modulus versus density ¹.

This dissertation aims to provide applications of some existing material design optimization techniques with a focus on reducing weight while keeping an acceptable and/or uniform level of stress within a structure. It involves design optimization through analytical modeling and stress-induced material transformation (i.e. shape optimization) coupled for the first time with mesh adaptive direct search algorithm. Then, it introduces a relatively new concept of bioinspired design optimization for lattice structures, which involves predicting the initial design based on mimicking the internal architecture of biological materials and then evolving the design iteratively - with bioinspired constraints - until reaching an optimal solution. The new bioinspired concept is based

¹ Chart created using CES EduPack 2019, ANSYS Granta © 2020 Granta Design

on the structural topology rather than shape or morphology. This concept was implemented in this dissertation to generate optimized scalable lattice structures for general engineering applications.

2 Literature Review

2.1 Design Optimization

Optimization is a very common procedure in engineering. It targets searching for the best possible solution for a given problem [18]. Structural design optimization is the careful distribution of material in space to yield an optimum outcome [19]. The desirable outcome could be to decrease stress, increase stiffness, reduce weight, etc. It provides engineers an initial but efficient layout of materials, optimized with respect to the functional specifications and surrounding conditions [1, 20]. Different terminologies have been used to refer to this concept such as layout optimization [15], shape optimization [21], and topology optimization [19, 22]. Topology optimization is probably the most common term of structural design optimization [1, 19, 20, 22-26]. Through this method, over-loaded regions within the design space are strengthened by adding materials whereas under-loaded regions are weakened by removing materials. Hence, topology optimization provides the best and optimal distribution of material in the design space that will satisfy the design requirements and constraints. Topology optimization algorithms could be grouped into gradient-based (i.e. deterministic) or non-gradient-based (such as bioinspired stochastic optimization) categories based on the procedure used to reach the optimal solution [18, 24].

2.1.1 *Gradient-based design optimization*

The most popular gradient-based design/topology optimization method in terms of research effort and implementation is the Solid Isotropic Material with Penalization method (SIMP) that was proposed by the seminal work of Bendsøe [24]. SIMP topology optimization incorporates an iterative analysis and design update steps to search for the optimal design [1]. The goal of this search is to find the optimal material distribution that minimizes an objective function (i.e. the compliance of the structure in most cases, which is the reciprocal of stiffness) subject to multiple

constraints. SIMP discretizes a design space into finite elements. Every element is assigned a relative density value that ranges between 0 and 1 such that 0 represents void (i.e. no material) and 1 represents completely solid. The elastic modulus of each element is related to its density using a penalization factor such that $E_e = \rho_e^p E_0$ to diminish the contribution of elements with intermediate densities, where ρ_e is the density of element e , p is the penalty value usually set to 3, and E_0 is the elastic modulus of solid material [1]. Then, the iterative optimization procedure starts by constructing the global stiffness matrix of the structure, obtaining the displacements at nodes, calculating the compliance and its derivatives with respect to each design variable, and performing optimization to update the design variables [1]. The optimization scheme is performed through optimality criteria methods [27] or the Method of Moving Asymptotes [28]. More details on the SIMP method are provided in [24].

Traditionally, the initial guess is achieved following a uniform distribution with the density of each core element equal to the maximum allowable average volume density, which might cause the final solution to converge to a local optimum and eliminates the possibility of exploring the global optimum [1]. Among other challenges and limitations of gradient-based topology optimization methods such as SIMP, that limited its application in industry, is the dependence of convergence on the mesh discretization of the design space; a challenge that has received little attention in the past [20]. Furthermore, convergence to good solutions is traditionally associated with large number of iterations.

2.1.2 Bioinspired design optimization (non-gradient-based)

When the problem size increases, a high computational cost is needed causing sometimes failure of a deterministic optimization algorithm [18]. This has led to emergence of the bioinspired optimization field in an attempt to find the fittest solution with an acceptable computational cost

[18]. Scientists have observed how various components in nature manage to find the optimal strategy while accounting for the different and sophisticated surrounding conditions. Therefore, bioinspired optimization focuses on mimicking natural structures for a wide range of applications such as biomedical engineering, robotics, nanotechnology, structural engineering, and *etc.* [18]. The two most predominant and successful categories of bioinspired optimization are evolutionary algorithms and swarm-based algorithms. Evolutionary algorithms take advantage of the natural and genetic adaptation which consists of an iterative process of development, reproduction, selection, and survival [18]. It starts with an initial solution that evolves iteratively towards the optimal solution [18]. On the other hand, swarm-based algorithms are inspired by the collective social behavior of organisms. They implement trajectory tracking algorithms based on the behavior of insect swarms or the irregular movements of particles in the problem space [18]. The reader can find more details on the various bioinspired optimization algorithms in this survey [18]. This dissertation is more concerned with implementing the first type of bioinspired optimization (i.e. evolutionary algorithms) to material design optimization.

Earlier studies focused on proposing strategies for topology optimization to obtain the most cost-effective and sustainable structural design without the need for cumbersome mathematical programming techniques [14-16]. For example, the work of Xie and Steven demonstrated the possibility of achieving optimal structural designs through finite element analysis (FEA) by mimicking naturally occurring structures such as bones and trees [15]. The concept relies on simplifying an initial design by removing stress-free regions or elements iteratively until reaching an optimal design that consists mostly of load-carrying elements. Since then, different terminologies have been used to represent this bioinspired topology optimization concept such as stress-induced material transformation (SMT) [21], evolutionary structural optimization (ESO)

[15], and soft kill option (SKO) [16, 29, 30]. Numerous applications have utilized this approach to derive optimal material and structural designs in various fields. For instance, in dentistry SMT was used to optimize the shape of dental implants [21, 22] and the design of cavity preparations to minimize the interfacial stresses in bonded restorations [31]. In aerospace, it was used to optimize airframe structures and aircraft panels [19]. Nevertheless, SMT only provides a rough guide towards the optimum design which may not be the absolute best result and further optimization methods are necessary to enhance the design, by reducing stress concentrations, such as stress-induced volume transformation (SVT) [15, 21]. SVT refines the design by smoothing the geometries to remove high stress concentrations in the structure [32]. Both SMT and SVT have gained a favorable reputation in German industry [29, 33]. Nevertheless, in prosthetic design, there remains a challenge to optimize bone implants through architecture topology design to enhance their mechanical properties [34]. SMT assumes perfect bonding at the interface which is not accurate. Interface bonding in FEA is commonly modeled using cohesive zone elements which have been used to model interface bonding in metal/ceramic systems [35], cracks in polymers [36, 37] and adhesively bonded joints [38]. Both methods mimic the adaptive growth of biological structures such as bones and trees stimulated by mechanical loads with an objective to ensure homogenous stress distribution [16, 39].

2.1.3 Trabecular bone as a marvel for bioinspired design

Trabecular or cancellous bone is the complex spongy tissue located near the ends of long bones in our skeletons as well as in irregular bones such as the spine [40]. It has a heterogeneous structure resulting in unique anisotropic structural and mechanical properties across anatomical sites [40]. The tissue of trabecular bone, i.e. the trabeculae, is composed of hydroxyapatite, collagen, water and proteins [40]. Because the trabeculae encompass an open intercommoned

porous space, trabecular bone is classified as a heterogeneous composite cellular solid [40]. It is also classified as an anisotropic material because its trabecular structure is oriented such that strength and modulus are greatest along certain directions [40]. The quality of bone mineralized-tissue composition, 3D architecture, and physiology of the musculoskeletal system are all factors that influence the optimal mechanical performance of trabecular bone [41-44]. Local variation of trabecular texture can be characterized by morphological descriptors such as volume fraction, trabecular thickness, trabecular anisotropy. All this variation is a record of bone loading history and its biomechanical environment [45]. The interconnected trabeculae have various sizes and shapes (Figure 2-1) to better address mechanical challenges and accommodate anatomic features (tendon and ligament insertions, presence of blood vessels nourishing the bone, residues of growth plate, trajectories of predominant forces acting on bone, etc.) [46, 47].

Trabecular bone has an architected structure that is specialized for shock absorbing and multidirectional loading during locomotion (Figure 2-1). Its 3D network of tiny interconnected osseous tissue elements that continually undergo dynamic biological remodeling in a process whereby osteoclasts resorb mature bone tissue followed by osteoblasts that deposit new bone [48]. In 1892, Wolff argued that trabecular bone adapts to external mechanical loading by remodeling and changing the orientation of its trabeculae to attain the maximum efficiency at the lowest metabolic cost (Figure 2-1) [49]. Since then many researchers considered trabecular bone a source for optimal design [50], and several design optimization algorithms have been developed for various applications based on the concept of trabecular bone functional adaptation [51-54].

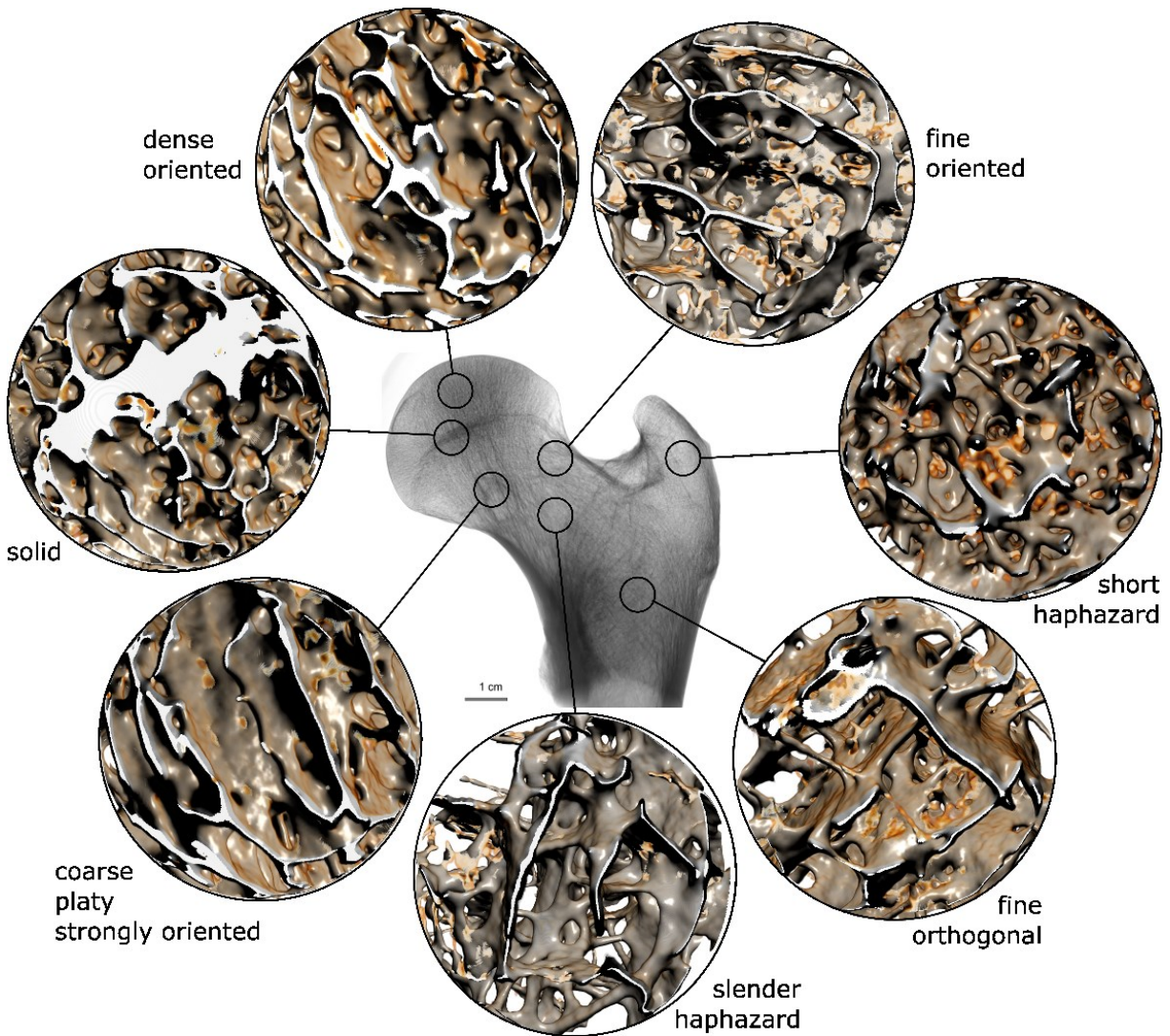


Figure 2-1: Variation and anisotropy of trabecular bone texture within one bone specimen (human proximal femur). Morphological features such as trabecular size, alignment, plate- or rod-like shape, and coarseness of the fabric, all reflect the local adaptation of the tissue to local loading, the adaptation being governed by bone cells and implemented at the micrometer level. Scale bar refers to all circular insets ².

2.1.4 Continuum versus discrete design optimization

Whether gradient-based or bioinspired, topology optimization operates on a fixed finite element mesh of either continuum or discrete (ground-truss approach) elements to optimally distribute material in the layout [24]. The continuum method is a micromechanics theory-based

² Courtesy of Natalie Reznikov.

approach that considers the design space as an artificial composite material with holes distributed. For continuum structures the shape of boundaries and the number of holes are optimized [14]. In the finally optimized model, small hole regions are filled (solid) whereas regions with large holes are considered empty (no material) [14, 55]. In the discrete/ground-truss approach, the optimal layout is reached by determining the position, optimum number, and connectivity of structural elements [14, 55-57]. This is achieved by selecting optimal cross-section parameters of the ground truss members; a grid of all elements connecting the nodes in the design space. In other words, each element is associated with a design variable that determines the element size or its contribution to the whole topology [25]. Typically, cross-sectional parameters of lattice members are considered as the design variables. The cross-sectional parameters of the members are evaluated and determined to support the applied loads on the structure. The members with cross-sectional values near zero are then eliminated to reach the optimal structure. The discrete approach is based mainly on lattice structures; a topic that will be introduced in the next section. Despite being advantageous for requiring less computational effort compared with the continuum approach, the discrete method still lacks unique structures that are designed for specific applications. Thus, it requires flexibility to have a large amount of uniquely designed structures that exploit the full benefits for a specific situation [55, 56]. Note that the continuum approach could be described as global and the discrete approach could be described as local because changes in the continuum method are based on a global objective function whereas changes in the discrete method are based on local entities such as stresses. Both continuum and discrete topology optimization approaches are explored in this dissertation.

2.2 Cellular and Lattice Structures

Cellular structures are structures with interconnected plates and struts incorporating voids [58, 59]. They are classified as natural (i.e. trabecular bone and cork) or humanmade (synthetic), open (solid edges only) or closed (solid edges and faces), random (stochastic connectivity) or periodic (unit cell-based connectivity), 2D (honeycomb) or 3D (sponge) [55, 58, 60]. In case of stochastic connectivity cellular structures are sometime referred to as foams, whereas the term “lattice” is used when the connectivity is regular or periodic [26, 60]. Lattice structures are very common in the discrete ground-truss topology optimization approach [56].

The use of cellular structures has been adopted in natural design because they are porous, lightweight, and mechanically optimized [55]. Inspired by these superb attributes, particularly the high stiffness-to-weight ratio, engineers have been motivated to design and fabricate naturally inspired cellular structures with optimized mechanical properties [55, 58]. Moreover, the use of cellular/lattice structures has been significantly increasing due to the recent industrial sustainable trend to make products with less material usage and less energy consumption [55].

The mechanical properties of cellular structures can be predicted using analytical or numerical methods. Analytical models involve Euler-Bernoulli or Timoshenko beam theories [61]. However, their limitation is that the length of the strut should be significantly greater than its thickness. Hence, only structures with very low relative densities could be studied with beam theories [62]. More sophisticated numerical methods involve the use solid finite elements where the length/thickness ratio limitation is avoided [62]. In such cases, the entire range of relative densities can be studied, but the number of 3D elements raises a computational issue. A method that uses beam finite elements to simulate an entire 3D tetrahedral lattice structure with no relative density limitation was proposed recently [62]. It mainly corrects the material stiffness to

compensate for the loss of validity of the beam theory when the length/thickness ratio of the element becomes too small [62].

Cellular structures deform under mechanical loading by a combination of bending, twisting or stretching of the strut elements [63]. The mechanical properties of cellular structures are a function of the relative density, the solid material, and the unit cell topology [59]. The relative density, one of the most critical attributes, is defined as the ratio of the density of the structure to the density of the base material from which the structure is made [58]. In a stretching-dominated deformation mode, the stiffness/strength of cellular structures scales linearly as a function of the relative density and is higher than that of a bending-dominated deformation mode [59]. On the other hand, the toughness of a bending-dominated deformation is larger compared with a stretching-dominated deformation mode [59, 64]. When both the base material and the relative density are fixed, the mechanical properties of cellular structures depend highly on the topology of the unit cell [59].

A variety of strut-based lattice structures with cubic symmetry and different topologies have been proposed and tested to assess the mechanical behavior. Examples include Kelvin strut-based structures [59, 65], tetrakaidekahedron [61], Octet-truss [8, 60, 66], and Gibson-Ashby strut-based structures [58, 59]. Focus started to shift lately towards lattice structures with mathematically defined topology such as triply periodic minimal surface (TPMS) based topologies [2, 59, 67]. When comparing strut-based and sheet-TPMS based cellular structures, the sheet-TPMS based cellular structures exhibited a near stretching-dominated deformation [59]. The Gibson-Ashby strut-based topologies exhibited a mixed mode of deformation whereas the Octet-truss presented a stretching-dominated behavior [59]. It was also observed that at decreased

relative densities the effect of topology on the mechanical properties becomes more pronounced [59].

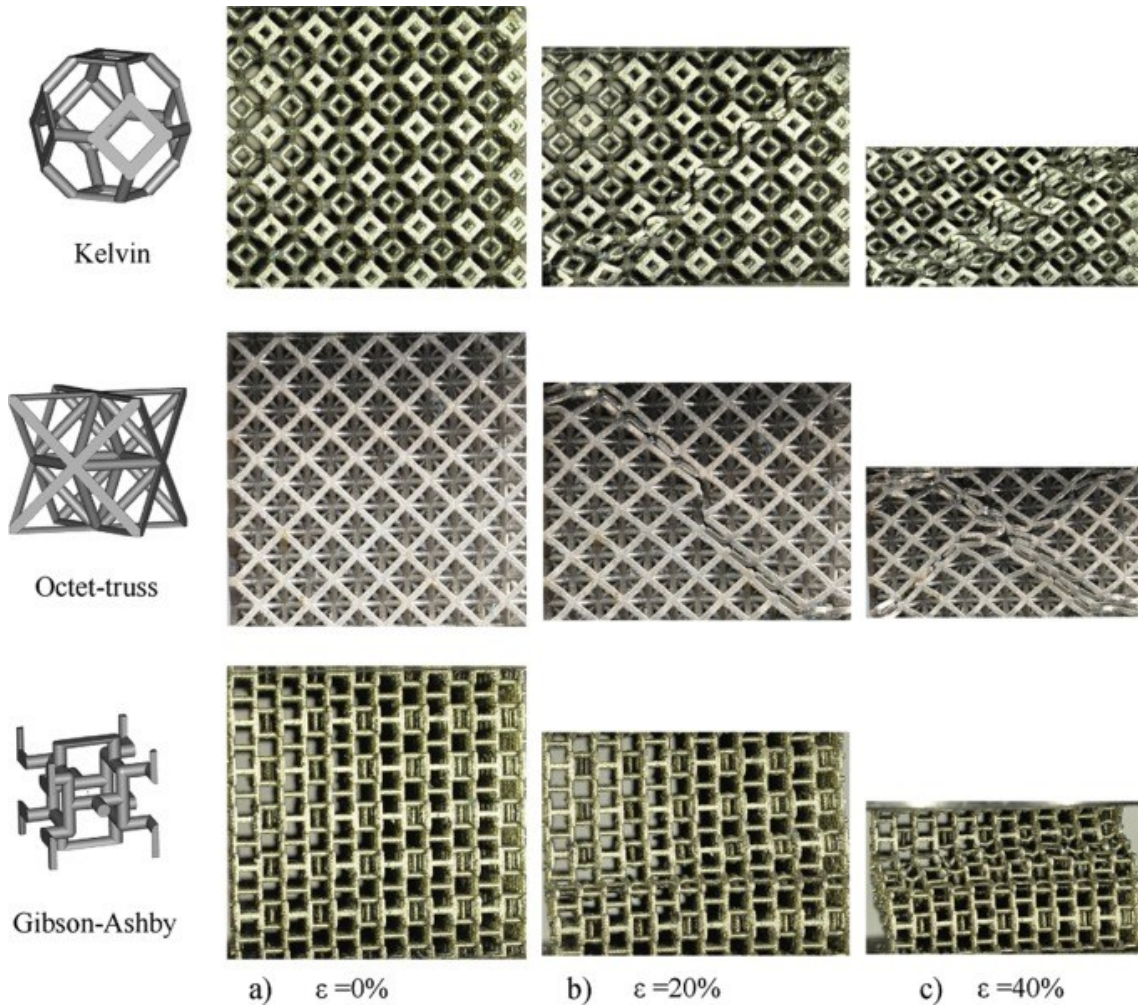


Figure 2-2: Deformation behavior of strut-based lattice structures at different strains ϵ [59].

Due to improper design of the experiment, improper statistical analysis, and different set-up parameters being utilized, it is difficult to compare the results in the existing literature [55]. In addition, more than 90% of lattice structures are manually created and need a significant amount of post-processing before being manufactured. Moreover, there is no systematic procedure available to approximate the manually-created cellular structure and reduce post-processing effort and time [55]. The fabrication of lattice structure is very complex, costly, and challenging using

conventional manufacturing methods [56]. Recent advances in additive manufacturing (AM) have enabled the fabrication of lattice with complex topology in an efficient manner [55].

2.3 Additive Manufacturing

Additive manufacturing (AM) or 3D printing is defined as the process of joining materials to manufacture a product layer by layer from a three-dimensional computer model [68]. The 3D model is usually made using computer-aided design (CAD) tools. AM is becoming very popular for applications that require the manufacturing of products with sophisticated internal architectures. For example, in orthopedic regenerative medicine there is a demand to design bone implants (i.e. scaffolds) that replicate the biomechanical properties of the host bones [3]. Among the different technology options, 3D printing is becoming popular due to the ability to directly print porous scaffolds with reticulate shape and interconnected porosity [69]. Selective laser-sintering (SLS), direct metal laser-sintering, and selective electron beam melting (SEBM) are among the most common AM technologies used to produce lightweight and optimized structures in which material is only added where needed and the amount of wasted material is reduced [55, 70]. These techniques use an energy source (laser or electron beam) to selectively melt or sinter layers of powder to form a 3D structure [55]. With recent advances of CAD/CAM technologies in dentistry [71-73], SLS has been used for processing metal frameworks for dental prostheses [70, 74, 75]. The superior precision of AM technologies allows for customized denture designs and renders the treatment accessible to a larger portion of the population. The next section will provide an overview on removable partial dentures (RPDs) and present design challenges that will be addressed in this dissertation to demonstrate design optimization.

2.4 Removable Partial Dentures (RPDs)

Edentulism refers to patients missing some or all their natural teeth. Due to its impact on patients' esthetic, phonetics and ability to chew food effectively, tooth loss is an important handicap that needs to be treated [76-78]. Removal partial dentures (RPDs) are essential cost-effective components of the dental prostheses industry. Their function is to restore missing teeth in partially edentulous patients improving their quality of life [79]. A typical cast-metal RPD, shown in Figure 2-3, consists of a metallic framework connected to artificial teeth and to an acrylic denture base made in poly (methyl methacrylate) (PMMA) [80]. The metallic framework has a direct retainer that engages a tooth to provide retention and resist movements away from the oral tissues and natural teeth. Clasps are the most common retainers and they usually consist of a lingual arm, a buccal arm, and a rest. A clasp buccal arm typically engages a tooth at undercut depths around 0.25 mm [81]. The most common clasp designs are circumferential clasps and bar clasps [80].

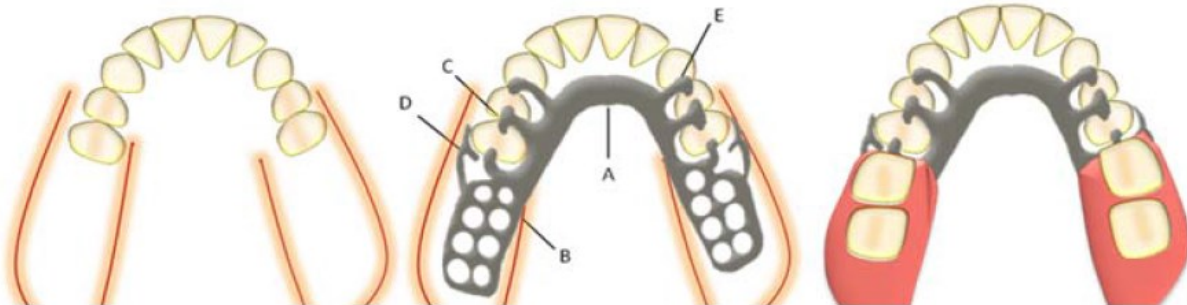


Figure 2-3: (Left) the mandibular partially edentulous arch before treatment. (Middle): the mandibular framework for the removable partial denture and its components of A: major connector; B: minor connector; C: rests; D: direct retainer; E: indirect retainer. (Right) the removable partial denture (RPD) on the edentulous arch.

Despite their wide usage, RPDs continue to face a few challenges [82], a major one being their plastic deformation and fracture caused by the constant exposure to masticatory forces [83]. This is aggravated by two issues: (1) RPDs are vulnerable to mechanical failure by fatigue

mechanism that occurs at the metal clasp, a critical component of the denture [84-86]; (2) RPDs combine acrylic and metallic components that are bonded together through mechanical interlocking provided by sandblasting of the metal surface. The bond between the acrylic and metallic components of the denture is weak and catastrophic mechanical failure often happens at this acrylic/metal interface [87-90]. Another important problem is esthetical and has to do with the display of clasp assemblies and colors at the plastic/metal interface due to separation [71, 85, 91].

2.4.1 Denture clasp

A denture clasp is a cantilever beam that undergoes elastic deformation when a force is applied to place the denture in the mouth, or remove it [92]. When this occurs, the clasp deflects and slides on the contoured surface of the tooth to settle on an undercut below the line of contour of the tooth. The magnitude of the retention force needed to deflect the clasps and allow placement or removal of the denture is critical for the denture performance. The force needed to place or remove a clasp from its intended position in the tooth is going to depend on the contour of the tooth and the deflection of the clasp. Thus, patient-specific tooth anatomy factors can influence the mechanical performance of the clasp. These include the depth, position and slope of the undercut on the tooth surface in which the clasp is supposed to settle. Several clinical studies showed that clasp failure is the most common complication of RPDs and the majority of RPDs are replaced after 5 to 6 years because of clasp failure [93]. RPD frameworks and clasps are commonly made from cobalt-chromium (Co-Cr) alloys because of their suitable cost, biocompatibility and excellent corrosion resistance [94, 95]. Hence, bettering the clasp design is necessary for enhancing the performance of RPDs.

The lack of a systematic approach for clasp design based on engineering principles stimulated previous attempts in literature in the search of new methods for optimizing the design

of clasps. Warr argued that the possibility of fracture due to faulty design is underestimated and proposed a numerical framework to evaluate the performance and quality of clasps [96, 97]. Brockhurst provided a systematic method for selecting clasp cross-section dimensions based on theoretical analyses [98]. He found that by using a clasp of uniform cross-section instead of variable cross-section decreased the deflection by 23% [98]. However, both Warr and Brockhurst used the straight beam theory to solve for the maximum bending stress, which is questionable for the curved clasp where the neutral axis is shifted towards the inner curvature of the clasp.

Other studies carried out numerical finite element analysis (FEA) to identify the stress distribution and deflections of clasps upon loading [99-103]. Sandu et al. analyzed the stress distribution in the retentive arms of combination clasps using 3D FEA and concluded that the mechanical performance of half-round cross-sections is better than round ones for clasps on premolars [100]. They also simulated the fatigue behavior of cast Co-Cr circumferential clasps and reported a maximum stress value of 310 MPa located at the junction of the clasp arm with the body under a vertical force of 5 N. Shirasu and coworkers studied the plastic deformation of Co-Cr wrought-wire clasps using non-linear FEA and suggested that permanent deformation initiates at the clasp shoulder [101]. Morris et al. concluded that tapered circumferential clasps would be more susceptible to fail by fatigue after prolonged clinical use compared to non-tapered ones [102]. Sato et al. conducted 3D FEA to study the effect of shape on the stress and stiffness of an I-bar clasp and derived a systematic formula between clasp shape and stiffness based on the FEA results [99]. An I-bar clasp consists of a straight vertical component arising from a horizontal connector approaching the undercut from the gingival direction (see Figure 2-4) [80]. I-bar clasps require minimal tooth contact as compared with circumferential clasps and provide adequate retention

with minimal undercut. However, the horizontal connector must be placed far enough (i.e. 2.5 - 3 mm) from the gingival margin to avoid food impaction [104].



Figure 2-4: I-bar clasps engaging on teeth in a mechanical retention experiment [105].

Despite the various theoretical and numerical studies, a predictive mapping to help select the optimal design of clasps remains nonexistent. Hence, there is a need to integrate mechanics modeling with FEA to identify optimal design criteria for the metal clasp. Design optimization of clasp arms through analytical modeling should be derived based on curved beam theory and Castigliano's energy method instead of straight beam theory [106, 107]. The contribution of frictional means of retention should be incorporated in the design equations. The clasp design optimization model should incorporate the required retention force, undercut, and tooth topology.

2.4.2 *Acrylic/metal interface in dental prostheses*

RPDs combine acrylic and metallic components that are bonded together. However, the weak bond between these two materials often results in catastrophic mechanical failure of the RPD [104]. Acrylic/metal bonding in RPDs is divided into two categories: mechanical and chemical

[108]. The mechanical category is further split into macromechanical and micromechanical. Some examples of micromechanical bonding are sandblasting [109] and etched casting [110]. Micromechanical bonding is not enough at critical positions such as anterior teeth, therefore minor connector designs are sometimes incorporated as forms of macromechanical connections between acrylic resin bases and denture metal frameworks at such locations [111]. Different authors suggested different mechanical designs for the acrylic/metal interface of RPDs [111-114]. In many cases acrylic-resin bases are attached to the metal framework by means of a preformed retention mesh [81] (see Figure 2-3, middle, B). Only little work has been done to provide engineered objective guidance for optimizing the retention design for acrylic resin bases of RPDs [111]. Terkla and Laney suggested short thin buccal arms extending from retention webs to supply additional retention for the acrylic denture base [112]. The geometry and orientation of the retention arms were not objectively guided.

Metal strengtheners have also been incorporated as reinforcement in acrylic dentures. Ruffino argued that metal strengtheners should be positioned perpendicular to the anticipated fracture in acrylic dentures [115]. The influence of the cross-section shape and length of metal strengtheners on the stress distribution and deflection in acrylic denture bases under loading was investigated [116, 117]. The considered loading ranged between 10-30 N. It was concluded that triangular or square cross-section shape of the metal strengtheners effectively minimized both maximum stress in the acrylic denture base and the vertical deflection of the saddle to the ridge, which averts early fracture of the acrylic denture base [118]. Mahler and Terkla reported increased tensile stress in regions of material discontinuity [119]. The use of metal mesh and glass fibers in acrylic dentures was also proposed to strengthen the denture [120]. Vallittu et al. conducted three-

point bending experiments and suggested that by incorporating glass fibers into PMMA denture bases, the strength of the denture can be increased [121].

Due to the complexity of the oral cavity, proper optimized interfaces in RPDs is virtually impossible using the traditional manual methods. There is a need for a guided method of reinforcing the base of dentures during preparation [122]. An optimized practical solution for retention designs of acrylic resin bases on metal frameworks of RPDs particularly for anterior teeth is still nonexistent. With 3D laser-sintering, optimized inter-locking features for acrylic/metal interface can be reached. Stronger acrylic/metal interfaces can be achieved using design optimization methods.

The bioinspired topology optimization approach is considered a good candidate to optimize the design of acrylic/metal interfaces in dentures. Interfaces in nature serve as source of bio-inspiration for designing robust interfaces that bond together different material phases. A wide range of biological designs and interface geometries are observed in nature. Researchers studied various biological materials, structures and interfaces such as trees, suture, bones, shells, nacre, teeth, and others [17, 123-132]. One of the crucial issues is the weak interfaces between stiff and compliant phases which need to be optimized according to the intended functions of the structure [129]. As alluded earlier, there has been considerable interest in the application of topology and shape optimization techniques to determine the most efficient material distribution in structural design of multi-materials and FEA is the main tool used to implement these techniques [29, 31, 32, 39, 133]. In structures with two or more different materials, areas of high stress concentration could be caused by a large difference in elastic modulus across a bonded interface [82].

In Chapter 4 bioinspired topology optimization is used to overcome the challenges associated with acrylic/metal bond loss by enabling engineered laser-sintered dentures with

optimized designs and mechanical performance. It is important to confirm the validity of additive manufacturing to fabricate the optimized designs obtained from the bioinspired topology optimization. To reach optimal designs, bioinspired topology optimization incorporates the use of failure theories for polymers and metals as well as Finite Element Analysis (FEA), which will be discussed in the next sessions.

2.5 Failure Theories

2.5.1 Maximum Normal Stress Theory

Failure theories are used to indicate the onset of failure in stress analysis. One of the important failure theories is the maximum normal stress theory, which is commonly used for brittle materials. It states that failure occurs when one of the three principal stresses equals the ultimate strength obtained from the tensile test of a specimen of the same material [106, 107]. To explain the meaning of principal stress, it is first important to understand that stress at any element is composed of normal (perpendicular to element's plane) and shear (parallel to element's plane). In 2D, the principal stress is the maximum or minimum normal stress exerted on a plane of an element and at which the value of the shear stress is zero [106, 107].

2.5.2 Von Mises Stress and Maximum-Distortion-Energy Criterion

Another important failure measure is the von Mises stress after the mathematician Richard von Mises who proposed that a structural component is safe if the maximum value of the distortion energy per unit volume is smaller than the distortion energy per unit volume required to cause yield in tensile-test specimen of the same material [106]. This principle is known as the maximum-distortion-energy criterion and is among the most popular yield criteria for ductile materials [106, 107]. In other words, yielding is assumed to occur when the von Mises stress equals the yield stress

of the material. In 3D, von Mises stress σ_{vM} is calculated as: $\sigma_{vM} = \frac{1}{\sqrt{2}} \left[(\sigma_x - \sigma_y)^2 + \right.$

$(\sigma_y - \sigma_z)^2 + (\sigma_z - \sigma_x)^2 + 6(\tau_{xy}^2 + \tau_{yz}^2 + \tau_{xz}^2)]^{1/2}$, where σ represents normal stress and τ stands for shear stress. Hence, von Mises is an equivalent stress calculated as a function of the normal and shear stresses in the structure, where the shear stress effect is magnified because it is potentially more dangerous for the structure and its elements.

2.6 Finite Element analysis (FEA)

A fundamental component of bioinspired structural design optimization is FEA. Engineers and scientists tend to represent physical processes in nature by mathematical formulations, often through differential equations, to simplify and understand them. However, the solution of such mathematical models by exact methods is often challenging [134]. The finite element method is an approximate numerical solution that approximates the differential equations by functions over subregions of the domain [134].

Several ideas and steps of the finite element method could be illustrated through analogy with a simple example of approximating the circumference of a circle using a finite number of line segments [134]. Suppose that it is required to approximate the circumference of a circle with a known radius R in a method analogous to finite elements analysis. The first step is finite element discretization, in which the circumference of a circle is approximated as a finite number of line segments (i.e. subdomains) [134]. Such line segments are called elements and they are connected to one another at points called nodes. The collection of elements is called the finite element mesh [134]. The next step is to formulate the elements equation. A typical element is isolated and its properties (i.e. length in this example) are calculated by some particular methods (ancient mathematicians used to measure the lengths of the line segments) [134]. The next step is the assembly of element equations and solution, where for our example the value of the perimeter is

approximated by summing the lengths of the line segments. The final step is convergence and error, in which the error is approximated, and a convergence criterion is fulfilled. For the presented example it could be demonstrated that the approximate perimeter approaches the exact value of the circumference (i.e. $2\pi R$) as the number of elements approaches infinity [134].

Hence, in FEA the problem domain is divided into finite regions or finite elements, and the differential equation is represented by a combination of approximation functions. For each finite element, approximation functions are represented as a linear combination of algebraic polynomials and undetermined coefficients [134]. Algebraic relations among the undetermined coefficients are determined by respecting the governing equations, loading conditions, and boundary conditions [134]. The undetermined coefficients represent the values of the solution at the nodes, which is often the unknown displacements for problems in solid mechanics including those considered in this dissertation. The approximation functions are derived through interpolation theory. After deriving the approximation functions for the elements, the stiffness matrix $[K_e]$ and consistent loads (F_e) are found for each element using the variational methods i.e. minimizing potential energy. Then, all element stiffness matrices and load vectors are assembled in a global stiffness matrix $[K]$ and a global load vector (F), respectively. After imposing boundary conditions, the system of equations $(F) = [K](U)$ is solved by a standard numerical procedure like Gauss elimination or Choleski's decomposition to find the displacements at nodes [135]. Finally, displacement-strain relationships and stress-strain relationships are used to find the strains and stresses of the elements, respectively [135].

Regions or finite elements could be either one-dimensional (e.g. beams), two-dimensional (e.g. triangles) or three-dimensional (e.g. tetrahedrons). The finite elements are connected through nodes and/or edges (in 1D two elements are connected through a node whereas in 2D and 3D two

elements are connected through nodes and edges). Among the most popular outputs of FEA are the stress and strain within each element in the domain as well as the forces and displacements at nodes.

3 Analytical Modeling for Optimization

This chapter focuses on optimization based on analytical modeling. An analytical model was developed to optimize the design and predict the safe performance of denture circumferential clasps. Parametric studies were conducted to map the response of the material under different loading and design conditions. Using the laser-sintered Co-Cr alloy as a representative clasp material, a predictive mapping to help determine the optimal clasp design was established. The results demonstrated that the dimensions of clasps can be optimized to prevent stress from reaching the fatigue failure limit. Based on the analytical model, design charts have been developed to guide the optimal design of clasp length and cross-sectional radius. The design charts could be used by dental technicians and designers to select the clasp geometry based on the measured undercut of the tooth.

- This chapter has been published in *Dental Materials* , 34(10), 1474-1482.

DOI: <https://doi.org/10.1016/j.dental.2018.06.011>

An analytical model to design circumferential clasps for laser-sintered removable partial dentures

Ammar A. Alsheghri ^a, Omar Alageel ^{b,c}, Eric Caron ^d, Ovidiu Ciobanu ^b, Faleh Tamimi ^b, Jun Song ^{a,3}

^a Department of Mining and Materials Engineering, McGill University, Montreal, QC, Canada

^b Faculty of Dentistry, McGill University, Montreal, QC, Canada

^c College of Applied Medical Sciences, King Saud University, Riyadh, Saudi Arabia

^d 3DRPD Inc., Montreal, QC, Canada

Corresponding author complete address: Department of Mining and Materials Engineering, McGill University, 3610 University Street, Montreal, QC, Canada, H3A 2B2

Email: jun.song2@mcgill.ca

Acknowledgements: The authors thank Dr. Faez Al-Hamed for reviewing this manuscript.

Funding: This work was supported by 3DRPD Inc., Montreal, Quebec, Canada; Fonds de recherche du Québec – Nature et technologies (FRQNT), McGill Engineering Doctoral Award (MEDA), and Natural Sciences and Engineering Research Council of Canada [grant number NSERC CRD 469834].

³ The author to whom corresponding should be addressed.

E-mail addresses: ammar.alsheghri@mail.mcgill.ca (A. A. Alsheghri), omar.alageel@mail.mcgill.ca (O. Alageel), ovidiu.ciobanu@mail.mcgill.ca (O. Ciobanu), eric.caron@dental-wings.com (E. Caron), faleh.tamimimarino@mcgill.ca (F. Tamimi), jun.song2@mcgill.ca (J. Song).

Abstract

Objective: Clasps of removable partial dentures (RPDs) often suffer from plastic deformation and failure by fatigue; a common complication of RPDs. A new technology for processing metal frameworks for dental prostheses based on laser-sintering, which allows for precise fabrication of clasp geometry, has been recently developed. This study sought to propose a novel method for designing circumferential clasps for laser-sintered RPDs to avoid plastic deformation or fatigue failure.

Methods: An analytical model for designing clasps with semicircular cross-sections was derived based on mechanics. The Euler–Bernoulli elastic curved beam theory and Castigliano's energy method were used to relate the stress and undercut with the clasp length, cross-sectional radius, alloy properties, tooth type, and retention force. Finite element analysis (FEA) was conducted on a case study and the resultant tensile stress and undercut were compared with the analytical model predictions. Pull-out experiments were conducted on laser-sintered cobalt-chromium (Co-Cr) dental prostheses to validate the analytical model results.

Results: The proposed circumferential clasp design model yields results in good agreement with FEA and experiments. The results indicate that Co-Cr circumferential clasps in molars that are 13 mm long engaging undercuts of 0.25 mm should have a cross-section radius of 1.2 mm to provide a retention of 10 N and to avoid plastic deformation or fatigue failure. However, shorter circumferential clasps such as those in premolars present high stresses and cannot avoid plastic deformation or fatigue failure.

Significance: Laser-sintered Co-Cr circumferential clasps in molars are safe, whereas they are susceptible to failure in premolars.

Keywords

Removable partial dentures (RPDs); laser-sintering; circumferential clasp design; cobalt-chromium (Co-Cr); plastic deformation; fatigue failure; finite element analysis (FEA); undercut; retention force; stress.

3.1 Introduction

Removable partial dentures (RPDs) are essential cost-effective components of the dental prosthesis industry. They are used to restore missing teeth in partially edentulous patients, improving their quality of life. Millions of patients are affected by this treatment worldwide; over 13% of the adult population in North America and Europe wear RPDs [136].

Despite their widespread use, RPDs present a few challenges [82, 83, 85] such as problems related to comfort and appearance [85, 137] and their vulnerability to mechanical failure by fatigue [138]. This failure mostly occurs at the metal clasp, a critical component that retains the denture to teeth at the undercut area [81]. A clinical study has shown that clasp failure is the most common complication of RPDs and the main reason why 50% of RPDs should be replaced after 5 to 6 years of usage [83].

The performance of clasps is governed by the clasp material properties (such as fatigue strength and elastic modulus) and design. RPD frameworks and clasps are commonly made from cobalt-chromium (Co-Cr) alloys because of their suitable cost, biocompatibility and excellent corrosion resistance [70]. A substantial enhancement in the material properties of Co-Cr alloys is difficult because it is a function of the composition of the alloy [98]. Hence, improving the clasp design is necessary for enhancing the performance of RPDs.

Clasps are traditionally made along with RPDs using a casting technique. However, casting is influenced by the skill of dental technicians and does not allow for precise control over the design of the clasps, which results in ill-fitting of RPDs [75]. Recent advances in CAD/CAM technologies [73], particularly additive manufacturing techniques such as laser sintering [70, 74, 75], allow the fabrication of very precise designs which opens the window for improving the design and fit of

clasps in RPDs. Laser-sintered Co-Cr RPDs provided better fitting [75] as well as improved fatigue resistance [70] and patient satisfaction [139] compared with cast Co-Cr RPDs.

The RPD industry still depends on traditional guidelines in driving the design of clasps [140]. These guidelines have valuable merits that the industry has amassed over the years. However, they are generally empirical and qualitative. In addition, the current design practice heavily relies on the skills of dental technicians and designers [140]. The traditional empirical and ad hoc design approach can render huge variation in clasp design, and subsequently vast variation in the performance of RPDs and patient experience [75, 139].

The lack of a systematic approach based on engineering principles stimulated previous research into finding new methods for designing better clasps. Warr argued that the possibility of fracture due to faulty design is underestimated and proposed a numerical framework to evaluate the performance and quality of clasps [96, 97]. Brockhurst provided a systematic method for determining clasp cross-sections based on theoretical analyses [98]. However, both Warr and Brockhurst used the straight beam theory to calculate the maximum bending stress, which is questionable for the curved clasp where the neutral axis is shifted towards the clasp's inner curvature. In addition, the practical application of Warr's formula was not possible at that time due to difficulty in obtaining the required measurements [97, 141].

More recent studies carried out FEA to identify the stress distribution and deflection of clasps upon loading [99-102]. However, these studies did not provide mathematical design models. Further, the type of finite element used in most cases were 8-node linear order brick elements with three degrees of freedom per node [99-101], which causes shear locking effects making the reaction to bending stiffer and hence may lead to quantitatively questionable results [142]. The use

of quadratic order or reduced integration brick elements with adequate mesh density would solve this problem [142].

Apart from retention caused by spring and friction forces, physical forces such as surface tension within the denture-saliva-palate system play an important role in retention due to the phenomena of capillarity and wetting [143]. Researchers have worked extensively on developing suitable expressions for the adhesion force due to surface tension [144, 145]. Retention due to surface tension has only been considered for denture bases on soft tissues, where capillary forces are more significant compared with clasps on teeth. However, combining capillary, friction, and spring forces in modeling clasp retention would provide a complete representation for the different forces involved.

Despite the various theoretical and numerical studies, a predictive mapping to help determine the optimal clasp design remains nonexistent to the best of our knowledge. The objective of this study is to use mechanics to identify design equations for circumferential clasps of RPDs processed by laser-sintering. Only molar and premolar teeth are considered because clasps are generally placed on posterior teeth for aesthetic reasons. Prosthodontic experts provided feedback on the design of clasps related to their placement (i.e. molars versus premolars) and dimensions [140]. However, this feedback was based on experience and among the goals of this manuscript is to investigate whether the model results will agree with the common practice. Our hypothesis is that the proposed model could predict the safe performance of laser-sintered circumferential clasps.

3.2 Materials and methods

A mechanics analytical model for clasp design was derived based on Euler–Bernoulli curved beam theory and Castigliano's method [106, 107]. Spring, friction, and adhesion retention forces were incorporated into the model. The model incorporates the effect of tooth anatomy, maximum

stress, alloy properties, undercut and required retention force. Next, FEA of a case study obtained from the analytical model was carried out. Finally, to validate the model experimentally, different clasps were produced using the laser-sintering technique and the retention force required for clasp dislodgement was measured and compared with the retention force provided by the analytical model.

3.2.1 Analytical model

A circumferential clasp engages the undercut as shown in Figure 3-1. Considering a clasp being pulled out of the undercut vertically, the tooth would press on the clasp retentive arm. Figure 3-1 illustrates the forces experienced by the clasp cross-section when a clasp disengages the undercut. For simplicity, these forces are assumed to be point forces acting at the clasp tip. The tooth buccal surface profile was assumed to make an angle θ with the x -axis. The forces acting on the clasp are the retention force F_R , the normal force perpendicular to the surface of the enamel F_N , the adhesion force F_{Ad} due to surface tension of the clasp-saliva-tooth system, and the friction force between the clasp and the enamel $F_{fr} = \mu F_N$, where μ is the static friction coefficient.

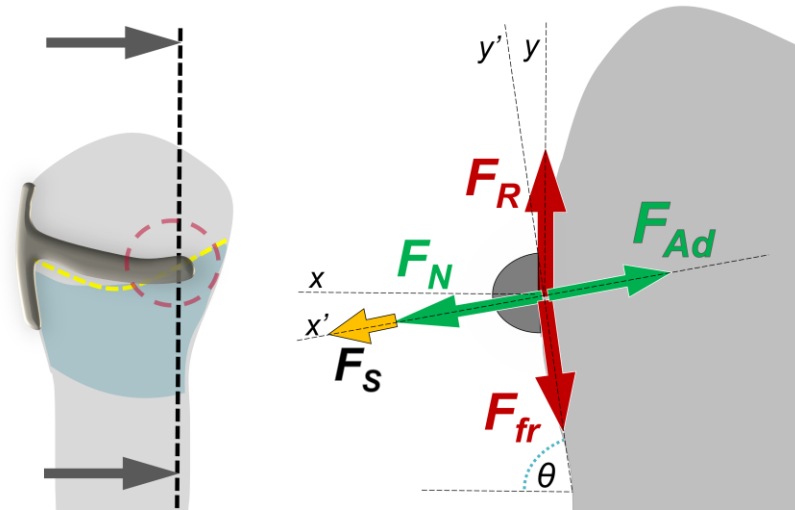


Figure 3-1: Schematic of a circumferential clasp showing the forces experienced by the clasp cross-section while being disengaged from the undercut.

By considering the equilibrium of forces, the resulting force responsible for deforming the clasp is the spring force F_S , which can be expressed in terms of the other forces as (details provided in the supplementary material):

$$F_S = F_R \left(\frac{\sin \theta}{\mu} - \cos \theta \right) - F_{Ad} \quad (1)$$

To calculate the spring force F_S in Eq. (1), a circumferential clasp was approximated as a curved beam as shown in Figure 3-2 that lies in a plane parallel to the x' axis in Figure 3-1. Figure 3-2 shows a clasp extending from the clasp shoulder (where point A lies) to the clasp tip (point B) over an angle φ (units in Rad). Angle α (units in Rad) defines the location of a point of interest J on the clasp. The spring force F_S acts on point B [92], as depicted in Figure 3-2. The failure criterion could be defined as the greatest stress in the clasp that exceeds the failure criterion for fatigue of the material. In Figure 3-2, the maximum stress which occurs at the inner curvature of the clasp shoulder was calculated based on Euler–Bernoulli elastic curved beam theory as [107]:

$$\sigma_{max} = \sigma_A = \frac{F_S r_c (1 - \cos \varphi)(r_n - r_i)}{A(r_c - r_n)r_i} + \frac{F_S}{A} \quad (2)$$

where A is the cross-sectional area of the clasp at point A, r_i is the inner radius of curvature, r_n is the radius of curvature of neutral axis and r_c is radius of curvature of the centroidal axis. Figure 3-2 shows that the neutral axis does not coincide with the centroidal axis and is shifted towards the inner curvature of the clasp. The clasp cross-sectional area was assumed constant for simplicity of the mathematical analysis. A linear elastic material model was considered with elastic deformations only, therefore the deflection δ of the clasp at point B was obtained from Castigliano's theorem [106, 107]:

$$\delta = \frac{F_S}{E} \int_0^{\left(\frac{L}{r_i}\right)} \frac{(\cos \alpha - \cos \varphi)^2 r_c^3}{I} d\alpha \quad (3)$$

where E is the elastic modulus, I is the second moment of the clasp cross-sectional area and deflection δ is the undercut. The effect of transverse shear was neglected for simplicity. For curved beams, as the radius of curvature increases, the contribution due to shear forces becomes negligibly small compared with the bending component [107]. For slender beams, accounting for shear forces would lead to an increase in the predicted displacements of 5% or less [146]. Hence, only the contribution due to bending was considered in Eq. (3). Note that Eqs. (2) & (3) are valid for clasps with any cross-section. For a semicircular cross-section with radius c [147]:

$$A = \frac{\pi c^2}{2} ; I = \left(\frac{\pi}{8} - \frac{8}{9\pi}\right) c^4 = 0.1098c^4 ; r_c = r_i + \frac{4c}{3\pi} ; e = r_c - r_n \cong \frac{I}{Ar_c} \quad (4)$$

By substituting Eqs. (4) into Eqs. (2) & (3) the maximum stress and deflection in a circumferential clasp with semicircular cross-section were obtained:

$$\sigma_{max} = \frac{F_S \left(r_i + \frac{4c}{3\pi}\right) \left[1 - \cos\left(\frac{L}{r_i}\right)\right]}{\pi r_i} \left[\frac{4 \left(r_i + \frac{4c}{3\pi}\right)}{3(0.1098)c^3} - \frac{2}{c^2} \right] + \frac{F_S}{\frac{\pi c^2}{2}} \quad (5)$$

$$\delta = \frac{F_S}{E} \int_0^{\left(\frac{L}{r_i}\right)} \frac{\left[\cos \alpha - \cos\left(\frac{L}{r_i}\right)\right]^2 \left(r_i + \frac{4c}{3\pi}\right)^3}{0.1098c^4} d\alpha \quad (6)$$

Eqs. (1), (5), and (6) represent an analytical model that enables safe design of clasps with semicircular cross-sections based on reverse engineering. The friction coefficient between the enamel and the Co-Cr alloy under wet conditions is 0.454 [148]. The adhesion force was assumed to be 1 N based on the interface debond energy of 100 J/m² between grit-blasted Co-Cr and PMMA

in ambient air conditions [149]. Note that pull-out experiments were done with plastic teeth and the interfacial bond energy between Co-Cr and PMMA was used because it is similar to that between Co-Cr and teeth. The elastic modulus for the laser-sintered Co-Cr is 200 GPa [70, 150]. The inner radius of curvature of the clasp r_i should be clinically measured because it varies per patient and type of tooth. In general, r_i for a premolar is between 4-5 mm whereas for a molar is near 7 mm [97, 151-153].

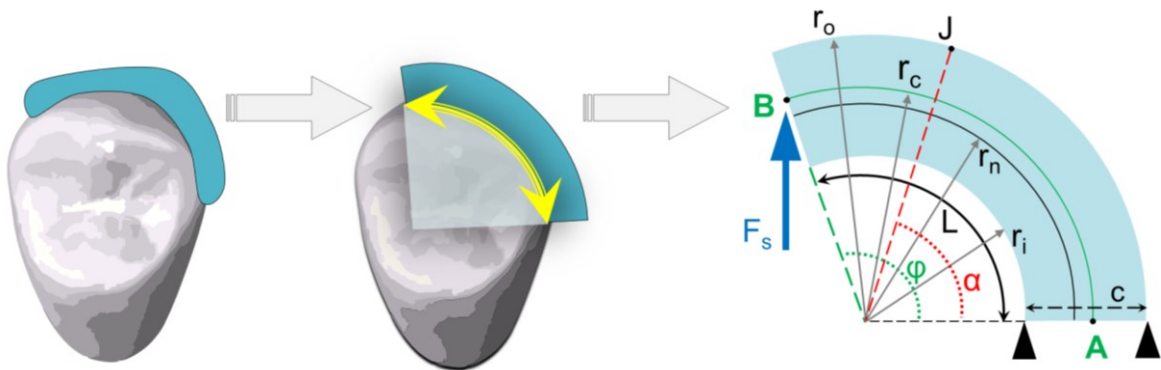


Figure 3-2: Schematic of a circumferential clasp approximated as a curved beam extending from point A at the clasp shoulder to point B at the clasp tip, with the relevant variables illustrated.

3.2.2 FEA

In accordance to the analytical analysis, corresponding FEA was conducted on a circumferential clasp model to provide an overview of the stress and deflection contours along the length of the clasp. The FEA was performed using ABAQUS 6.11 (SIMULIA, USA) [154]. The purpose was to identify the failure region in the clasp. In the FEA, only elastic deformations were considered and a linear elastic material model was used. A clasp model with the following set of parameters was considered: length ($L = 9 \text{ mm}$), cross-sectional radius ($c = 0.9 \text{ mm}$), radius of curvature ($r_i = 5 \text{ mm}$), Elastic modulus ($E = 200 \text{ GPa}$), and Poisson's ratio ($\nu = 0.3$). The clasp shoulder was fixed in all directions except the y' -direction, which implies that the clasp shoulder is not restricted to move in the direction perpendicular to the plane where the clasp lies.

A spring force $F_S = 19\text{ N}$ was exerted at the clasp free end (point B in Figure 3-2), which by trial-and-error was found to result in a deflection of about 0.25 mm at the clasp tip. Twenty-node quadratic brick elements with reduced integration were used to mesh the clasp with an element size of 0.05 mm.

3.2.3 *Experimental Validation of Analytical Model*

To validate the results from theoretical analysis, RPD circumferential clasps were tested on different tooth types of upper and lower arches. Those clasps were designed and fabricated on the molar and premolar teeth of a dentoform model as depicted in Figure 3-3(a) (Nissin Dental Products Inc., Kyoto, Japan) at the prototyping center (3DRPD Inc., Montreal, QC, Canada). First, upper and lower arches of the dentoform models were scanned using a 3D scanner (Dental Wings Inc., Montreal, QC, Canada). Then, circumferential clasps with different lengths and cross-sectional areas were designed on the scanned models using a CAD software (3Shape Inc., Copenhagen, Denmark) and placed on the abutment teeth. Next, Co-Cr clasps were processed by direct laser-sintering technology using the PXM system (Phenix Systems, Riom, France) with a layer thickness of 30 μm , a Fibre laser power of 300W and a wavelength of 1070 nm. The Co-Cr powder for the laser-sintering system was provided by (Sint-Tech, Clermont-Ferrand, France) with a composition of Co 63%, Cr 29%, Mo 5.5% Mn 0.9%, Si 0.8%, and Fe 0.8%.

The retention forces of each tooth clasp were measured on the dentoform model fixed on the lower grip of a universal testing machine (MTS, Eden Prairie, MN) as shown in Figure 3-3(b). The dentoform model allows replacement of each tooth on the arch enabling measurement of clasp retention force for each tooth type separately. To perform the test, a contralateral pair of PMMA teeth was placed on the model and engaged with two clasps of the metal framework which in turn was attached to the upper grip of the testing machine. The machine applied a pull-out force at a

constant speed of 5 mm/sec until releasing clasps from the teeth [85]. The retention force was recorded by the machine. Six measurements were recorded and the process was repeated for each tooth type on both the upper and lower arches. The readings were averaged and the measured retention force was then compared with the retention force predicted by the analytical model. To obtain the retention force from the analytical model, the spring force was first calculated from Eq. (6) and then substituted into Eq. (1). An elastic modulus of 200 GPa was used [70, 150]. The undercut δ , tooth tilt angle θ , clasp cross-sectional radius c and length L were measured for each tooth type. The radius of curvature r_i for each tooth and friction coefficient μ were obtained from the literature [97, 148]. Table 3-1 in the supplementary material lists the values used in experimental validation of the analytical model.

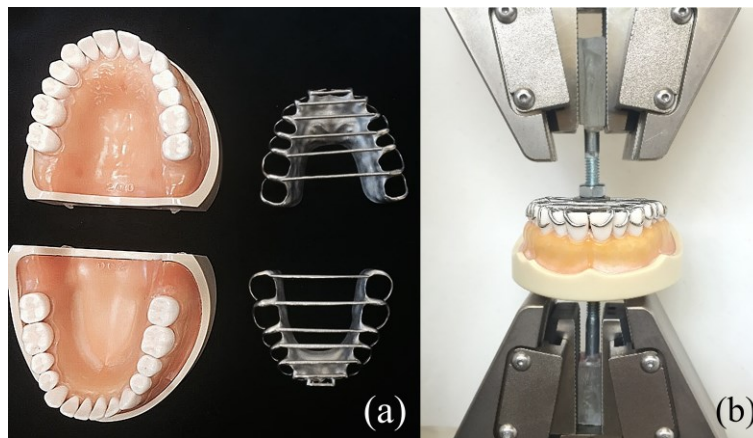


Figure 3-3: Photographs showing (a) Dentofrom teeth model and laser-sintered clasps; (b) measurement of retention forces using a universal testing machine (MTS, Eden Prairie, MN). Note that only circumferential clasps on molar and premolar teeth were considered in this study.

3.3 Results

3.3.1 Analytical model

Figure 3-4 depicts the retention force F_R predicted from Eq. (1) as a function of the tooth tilt angle θ for four different friction coefficients with the spring force and adhesion force specified as 10 N and 1 N, respectively. A value of 10 N was assigned to the spring force to be compatible

with undercuts in the range of 0.1- 0.25 mm. A monotonic increase in the retention force as the tilt angle decreases is observed. Figure 3-1(b) illustrates that undercut increases when tilt angle decreases. Hence, the retention force increases as the undercut increases when other factors remain constant. Figure 3-4 demonstrates that a larger coefficient of friction leads to a higher retention.

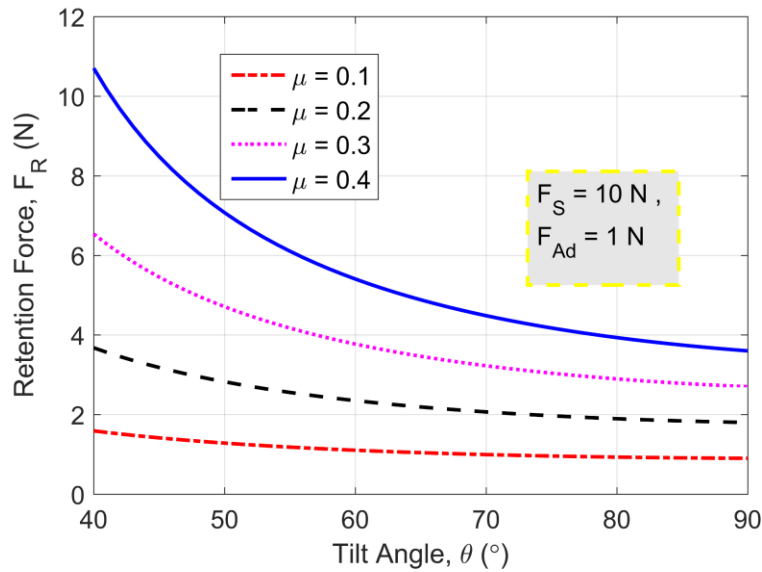


Figure 3-4: Retention force F_R versus tilt angle θ for a series of friction coefficients μ .

Figure 3-5 shows applications of the analytical model (i.e. Eqs. (1), (5), and (6)) for a laser-sintered Co-Cr clasp with a semicircular cross-section in molars and premolars. Figure 3-5(a) shows the relation between length, radius of cross-section and maximum stress in the clasp for a molar at a retention force of 10 N and different undercuts. Since a molar was considered, the radius of curvature r_i was set at 7 mm [97, 151, 152]. The figure demonstrates that increasing the radius of cross-section while maintaining the length reduces the stress in the clasp and results in less undercut needed. It also shows that, for a fixed cross-section, longer clasps need to engage deeper undercuts but will experience greater stresses. Typically, a buccal clasp arm should engage an undercut of 0.25 mm 0.25 mm if the clasp material is Co-Cr [140]. The retention force for a Co-Cr clasp engaging an undercut of 0.25 mm is between 8-10 N [92, 155]. The figure illustrates that

for an undercut of 0.25 mm, the optimal clasp length in molars is around 13 mm which requires a cross-sectional radius of 1.2 mm and results in a retention force of 10 N and a stress around 413 MPa.

Figure 3-5(b) shows the relation between length, radius of cross-section and stress for Co-Cr clasps in premolars at a retention force of 10 N and different undercuts. Since a premolar was considered, the radius of curvature r_i was set at 5 mm [97, 151, 152]. In general, similar trends are observed for premolars as compared with molars. However, higher stresses are associated with premolar clasps. For example, Figure 3-5(b) shows that to achieve a retention force of 10 N at 0.25 mm undercut, a clasp length of 9 mm can be used with a cross-sectional radius of 0.9 mm, but the resulting stress will be 674 MPa. Even a longer clasp (i.e. 10.5 mm) with a greater cross-sectional radius (i.e. 1.05 mm) will still result in a stress around 530 MPa, which is greater than the stress experienced by clasps in molars for the same undercut and retention.

Figure 3-5(c) & (d) show the relation between length, radius of cross-section and undercut at a stress of 400 MPa and different retention forces for Co-Cr circumferential clasps in molars and premolars, respectively. Both figures reveal that, for a specific cross-sectional radius, longer clasps can engage deeper undercuts at the expense of reducing retention while maintaining the same stress. On the contrary, increasing cross-sectional area at a fixed length adds greater retention while keeping the same stress but reduces the undercut. The figures also show that to engage a deeper undercut while keeping the same retention and stress, both the length and cross-sectional radius should be increased.

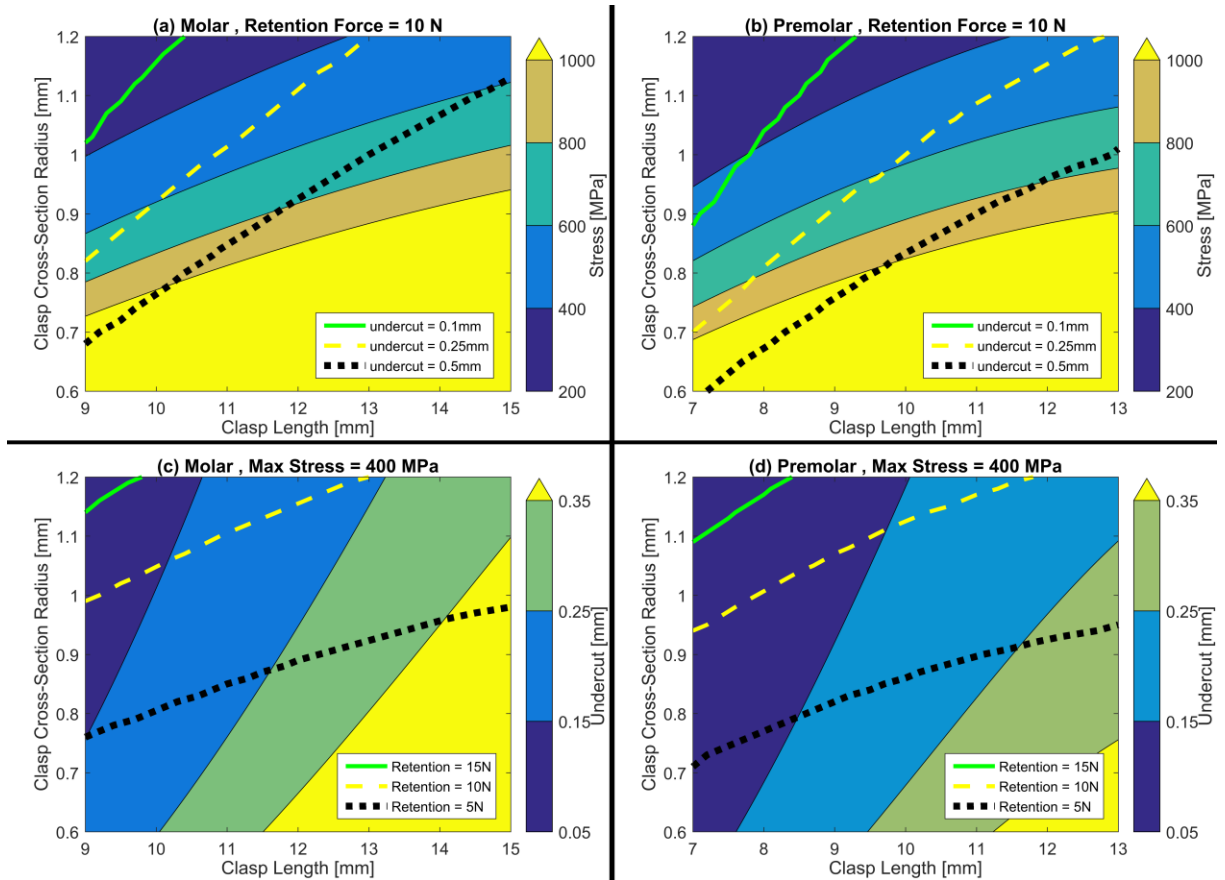


Figure 3-5: Design charts for laser-sintered Co-Cr clasps with a semicircular cross-section showing relation between clasp length and radius of cross-section with (a) stress and undercut for a molar; (b) stress and undercut for a premolar; (c) undercut and retention force for a molar; (d) undercut and retention force for a premolar. The solid green, yellow dashed and black short dashed lines correspond to the undercut in (a) and (b), and to the retention force in (c) and (d).

3.3.2 FEA

Figure 3-6(a) displays the contours of the direct tensile stress due to bending for a circumferential clasp with a semicircular cross-section in a premolar. The maximum stress with value of 787 MPa is located at the inner surface of the clasp shoulder. The stress gradually decreases approaching a value near zero at the clasp free end where the force is applied. Figure 3-6(b) shows the deflection contours. The deflection is zero at the clasp shoulder. It increases gradually until reaching a maximum value of 0.28 mm at the clasp free end.

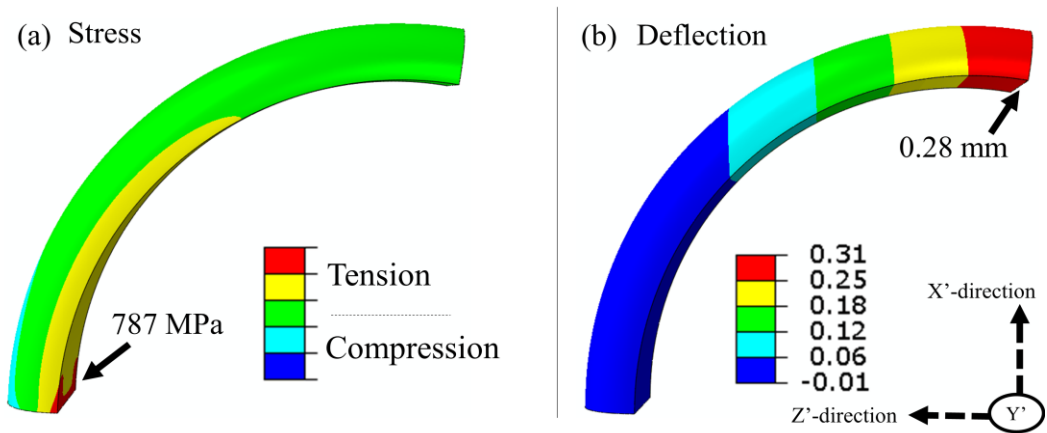


Figure 3-6: FEA of a circumferential laser-sintered Co-Cr clasp for a premolar with semicircular cross-section showing (a) Tensile stress [MPa]; and (b) Deflection [mm] in the x'-direction.

3.3.3 Experimental Validation of Analytical Model

Figure 3-7 shows comparisons between the analytical model predictions and experimental results for clasp retention forces on teeth of both the maxillary and mandibular arches. Four types of teeth were considered: 1st premolar, 2nd premolar, 1st molar, and 2nd molar. The x-axis represents the retention force predicted by the analytical model, while the y-axis represents the retention force measured experimentally. The exact values for predicted and measured retention forces are listed in Table 3-2 in the supplementary material. In Figure 3-7, the dashed line indicates the ideal case where the predicted value equals the measured one. Overall, we see that a good agreement has been achieved between the model predictions and experimental data. The root mean square error between the model predictions and the experimental data was 0.39 N. The coefficient of determination, which is a statistical measure of how successful the model was in explaining the variation of experimental data, was 0.91 indicating that the model explains 91% of the total variation in the data about the average. As shown in Figure 3-7, the lower 2nd premolar and the upper 1st molar presented the greatest measured and predicted retention forces, whereas the 1st upper and lower premolars had the lowest measured and predicted retention forces. However, there

existed slight discrepancy in the measured and predicted forces probably due to possible measurement errors for undercut and clasp dimensions.

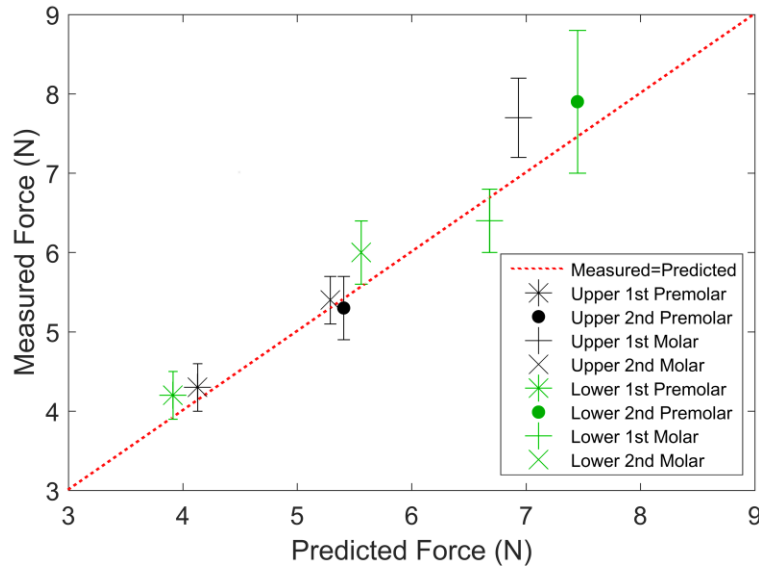


Figure 3-7: Experimental validation of the analytical model showing measured retention force versus predicted retention force. The dashed line indicates when the measured force equals the model predicted one, while the symbols denote the retention forces on different teeth.

3.4 Discussion

Using the laser-sintered Co-Cr alloy as a representative clasp material, our results demonstrated that the dimensions of clasps can be optimized to prevent stress from reaching the fatigue failure limit. Although the same mechanics-based model can be used for designing cast clasps, it is more suitable for laser-sintered clasps due to the better precision of laser-sintering [70]. Based on our results, design charts have been developed to guide the design of clasp length and cross-sectional radius. For clasps made from laser-sintered Co-Cr, the clasp material exhibits a yield strength of 500 MPa [156] and a fatigue strength around 400 MPa for 7.2 million cycles at 0 – 400 MPa load range and 20 Hz [150]. Based on that, a maximum design stress σ_{max} of 400 MPa is considered safe to avoid plastic deformation or fatigue failure. Based on that Figure 3-5(c) &

(d) could be used by dental technicians and designers to select the clasp geometry based on the measured undercut of the tooth.

Our findings suggest that circumferential clasps in smaller teeth such as premolars would be more susceptible to plastic deformation and fatigue failure than in larger teeth such as molars. This is because circumferential clasps with smaller radius of curvature such as those in premolars would experience higher stresses than those in molars. For instance, the results showed that the stress experienced by circumferential clasps in molars was 413 MPa, whereas it was 674 MPa in premolars which exceeds the fatigue strength of laser-sintered Co-Cr and is 48% higher than the stress in molar clasps for the same retention and undercut. Therefore, a gingivally-approaching design or wrought wire could be more suitable for premolars, which agrees with the opinion of prosthodontic experts [140, 157]. It is also noteworthy that the analytical model suggested a length of 13 mm for Co-Cr circumferential clasps in molars, whereas 58% of experts believe that clasps should be at least 15 mm in length if they are constructed in Co-Cr alloy [140]. Therefore, it could be argued that analytical modeling of laser-sintered clasps could help to safely decrease their required length.

The FEA results indicate that the stress at the clasp shoulder is greater than the yield stress of laser-sintered Co-Cr, which suggests that plastic deformation could occur for circumferential clasps in premolars. By comparing the maximum stress calculated by the analytical model, i.e. 674 MPa, with the bending tensile stress computed by FEA, i.e. 787 MPa, we find a difference error of 15%. The error was less, around 11%, when comparing the undercut predicted by the analytical model, i.e. 0.25 mm, with the value computed by FEA, i.e. 0.28 mm. There could be several reasons for this discrepancy including, but not limited to, the assumption of point loading which could cause severe distortion in the finite elements around the loading point.

The experiments showed that, in the mandibular arch, the 2nd premolar had the greatest measured retention force because it combined a short length and a deep undercut. For the maxillary arch, the 1st molar had the greatest retention due to its relatively greater radius of curvature and shorter length while engaging a deep undercut. The clasp placed on the 1st premolar had the smallest cross-sectional radius while engaging a smaller undercut and radius of curvature. Therefore, it provided the smallest retention force for both maxillary and mandibular arches. No significant twisting of the clasp about its shoulder was observed in the experiment which explains the good agreement between the experimental and analytical results. In fact, in the analytical and FE models, the clasp shoulder was assumed to move, with the rest of the clasp, only along the y'-direction which agrees well with our experimental set-up.

The analytical model presented in this manuscript can be expanded to include other types of cross-sections and the effect of tapering could also be included. It is worthy to note the simplifications of the analytical and FE models which include the assumption that the clasp lies on a single plane and the uncertainty in the frictional coefficient. Therefore, uncertainty in the predictions could be anticipated from a quantitative point of view. However, a small variation in the friction coefficient would not significantly influence the results. For example, Figure 3-4 shows that at a tilt angle of 80°, an increase of friction coefficient from 0.3 to 0.4 would increase the retention force by 1 N. In addition, only circumferential clasps on molar and premolar teeth were considered in this study. Overall, the proposed theoretical framework provides an acceptable qualitative agreement with experiments without violating the common principles governing the dependency of clasp retention on metal stiffness, clasp geometry, and physical and frictional forces. Further, the proposed framework forms a first step that would lead to a more realistic model in the future.

3.5 Conclusion

The proposed analytical model, within its limitations, provided acceptable qualitative and quantitative guidelines for designing circumferential clasps in molar and premolar teeth. The results suggested that circumferential clasps constructed in laser-sintered Co-Cr alloys could be safely designed for molars, but they should be avoided in premolars.

3.6 Supplementary Material

3.6.1 Retention Force model

Assuming the clasp is disengaged under quasi-static conditions, the static equilibrium approach can be used to determine the retention force F_R . Consider the force balance along the y' -axis in Figure 3-1, we have:

$$F_{fr} = F_R \sin \theta \quad (\text{S.7})$$

where F_{fr} is the friction force such that:

$$F_{fr} = \mu F_N \quad (\text{S.8})$$

The normal force F_N can now be expressed in terms of the angle θ , the friction coefficient μ , and retention force F_R by combining the preceding two equations:

$$F_N = \frac{F_R \sin \theta}{\mu} \quad (\text{S.9})$$

By considering the equilibrium of forces along the x' -axis in Figure 3-1, the resulting spring force responsible for deforming the clasp F_S can be expressed as:

$$F_S = F_N - F_{Ad} - F_R \cos \theta \quad (\text{S.10})$$

By substituting the value of F_N , the spring force F_S can be expressed in terms of the angle θ , the friction coefficient μ , the adhesion force F_{Ad} , and the retention force F_R :

$$F_S = F_R \left(\frac{\sin \theta}{\mu} - \cos \theta \right) - F_{Ad} \quad (\text{S.11})$$

Deflection and maximum stress in circumferential clasps:

The deflection of a circumferential clasp is calculated based on Castigliano's theorem [106, 107]:

$$\delta = \int_0^\varphi \frac{M}{EI} \frac{dM}{dF_S} r_c d\alpha \quad (\text{S.12})$$

The bending moment M in the clasp was calculated as (see Figure 3-2 for a visual explanation of the relevant angles and clasp geometry):

$$M = F_S (r_c \cos \alpha - r_c \cos \varphi) = F_S r_c (\cos \alpha - \cos \varphi) \quad (\text{S.13})$$

Substituting the moment expression from Eq. (S.13) in Eq. (S.12) gives:

$$\delta = \int_0^\varphi \frac{F_S r_c^3 (\cos \alpha - \cos \varphi)^2}{EI} d\alpha = \frac{F_S}{E} \int_0^\varphi \frac{r_c^3 (\cos \alpha - \cos \varphi)^2}{I} d\alpha \quad (\text{S.14})$$

For a circumferential clasp with half-round cross section [147]:

$$I = \left(\frac{\pi}{8} - \frac{8}{9\pi} \right) c^4 = 0.1098c^4 \quad (\text{S.15})$$

$$r_c = r_i + \frac{4c}{3\pi} \quad (\text{S.16})$$

where c is the radius of the half-round cross-section. By substituting Eqs. (S.15) and (S.16) and the expression $\varphi = \frac{L}{r_i}$ in Eq. (S.17):

$$\delta = \frac{F_S}{E} \int_0^{\frac{L}{r_i}} \frac{\left[\cos \alpha - \cos \left(\frac{L}{r_i} \right) \right]^2 \left(r_i + \frac{4c}{3\pi} \right)^3}{0.1098c^4} d\alpha \quad (\text{S.17})$$

The maximum bending normal stress occurs at the clasp's inner curvature and can be calculated based on Euler–Bernoulli elastic curved beam theory [107]:

$$\sigma_{Bend,max} = \left[\frac{M(r_n - r_i)}{Aer_i} \right]_{max} \quad (\text{S.18})$$

where $\sigma_{Bend,max}$ is the maximum bending normal stress, A is the cross-section area of the clasp, r_i is the inner radius of curvature, and e is the eccentricity which is the distance between the radius of curvature of neutral axis r_n and the radius of curvature of the centroidal axis r_c . The cross-section area A is defined as:

$$A = \frac{\pi c^2}{2} \quad (\text{S.19})$$

The radius of curvature of neutral axis is

$$r_n = \frac{A}{\int_{r_i}^{r_o} \frac{dA}{r}} \quad (\text{S.20})$$

The eccentricity e is approximated as [147]:

$$e = r_c - r_n \cong \frac{I}{Ar_c} \quad (\text{S.21})$$

Substituting Eqs. (S.22) & (S.21) in Eq. (S.18) with assuming the bending normal stress peaks at the clasp shoulder [92] (i.e. point A where $\alpha = 0$) and including the effect of direct normal stress at point A (i.e. $\sigma_N = F_S/A$), an expression for the maximum stress in the clasp is reached:

$$\sigma_{max} = \frac{M(r_n - r_i)}{Aer_i} + \frac{F_S}{A} = \frac{M(r_c - e - r_i)}{A\left(\frac{I}{Ar_c}\right)r_i} + \frac{F_S}{A} = \frac{M}{r_i} \left[\frac{4cr_c}{3\pi I} - \frac{1}{A} \right] + \frac{F_S}{A} \quad (S.23)$$

By substituting Eqs. (S.13), (S.15), and (S.19) into Eq. (S.23) (with $\cos \alpha = 1$):

$$\sigma_{max} = \frac{F_S r_c (1 - \cos \varphi)}{r_i} \left[\frac{4cr_c}{3\pi(0.1098)c^4} - \frac{2}{\pi c^2} \right] + \frac{2F_S}{\pi c^2} \quad (S.24)$$

By manipulating the terms in Eq. S.25 and substituting $\varphi = L/r_i$, an expression for the maximum stress in circumferential clasps with half-round cross sections is reached:

$$\sigma_{max} = \frac{F_S \left(r_i + \frac{4c}{3\pi} \right) \left[1 - \cos \left(\frac{L}{r_i} \right) \right]}{\pi r_i} \left[\frac{4 \left(r_i + \frac{4c}{3\pi} \right)}{3(0.1098)c^3} - \frac{2}{c^2} \right] + \frac{2F_S}{\pi c^2} \quad (S.25)$$

Eq. (S.25) provides the maximum stress as a function of clasp inner radius of curvature r_i , cross-sectional radius c , length L and spring force F_S . It is apparent from Eq. (S.25) that increasing the cross-sectional radius c decreases the maximum stress whereas increasing the spring force F_S or length L increases the stress. Eq. (S.17) indicates that undercut δ decreases with increasing the cross-sectional radius c and elastic modulus E of the clasp and increases as the spring force F_S , the inner radius of curvature r_i , or the length L increases.

3.6.2 Relation between retention force, spring force and coefficient of friction

Figure 3-8 shows the relation between the retention force F_R , the spring force F_S which represents the stiffness of the clasp and hence could be also called the stiffness force, and the coefficient of friction μ for a tilt angle $\theta = 75^\circ$ and adhesion force $F_{Ad} = 1\text{ N}$. The value of θ varies slightly among patients and depends also on the type of tooth. This angle was specified based on measurements made in molars and premolars of the dentofrom model. The figure shows that the retention force increases linearly with increasing the spring/stiffness force. Also, increasing the friction coefficient results in a greater retention force.

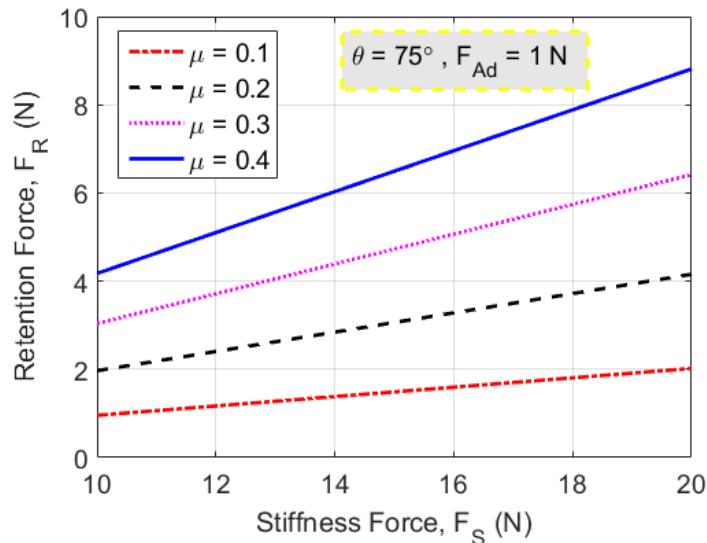


Figure 3-8: Retention force F_R versus spring/stiffness force F_S for a series of friction coefficients μ .

3.6.3 Mesh sensitivity analysis

A mesh sensitivity analysis was conducted to ensure mesh-independent results for the stress and deflection fields of the clasp. The size of elements was varied and the response of von Mises stress was monitored until convergence. An element size of 0.04 mm was selected which corresponds to 225 elements used in the finite element model.

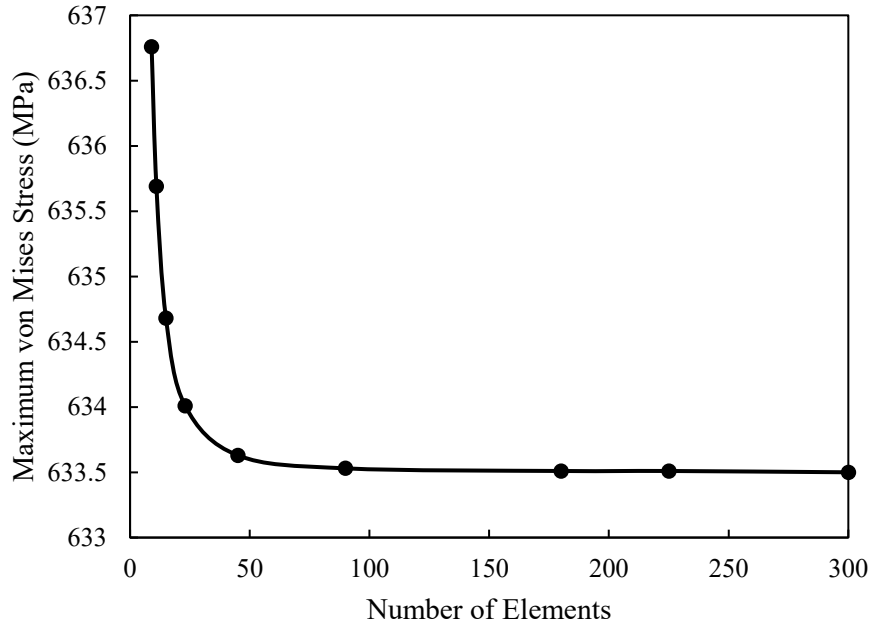


Figure 3-9: Mesh sensitivity analysis for clasp FE model showing convergence of von Mises stress after 50 elements.

3.6.4 Experimental validation of the analytical model

Table 3-1: Values used for experimental validation of the analytical model.

	Tooth type							
	1 st Premolar		2 nd premolar		1 st molar		2 nd molar	
	Upper	Lower	Upper	Lower	Upper	Lower	Upper	Lower
undercut [mm]	0.1	0.1	0.11	0.15	0.15	0.14	0.11	0.11
radius of curvature [mm]	5	5	5	5	7	7	7	7
clasp length [mm]	9.47	9.86	9.74	9.55	12.49	13.26	13.61	13.72
cross-section radius [mm]	0.96	0.98	1.04	1.03	1.21	1.3	1.34	1.36
tilt angle	78.9	79	78.5	78	78.1	80	83	80.8

Table 3-2: Measured and predicted retention forces for different tooth types.

	Tooth type							
	1 st Premolar		2 nd premolar		1 st molar		2 nd molar	
	Upper	Lower	Upper	Lower	Upper	Lower	Upper	Lower
Measured force [N]	4.3±0.3	4.2±0.3	5.3±0.4	7.9±0.9	7.7±5.5	6.4±0.4	5.4±0.3	6±0.4
Predicted force [N]	4.1	3.9	5.4	7.5	6.9	6.9	5.3	5.6

4 Shape Optimization

In many cases it is difficult to produce a closed-form analytical model to optimize structural designs. Therefore, this chapter explored a gradient-free design optimization method. A practical case study was considered with an objective to improve metal/polymer interfacial strength and stiffness in dental and orthopedic prostheses. To achieve this, a bioinspired shape optimization algorithm was used to suggest interlocking designs of metal features to be additively manufactured on metal surfaces through laser-sintering. This interlocking design should enhance the strength and stiffness of the metal/polymer interface, which should also lead to decreasing gap formation (the average displacement of polymer at the interface).

- This chapter has been published in *Acta biomaterialia*, 80, 425-434.

DOI: <https://doi.org/10.1016/j.actbio.2018.09.029>

Bioinspired and optimized interlocking features for strengthening metal/polymer interfaces in additively manufactured prostheses

Ammar A. Alsheghri ^a, Omar Alageel ^{b,c}, Mohamed Amine Mezour ^b, Binhan Sun ^a, Stephen Yue ^a, Faleh Tamimi ^{b, 1}, Jun Song ^{a, 4}

^a Department of Mining and Materials Engineering, McGill University, Montreal, QC, Canada

^b Faculty of Dentistry, McGill University, Montreal, QC, Canada

^c College of Applied Medical Sciences, King Saud University, Riyadh, Saudi Arabia

Corresponding Author complete address: Department of Mining and Materials Engineering, McGill University, 3610 University Street, Montreal, QC, Canada, H3A 2B2

Email: jun.song2@mcgill.ca

Tel.: 001-514-398-4592

FAX: (514) 398-4492

Funding: This work was supported by 3DRPD Inc., Montreal, Quebec, Canada; Fonds de recherche du Québec – Nature et technologies (FRQNT), McGill Engineering Doctoral Award (MEDA), and Natural Sciences and Engineering Research Council of Canada [grant number NSERC CRD 469834].

⁴ The author to whom corresponding should be addressed.

E-mail addresses: ammar.alsheghri@mail.mcgill.ca (A. A. Alsheghri), omar.alageel@mail.mcgill.ca (O. Alageel), mohamed.mezour@mail.mcgill.ca (M. Mezour), binhan.sun@mail.mcgill.ca (B. Sun), steve.yue@mcgill.ca (S. Yue), faleh.tamimimarino@mcgill.ca (F. Tamimi), jun.song2@mcgill.ca (J. Song).

Abstract

Biomedical and dental prostheses combining polymers with metals often suffer failure at the interface. The weak chemical bond between these two dissimilar materials can cause debonding and mechanical failure. This manuscript introduces a new mechanical interlocking technique to strengthen metal/polymer interfaces through optimized additively manufactured features on the metal surface. To reach an optimized design of interlocking features, we started with the biomimetic stress-induced material transformation (SMT) optimization method. The considered polymer and metal materials were cold-cured Poly(methyl methacrylate) (PMMA) and laser-sintered Cobalt-Chromium (Co-Cr), respectively. Optimal dimensions of the bioinspired interlocking features were then determined by mesh adaptive direct search (MADS) algorithm combined with finite element analysis (FEA) and tensile experiments such that they provide the maximum interfacial tensile strength and stiffness while minimizing the stress in PMMA and the displacement of PMMA at the Co-Cr/PMMA interface. The SMT optimization process suggested a Y-shape as a more favorable design, which was similar to mangrove tree roots. Experiments confirmed that our optimized interlocking features increased the strength of the Co-Cr/PMMA interface from 2.3 MPa (flat interface) to 34.4 ± 1 MPa, which constitutes 85% of the tensile failure strength of PMMA (40.2 ± 1 MPa).

Keywords

Metal/Polymer Interface; Biomimetic Design; Interlocking Features; Finite Element Analysis (FEA); Additive Manufacturing.

4.1 Introduction

Biomedical devices combining polymers with metal alloys often suffer from mechanical failure at the metal/polymer interface [158-160]. For example, dental prostheses and orthopedic devices, in which metal frameworks are joined with acrylic resin bases, present a weak bond between these components that can cause debonding and subsequent catastrophic mechanical failure at the metal/polymer interface [87, 160].

Poly(methyl methacrylate) (PMMA) is extensively used for dental prostheses as well as in orthopedic devices because of its biocompatibility, excellent esthetic, and mechanical properties [161]. Metal frameworks are commonly made from Cobalt-Chromium (Co-Cr) alloys because of their suitable cost, excellent mechanical properties, corrosion resistance, and biocompatibility [82]. The tensile strength between PMMA and grit-blasted Co-Cr is only about 5 MPa [162], possibly due to the weak acid-base bond PMMA forms with metal oxide [163]. Therefore, mechanical and chemical methods have been explored to enhance the binding of metals with PMMA [111, 164-166].

The highest reported tensile strength between PMMA and sandblasted metal using chemical bonding agents was about 23 MPa [165], which is still lower than stresses encountered in load-bearing biomedical applications. Consequently, further enhancement of the metal/polymer interface strength is necessary. Ideally the metal/polymer interface strength should be as close as possible to the tensile failure strength of the polymer, e.g., being around 65 MPa in the case of PMMA [167]. Another method to achieve the strength enhancement is to incorporate mechanical connector designs as forms of mechanical retention between acrylic resin bases and denture metal frameworks [111].

Different surface topographies and designs have been proposed and tested to strengthen the metal/polymer retention [81, 111, 168, 169]. For example, preformed retention mesh [81], surface beads [168], and rough surface finish [169] have been used to strengthen the bond between PMMA and the metal foundation in dental prostheses, fixed prosthodontics, and cemented total hip replacements, respectively. However, despite the well documented advantage of such retention methods, optimization and improvements have been limited by the available manufacturing technology. Recent developments in 3D printing technology such as additive manufacturing using laser-sintering provide great versatility and flexibility in fabricating metallic interlocking retention features of complex designs, which was not feasible with traditional casting methods [70]. Consequently, there is timely need of optimized designs for such metallic interlocking connectors.

Geometrical structures in nature serve as a source of bio-inspiration for designing robust interfaces that bond together different material phases [127, 129]. There has been considerable interest in the application of biomimicry in structural topology to determine the most efficient material distribution in structural design of multi-materials [29]. Shape optimization using Stress-induced Material Transformation (SMT) is one technique that mimics the adaptive growth of biological structures such as trees and bones [33]. It is used to determine a rough but efficient layout of materials in a structure and thus provides a draft design from which the optimal shape could be obtained [33].

The aim of this manuscript is to improve the strength of metal/polymer interfaces (i.e. Co-Cr/PMMA) through mechanical means of retention. The first objective is to obtain a bioinspired preliminary metal interlocking feature by the SMT shape optimization method and then further optimize it through mesh adaptive direct search (MADS) algorithm. Both techniques are implemented through finite element analysis (FEA). The second objective is to additively

manufacture the optimized metal designs by laser-sintering, combine the produced metal samples with cold-cured PMMA, and then experimentally test the specimens by tensile testing.

4.2 Materials and Methods

4.2.1 2D FEA

The FEA was performed using commercial software Abaqus (Dassault Systems Simulia Corporation, Johnston, RI, USA). A static linear analysis was performed such that both materials were considered linear elastic throughout the entire deformation. This assumption is reasonable for PMMA as a brittle material in non-failure conditions [170], and for Co-Cr as a ductile material prior to yielding. The model parameters used for PMMA were: elastic modulus $E = 2.4 \text{ GPa}$ [82, 171] and Poisson's ratio $\nu = 0.4$ [172], whereas for Co-Cr: $E = 200 \text{ GPa}$ [70] and $\nu = 0.33$ [153]. Surface-to-surface contact with friction behaviour between Co-Cr features and corresponding PMMA surfaces was assumed with a friction coefficient of 0.35 [173]. A 2D geometry was considered for the structure with a width of 5.5 mm and thicknesses of 1 mm and 2 mm for Co-Cr and PMMA, respectively (see Figure 4-1(c)). A velocity boundary condition of 10 mm/min was applied at the top surface of PMMA for a period of 0.1 sec whereas the lower surface of the Co-Cr was fixed. Plane stress quadrilateral elements with a thickness of 1 mm, 8 nodes, and quadratic geometric accuracy were used to mesh the metal and polymer parts. An element size of 0.02 mm was selected based on a mesh sensitivity analysis. The maximum values for von Mises and peak maximum principal stresses were recorded during the analysis step in Co-Cr and PMMA, respectively. The displacement of PMMA at the interface was calculated by averaging the displacements of PMMA nodes located on the yellow lines in Figure 4-1(c).

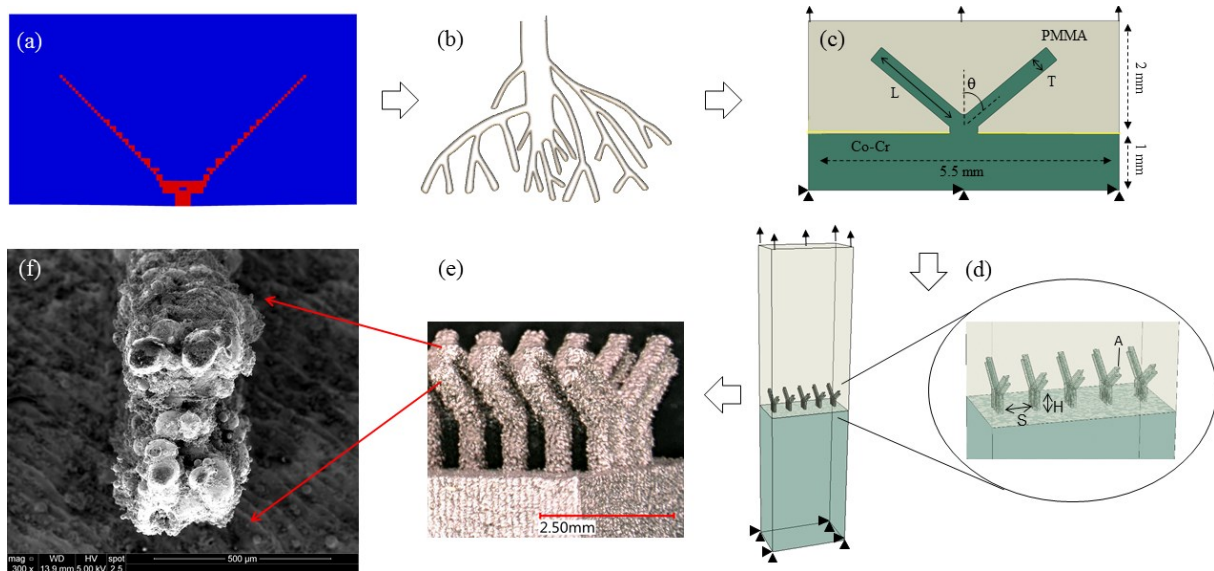


Figure 4-1: Co-Cr/PMMA interlocking feature design inspired by (a) shape optimization through stress-induced material transformation (SMT), which looks similar to a branch of (b) mangrove prop roots, (c) 2D Y-shape geometry with design variables and boundary conditions, (d) 3D geometry with design variables, (e) digital microscope image of additively manufactured specimen using laser-sintering, and (f) SEM image of the feature cross-sectional area.

4.2.2 Optimization procedures

Shape optimization using Stress-induced Material Transformation (SMT) was conducted to reach a bioinspired preliminary design from which optimized interlocking features could be obtained. The SMT method, which mimics the adaptive growth of biological structures such as bones and trees, was implemented using 2D FEA [29, 33] (details provided in supplementary materials). Starting from the bioinspired preliminary design obtained by shape optimization (see Figure 4-1(a)), which suggested a Y-shaped interlocking feature, mesh adaptive direct search (MADS) optimization was conducted to obtain optimal dimensions for the features using NOMADm, a suite of MATLAB for numerically solving nonlinear and mixed variable optimization problems [174-176]. MADS uses a derivative-free method to converge to a point that satisfies certain optimality conditions (i.e. minimize the objective function) [174]. The simulation model, which was implemented through 2D FEA, was carried out by coupling MATLAB with Abaqus. The selected design variables were length (L), thickness (T), and angle (θ) (Figure 4-1(c)).

The objective function was selected to be the inverse of stiffness [mm/N], with stiffness defined as sum of reaction forces at the metal base divided by average displacement of the top polymer surface. The imposed constraints were von Mises stress in metal ≤ 400 MPa, maximum principal stress in polymer ≤ 40 MPa, and average displacement of polymer nodes at interface ≤ 6 μ m. The ranges of design variables were 0.35-0.55 mm for thickness (T), 50°-80° for angle (θ), and 0.5-2 mm for length (L). The starting values for design variables were: T = 0.5 mm, $\theta = 75^\circ$ and L = 1.5 mm.

The optimal design model was:

$$\text{minimize } f(L, T, \theta; \text{load \&BCs}) = \frac{1}{\text{stiffness}} = \frac{\text{Avg displacement of top polymer surface [mm]}}{\text{sum of reaction forces at metal base [N]}}$$

subjected to the constrains of:

$$\text{polymer displacement at interfcce}(L, T, \theta, \text{load \&BCs}) \leq 6 \mu\text{m}$$

$$\text{von Mises stress in metal}(L, T, \theta, \text{load \&BCs}) \leq 400 \text{ MPa}$$

$$\text{maximum principal stress in polymer}(L, T, \theta, \text{load \&BCs}) \leq 40 \text{ MPa}$$

After reaching optimal dimensions for L, T, and θ , parametric studies using 2D FEA were performed to illustrate the effect of varying the design variables (i.e. L, T, and θ) on the maximum von Mises stress in Co-Cr, the peak maximum principal stress in PMMA, stiffness, and average displacement of PMMA at the Co-Cr/PMMA interface.

4.2.3 3D FEA

Parametric studies using 3D FEA were performed to illustrate the effect of varying additional design variables on the maximum von Mises stress in Co-Cr, stiffness, and average displacement of PMMA at the Co-Cr/PMMA interface. The considered design variables were the feature's cross-sectional area (A), the spacing between features (S), and the feature's neck height (H) as

shown in Figure 4-1(d). The geometry considered for 3D FEA had dimensions of $5.5 \times 10 \times 20 \text{ mm}^3$ for PMMA and $5.5 \times 10 \times 18 \text{ mm}^3$ for Co-Cr. To convert 2D to a 3D geometry, an I-shaped cross-section was adopted for the interlocking features due to its relatively high second moment of area and bending resistance while providing a large surface area for Co-Cr to interact and bond with PMMA [70, 75, 106]. The interlocking features were implemented at the top surface of the Co-Cr part and duplicated at the lower surface of the PMMA part as shown in Figure 4-1(d) and Figure 4-6. Tetrahedral elements with 4 nodes and linear geometric accuracy were used for meshing. A velocity boundary condition of 10 mm/min was applied at the top surface of PMMA, whereas a fixed boundary condition was used at the bottom surface of Co-Cr. The reaction forces were recorded at the bottom surface of the Co-Cr component. The simulation ran until failure of the specimen. The structure was assumed to fail when the sum of the reaction forces equals the experimental failure force. Different failure loads were used for the different designs in the parametric studies. The stiffness was calculated by dividing the force at failure by the displacement of the top PMMA surface at failure. The average PMMA displacement at the interface was recorded at the time of failure by averaging the displacements of PMMA nodes at the interface. The average von Mises stress in Co-Cr interlocking features was also calculated at the point of failure.

4.2.4 *Sample Preparation*

Experiments were performed on specimens composed of the Co-Cr alloy and PMMA acrylic resin to study the effect of spacing, neck height, and cross-sectional area of the interlocking features on the interfacial strength of the Co-Cr/PMMA structure. Co-Cr specimens with interlocking features were designed in a computer-aided design (CAD) software and then additively manufactured by selective laser-sintering (SLS) at the prototyping centre (3DRPD Inc.,

Montreal, QC, Canada). The specimens were processed using the PXM system equipped with a roller to compact the powder (Phenix Systems, Riom, France), with fibre laser power of 300 W and wavelength of 1070 nm. The chemical composition of the Co-Cr powder as provided by the manufacturer is 63% Cobalt (Co), 29% Chromium (Cr), 5.5% Molybdenum (Mo), <1% Silicon (Si), <1% Manganese (Mn), and <1% Iron (Fe). The particle size of the Co-Cr powder (ST2724G-A, Sint-Tech; Clermont-Ferrand, France) are in the range of 6-22 μm . The layer thickness, laser scan speed, and building direction were 30 μm , 5-7 m/s, and 90°, respectively.

To combine PMMA acrylic resin with the laser-sintered Co-Cr specimens, a custom-made mold was fabricated from silicone (Exaktosil N 21, Bredent, Germany). The Co-Cr specimen was placed in the mold, after which a mix of PMMA powder and MMA liquid monomer (Biocryl Resin Acrylic, Great Leakes, NY) with 1.6/1.0 vol. % was poured to fill the space in the mold [177]. The PMMA was left to set for five hours at room temperature and humidity. This procedure generated the test specimen, which was 63 mm long, 10 mm wide, and 5.5 mm thick, composed of bulk PMMA polymerized at one side and laser-sintered Co-Cr at the other side (Figure 4-1(d) and Figure 4-12).

4.2.5 *Mechanical Testing*

After complete setting of the acrylic resin, the interface strength of the Co-Cr/PMMA specimen was measured by tensile testing, with an MTS testing machine (MTS Systems Corp., Eden Prairie, Minnesota). A tensile force was applied to the specimen at a constant speed of 10 mm/min until fracture (Figure 4-12). Eleven different groups were considered for the experimental part: one group to measure the tensile failure strength of PMMA alone, one group to evaluate the strength of a control specimen with flat interface between Co-Cr and PMMA, eight groups contained interlocking feature designs at the interface to assess the influence of varying design variables on

the strength, and the last group contained a conventional bead design. The considered design variables' values for the interlocking feature design were 0.1, 0.5 and 1 mm for feature's neck height (H); 0.9, 1, 1.5 and 2 mm for spacing (S); and 0.09, 0.22 and 0.312 mm² for feature's cross-sectional area (A) as illustrated in Figure 4-1(d). Table 4-1 lists the different designs with their corresponding codes. The codes were assigned to represent the significant dimensions of each design. For example, A2H10S09 represents an interlocking feature with a cross-sectional area (A = 0.22 mm²), a neck height (H = 1 mm), and a spacing between features (S = 0.9 mm). The bead design had a bead diameter of 1 mm and a spacing between beads of 1.6 mm. The maximum force at failure was recorded by the machine. The strength of the Co-Cr/PMMA interface was calculated by dividing the maximum force by the cross-sectional area of the specimen (i.e. 55 mm²).

Table 4-1: Design variables' values for each considered design group

Group	Features' neck height (H) [mm]	Spacing between features (S) [mm]	Feature's cross-sectional area (A) [mm ²]
A1H10S09	1	0.9	0.09
A2H10S09	1	0.9	0.22
A3H10S09	1	0.9	0.312
A1H10S10	1	1	0.09
A1H05S10	0.5	1	0.09
A1H01S10	0.1	1	0.09
A1H10S15	1	1.5	0.09
A1H10S20	1	2	0.09

4.2.6 *Surface Analysis*

X-ray photo electron spectroscopy (XPS) was used to determine the surface composition and chemistry of the laser-sintered Co-Cr alloy (Thermo Fischer Scientific Inc., East Grinstead, UK). Images were taken for the interlocking features and the fractured surfaces using scanning electron microscopy (Inspect-50 field emission SEM, FEI Japan, at 10 kV operating voltage), digital microscopy (DM) (Keyence, Canada), and stereo microscopy (SM) (Olympus, Japan).

4.3 **Statistical Methods**

Statistical analysis to identify differences between groups with different design variables was done using a one-way analysis of variance (ANOVA) and Tukey HSD multiple comparison performed using SPSS Statistics software. The significance level was set at $p < 0.05$ (see Figure 4-14 in Supplementary Materials).

4.4 **Results**

4.4.1 *Optimization and 2D FEA*

Figure 4-1(a) and Figure 4-1(c) show the preliminary bioinspired interlocking feature shape provided by shape optimization using SMT from which an optimized design could be obtained (details provided in Figure 4-9 in Supplementary Materials). The mesh adaptive direct search (MADS) optimization algorithm provided optimal dimensions for the metal feature in Figure 4-1 (c) in terms of length (L), thickness (T), and angle (θ) after 94 function evaluations (see Figure 4-10 in Supplementary Materials), yielding $L = 1.8$ mm, $T = 0.55$ mm, and $\theta = 76^\circ$. The value of the objective function at convergence was 0.0013 mm/N indicating a maximum stiffness of 769 N/mm. The peak maximum principal stress in PMMA was 39.4 MPa, whereas the maximum von Mises stress in Co-Cr was 227 MPa. The average displacement of PMMA at the interface was 5.99 μm .

The results of the 2D FEA parametric study concerning the influence of design variables on the maximum von Mises stress in metal, the peak maximum principal stress in polymer, stiffness, and polymer displacement at the interface are presented in Figure 4-2. Increasing the tilt angle (θ) reduced the von Mises stress in Co-Cr and the PMMA displacement at interface but increased the peak maximum principal stress in PMMA (Figure 4-2(a) and (b)). The stiffness increased initially with increasing the tilt angle up to a value of 74° after which it decreased with further increase in the tilt angle (Figure 4-2(b)). In contrast, increasing the metal length (L) increased von Mises stress in the metal but reduced the peak maximum principal stress in the polymer, the stiffness, and the PMMA displacement at interface (Figure 4-2(c) and (d)). Figure 4-2(e) and (f) show that increasing the metal thickness (T) results in similar trends with increasing the tilt angle (θ). Figure 4-2(e) illustrates that increasing the thickness decreased the von Mises stress in the metal slightly and increased the peak maximum principal stress in the polymer. In addition, the stiffness was increased and the PMMA displacement at the interface was decreased as evident in Figure 4-2(f). In general, fluctuations are observed in the stress curves (non-smooth curves) because the mesh changes slightly as the geometry changes, which causes fluctuations in the stresses despite preserving the average element size of the mesh.

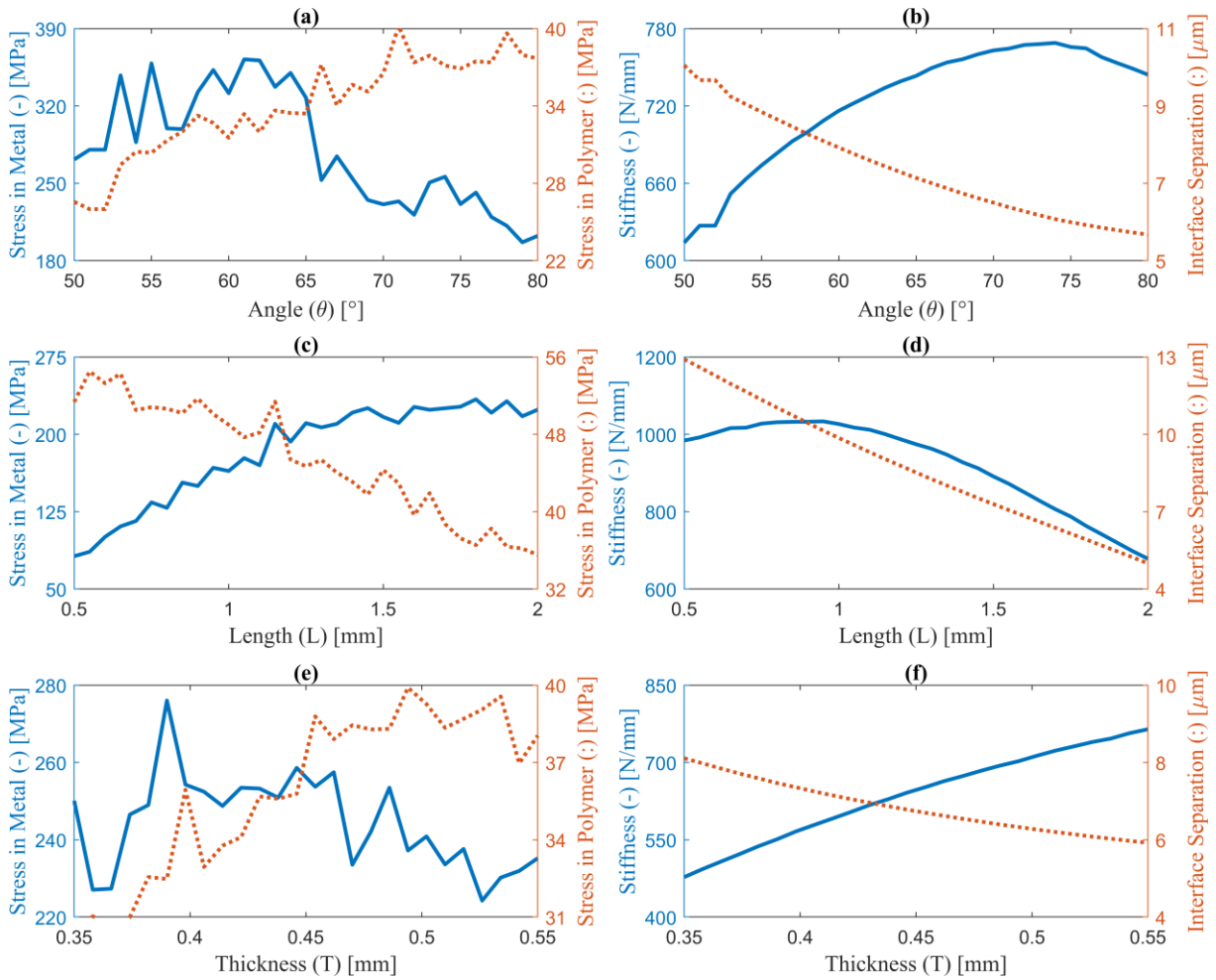


Figure 4-2: 2D FEA parametric study showing the effect of geometry on (a,c, & e) maximum von Mises stress in metal (solid line) and peak maximum principal stress in polymer (dotted line); and (b, d & f) stiffness of the structure (solid line) and polymer displacement at metal/polymer interface (dotted line): (a & b) effect of θ at $T = 0.55$ mm & $L = 1.8$ mm; (c & d) effect of L at $T = 0.55$ mm & $\theta = 76^\circ$; (e & f) effect of T at $\theta = 76^\circ$ & $L = 1.8$ mm.

4.4.2 Experimental Results

Experimental tensile tests of PMMA revealed a brittle failure with a nominal strength of 40.2 ± 1.3 MPa at failure, showing an increase in the tensile strength of the Co-Cr/PMMA specimen with increasing the feature's neck height (see Figure 4-3(a)). The strength decreased with increasing the spacing between the interlocking features (i.e. reducing the number of features) and decreasing the feature's cross-sectional area as evident in Figure 4-3(b) and Figure 4-3(c), respectively. A maximum tensile strength of 34.4 ± 1 MPa was achieved in design A2H10S09

followed by 31.9 ± 1.8 MPa in design A3H10S09. The tensile strength of A2H10S09 design was 12% greater than a conventional bead design, which yielded a strength of 30.5 ± 2.4 MPa. Nevertheless, the strength of both designs was less than the failure strength of PMMA (i.e. 40.2 ± 1.3 MPa) as shown in Figure 4-4(c). Table 4-3 lists the results for experimental nominal tensile strength of all considered groups and Figure 4-13 presents typical experimental load-displacement curves. In addition, the interlocking design increased the stiffness by 18% and lowered the PMMA displacement at the Co-Cr/PMMA interface by 70% compared with the conventional bead design, meanwhile no significant difference was found in the toughness of both designs as evident in Figure 4-4(a)-(d). Figure 4-5 shows stereo microscopy (SM) images of the fracture surfaces of interlocking feature A2H10S09 and bead designs. In both cases, an inclined adhesive/cohesive fracture occurred at the Co-Cr/PMMA interface.

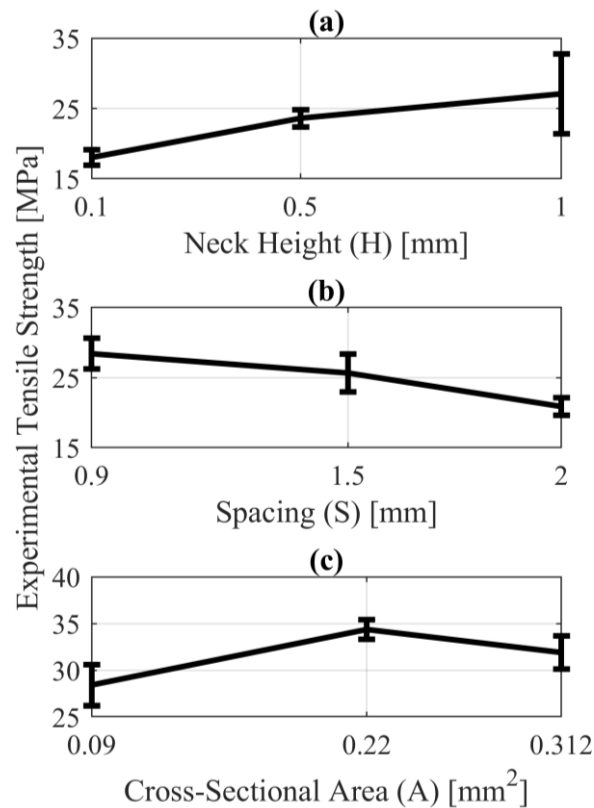


Figure 4-3: Effect of (a) features' neck height (H) at $S = 1$ mm & $A = 0.09$ mm²; (b) spacing between features (S) at $H = 1$ mm & $A = 0.09$ mm²; and (c) feature's cross-sectional area (A) at S

= 0.09 mm & H = 1 mm on experimental tensile nominal strength [MPa] of the Co-Cr/PMMA specimen.

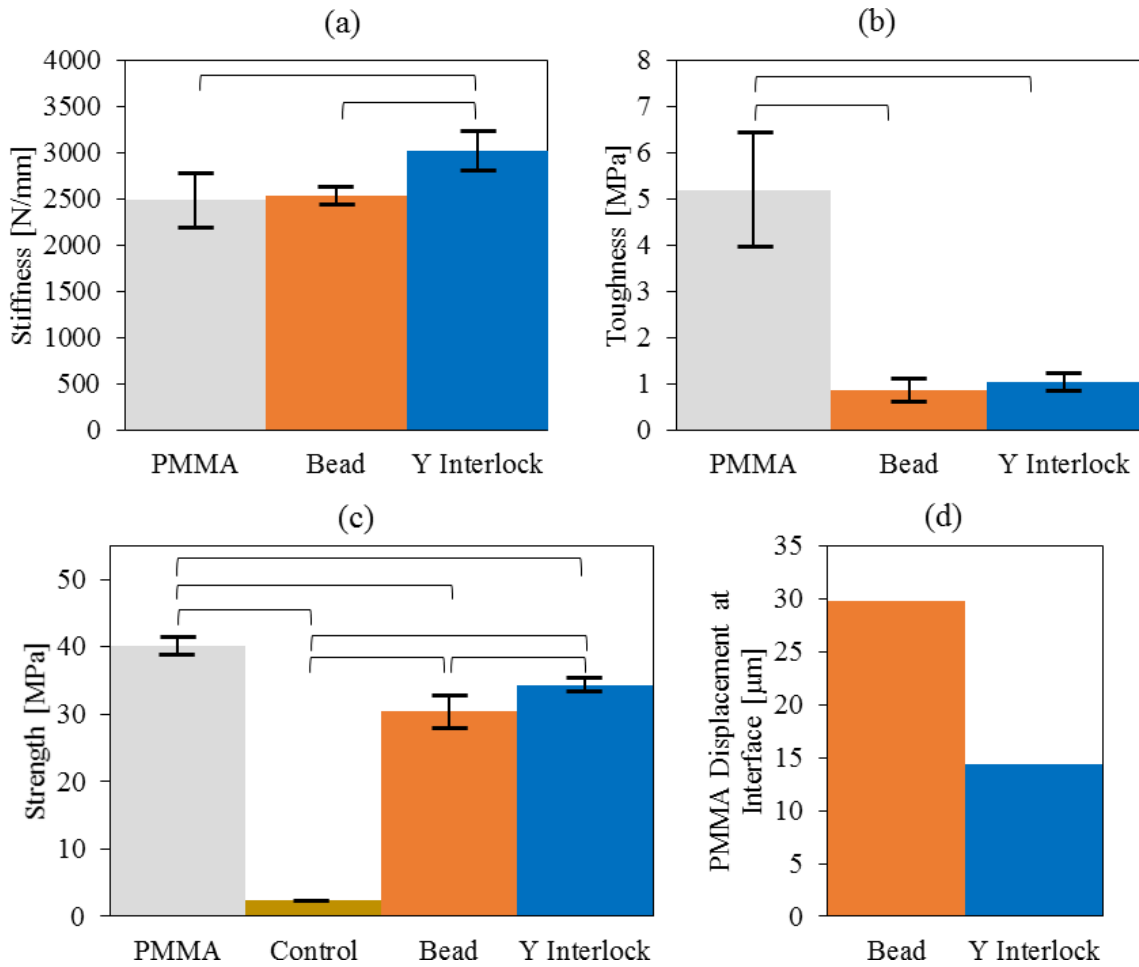


Figure 4-4: Comparison between experimental (a) stiffness, (b) toughness and (c) tensile strength of PMMA, control specimen, Y interlock (A2S09H10), and bead designs with one-way analysis of variance (ANOVA) and Tukey HSD multiple comparison at significance level of $p < 0.05$; and (d) displacement of PMMA at interface generated by FEA for Y interlock (A2S09H10) and bead designs.

4.4.3 3D FEA

Figure 4-6 shows SM images of the bead and interlocking designs ((a) and (b)) with 3D FEA results showing the contours of maximum principal stress in PMMA ((c) and (d)), displacement contours ((e) and (f)), and von Mises stress in Co-Cr ((g) and (h)). In particular, Figure 4-6(c) and (d) show that areas of high stresses in PMMA are located around the undercut regions for the bead design, whereas they are shifted towards the highest surface of contact for the interlocking design.

The 3D FEA revealed that both the von Mises stress in metal and the average displacement of PMMA at the interface increased with increasing the feature's neck height and spacing between features and decreased with increasing the cross-sectional area of the features as evident in Figure 4-7. However, the stiffness increased with increasing the cross-sectional area and height and decreased with increasing the spacing between features. In general, the experimental results were consistent with the computational ones shown in Figure 4-7. For example, the computational stiffness (Figure 4-7(b), (e), and (h)) followed the same trends of the experimental strength. In addition, both the experimental stiffness and the simulated stiffness, using FEA, follow the same trend as shown in Figure 4-8. A good linear fit was obtained between the simulated and experimental stiffnesses such that $Stiffness_{Sim} = 0.93 Stiffness_{Exp} + 3538$ with a coefficient of determination (i.e. R-squared value) of 0.75. Nevertheless, from a quantitative point of view, the experimental stiffness was lower because it incorporated the tensile machine displacement.

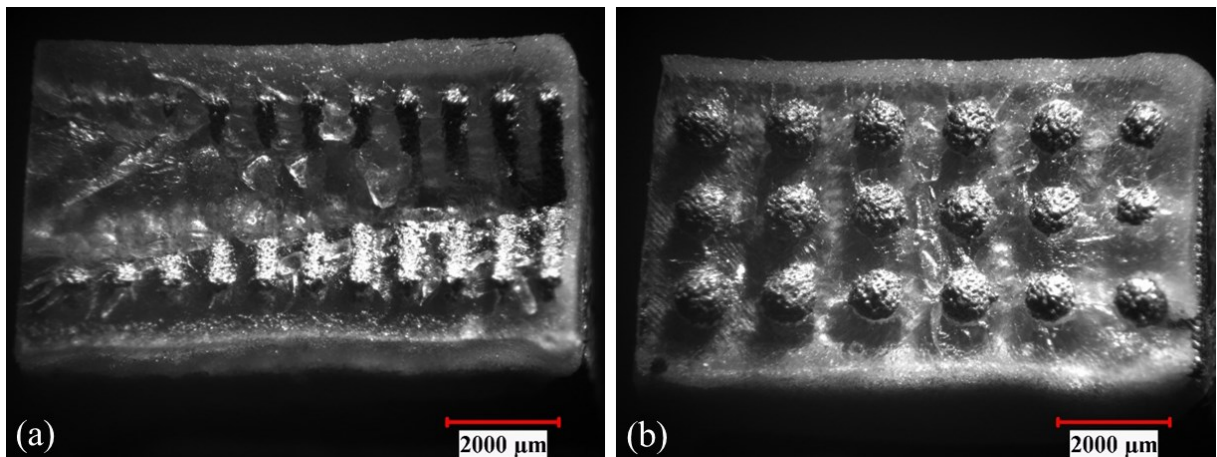


Figure 4-5: Stereo microscope images for fracture surfaces of tensile specimens: (a) interlocking feature design A2H10S09 and (b) Bead design.

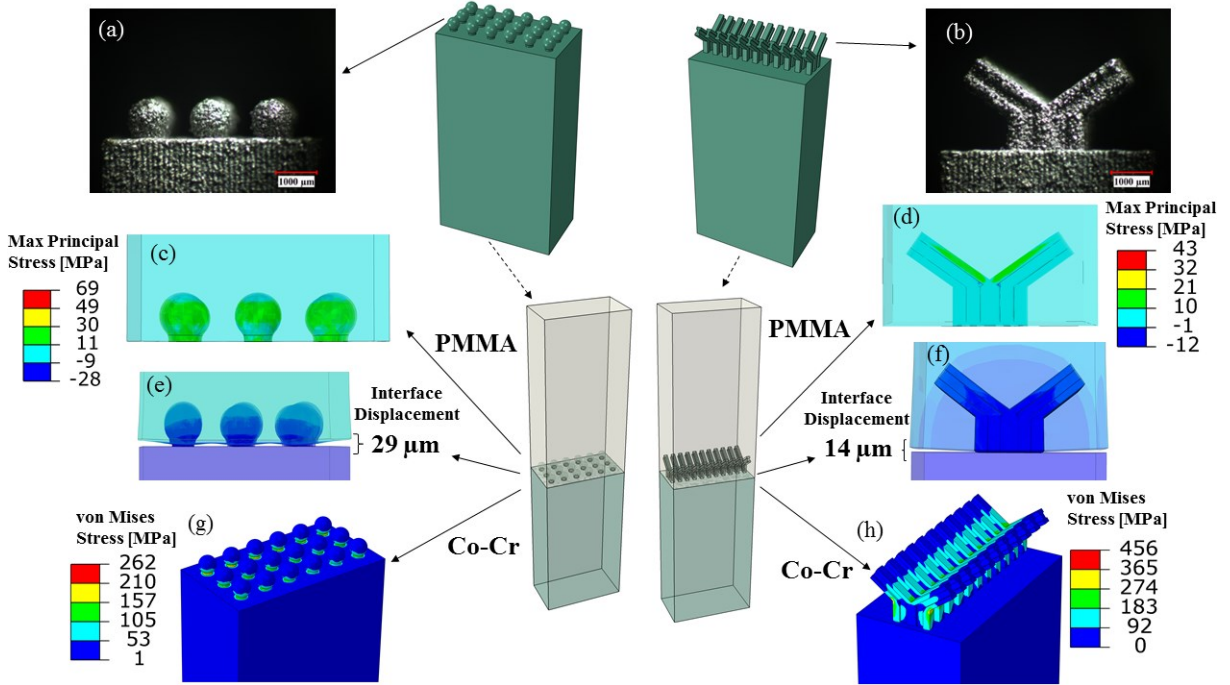


Figure 4-6: Stereomicroscope images of (a) bead design and (b) interlocking features A2H10S09 design; with 3D FEA showing the contours of (c & d) maximum principal stress in PMMA, (e & f) displacement contours, and (g & h) von Mises stress in Co-Cr.

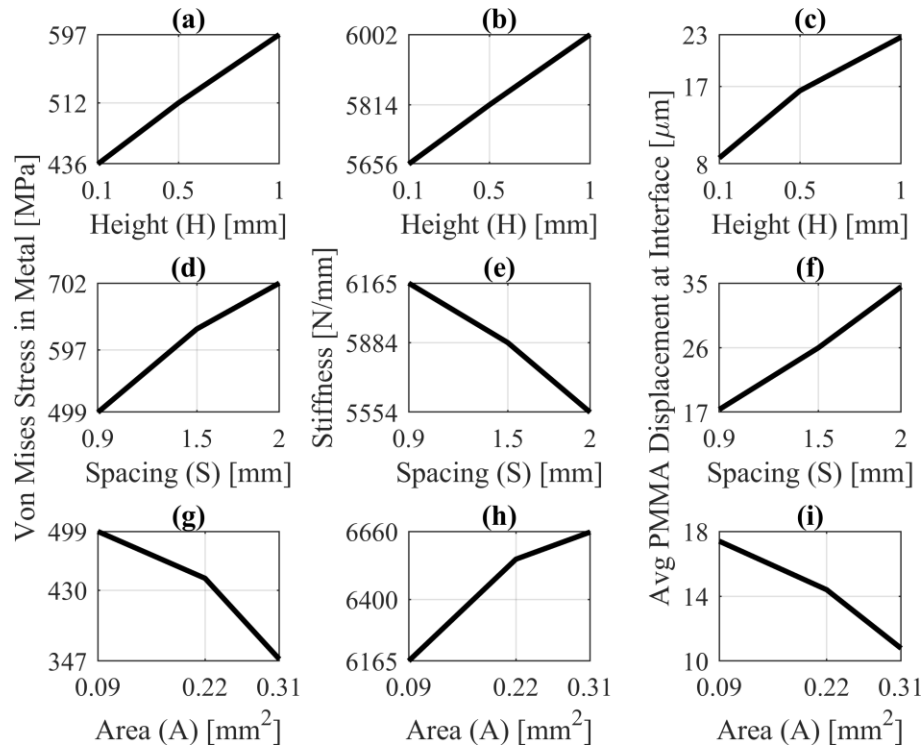


Figure 4-7: Results of 3D FEA showing the effect of interlocking features' neck height (H), spacing (S), and cross-sectional area (A) on (a, d & h) von Mises stress in metal; (b, e & h) stiffness; and (c, f & i) PMMA displacement at the interface of the Co-Cr/PMMA specimen. The considered

design values were $S = 1 \text{ mm}$ and $A = 0.09 \text{ mm}^2$ for (a, b & c); $H = 1 \text{ mm}$ and $A = 0.09 \text{ mm}^2$ for (d, e & f); $H = 1 \text{ mm}$ and $S = 0.9 \text{ mm}$ for (g, h & i).

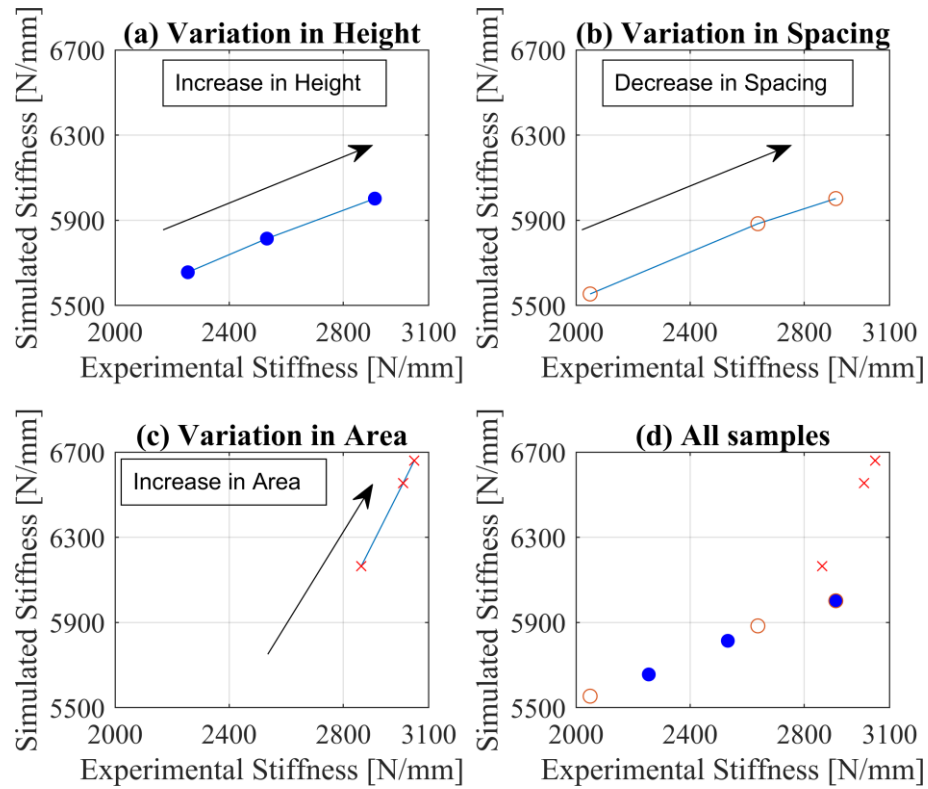


Figure 4-8: Comparison between stiffness values obtained from experiments with the ones calculated using 3D FEA. (a) Height (H) is varied at $S = 1 \text{ mm}$ & $A = 0.09 \text{ mm}^2$; (b) spacing between features (S) is varied at $H = 1 \text{ mm}$ & $A = 0.09 \text{ mm}^2$; (c) feature's cross-sectional area (A) is varied at $S = 0.09 \text{ mm}$ & $H = 1 \text{ mm}$; (d) all data are considered.

4.5 Discussion

This study was conducted to reach an optimized design of mechanical interlocking features for metal/polymer interfaces in dental and orthopedic prostheses. As shown in (see Figure 4-11 in Supplementary Materials), in contrast to the bulk laser-sintered Co-Cr alloy, the surface is composed of an external oxide layer that contains mainly O, Cr, and C that is likely originating for adventitious contaminants and resulting in a weak bond between the metal and polymer [178]. Therefore, we used bio-mimetic shape optimization (i.e. SMT), mesh adaptive direct search (MADS) optimization algorithm, FEA, and tensile experiments to optimize metal surface

interlocking features. The objective was to increase the strength and stiffness at the interface while maintaining acceptable levels of stress in both the metal and polymer and minimum micromotion of the polymer at the metal/polymer interface.

The bio-mimetic SMT technique suggested a Y-shape as a more favorable design, which looks similar to the roots of trees (Figure 4-1(b)), particularly the red mangrove prop roots. Mangrove roots, a group of trees and shrubs that grows in the intertidal zone of coastal areas, form inspiring arch shapes providing great potential for enhanced material designs [179]. Prop and drop arch-shaped roots anchor the red mangrove tree firmly in the muddy soil providing a sturdy support for the tree [179, 180]. The 2D FEA parametric study showed that as the metal interlocking features become more aligned with the pulling direction (i.e. the tilt angle decreases), the peak maximum principal stress in the polymer decreases and the polymer displacement at the interface increases. This is mainly due to the decrease in the resistance to polymer pull-up force as the features become more aligned with the pulling direction. In addition, as the aspect ratio of the metal feature decreases (i.e. thickness (T): length (L)), the stress rises in metal and declines in polymer (Figure 4-2(c) and (e)). This is because the metal becomes weaker as the feature's aspect ratio decreases and more energy is consumed in deforming it, which reduces stress in the polymer.

The experiments revealed a proportional increase in the strength with increasing the neck height and cross-sectional area of the features and decreasing spacing between features (i.e. increasing number of features) (Figure 4-3). This is related to the increased surface area of the metal features, which allows for the establishment of more Co-Cr/PMMA bonds. The interlocking feature design A2H10S09 achieved a strength of 34.4 ± 1 MPa, which was greater than the highest reported interfacial tensile strength between PMMA and a sandblasted metal bonded using chemical agents (i.e. 23 MPa) [165]. The interlocking feature design presented also a better performance when

compared with a conventional bead design in terms of strength, stiffness, and PMMA displacement at interface. This was expected because the interlocking design provides better alignment of metal features with the pulling force direction. Hence, a greater part of the strain energy is probably converted into elastic strain energy in the metal in the case of the interlocking features compared with the bead design. In addition, the interlocking design has a higher surface area (i.e. 167 mm²) compared with the bead design (i.e. 56 mm²), which allows the formation of more bonds between Co-Cr and PMMA. It is concluded that the bead design is good for reducing stress in the metal, whereas the interlocking design is better for reducing stress in the polymer (Figure 4-6). Nevertheless, the stress developed in the metal features of interlocking design was below the yield strength of laser-sintered Co-Cr, which is around 500 MPa [156]. It is also noteworthy that the presence of sharp edges in the 3D finite element model of the interlocking features contributed to increasing the computational stress value.

Both the interlocking and bead designs fractured near the Co-Cr/PMMA interface as shown by the stereo microscope images (Figure 4-5), which was consistent with the 3D FEA (Figure 4-6). This could be due to the large difference in the elastic modulus across the Co-Cr/PMMA interface [82]. Two scenarios might explain the cracking mechanism in both designs. (i) A cohesive failure in PMMA initiated a crack, which then propagated through an adhesive failure at the Co-Cr/PMMA interface. (ii) A crack started due to an adhesive failure at the Co-Cr/PMMA interface and then propagated through a cohesive failure within PMMA. The interfacial PMMA displacement at the side of the specimen was around the order of 10 μm in both designs (Figure 4-6), which suggests that the crack could have started initially as an adhesive failure at the Co-Cr/PMMA interface. This could also be supported by the fact that overcoming the adhesive strength of the Co-Cr/PMMA specimen (i.e. 2.3 MPa) is easier than overcoming the cohesive

strength of PMMA (i.e. 40.2 MPa). Nevertheless, in both designs, the crack started from the side of the specimen, which might be due to some small mis-alignment during tensile testing and material defects related to the presence of bubbles in PMMA and sample machining.

Among the limitations of this study are the presence of air bubbles in PMMA, which was not accounted for in the FEA simulations, and the assumption of linear elastic behaviour for PMMA, which is a viscoelastic material. However, these assumptions are alleviated given the comparative procedure followed among the adopted groups in this study and that viscoelastic effect is negligible at low strains (i.e. $< 0.5\%$) [181]. Another limitation is the presence of sharp edges in the geometry used for 3D FEA, which are usually rounded when produced by laser-sintering. The edges were not rounded during FEA to prevent divergence problems when dealing with surface-to-surface contact interaction between Co-Cr and PMMA finite elements. It is also noteworthy that both the thickness for 2D FEA and the area for 3D FEA and experiments were important parameters to consider. Though a preliminary optimized shape was achieved by considering thickness in the 2D FEA, it was necessary to reconsider the area parameter in the 3D studies due to the complexity of the I-shaped cross-section. Moreover, considering both thickness and area parameters was very important to the validation of the work. The 2D FEA showed that increasing thickness resulted in increasing stiffness and reducing polymer displacement at interface (Figure 4-2(f)), which is consistent with 3D FEA (Figure 4-7(h) & (i)) and with experiments that revealed an increase in the experimental tensile strength with increasing cross-sectional area (Figure 4-3(c)).

Within the limitation of this work, the percentage difference in tensile strength between Co-Cr/PMMA specimen with interlocking feature design A2H10S09 and PMMA was 16%. We expect to obtain better results upon scaling down the feature's size and increasing the density of features. However, in this study we were limited by the resolution of the laser-sintering machine, which was

about 30 μm . To minimize defects due to the manufacturing process, the smallest feature in the specimens was designed to be at least one order of magnitude greater than the resolution of the laser-sintering machine. In addition, we expect that our interlocking feature design will perform better than the conventional retention designs under shear or combined loading conditions, which will be the subject of future work. It is also important to note that the focus of this manuscript was primarily on enhancing the metal/polymer interfacial strength through mechanical retention and future studies should focus on the combination of the proposed mechanical interlocking technique with state-of-the-art chemical bonding agents to reach optimal results. A critical question to be addressed is whether the interlocking features would compromise or enhance the efficiency of the chemical bonding agent, which we hope to answer in our forthcoming studies.

4.6 Conclusion

This study proposed a new bioinspired and optimized interlocking feature design that can be additively manufactured on laser-sintered dental and biomedical prostheses to improve the strength and stiffness of metal/polymer (i.e. Co-Cr/PMMA) interfaces and reduce the polymer micromotion at the interface. We used the bio-mimetic stress-induced material transformation (SMT) optimization method which suggested a Y-shaped interlocking feature similar to the roots of mangrove trees. Then, mesh adaptive direct search (MADS) combined with finite element analysis (FEA) were conducted to determine optimal dimensions of the bioinspired interlocking features. Experiments confirmed that our optimized interlocking features increased the strength of the Co-Cr/PMMA interface from 2.3 MPa (flat interface) to 34.4 ± 1 MPa which is greater than the highest reported interfacial tensile strength between PMMA and a sandblasted metal bonded using chemical agents (i.e. 23 MPa). We demonstrated that the newly proposed interlocking retention design can serve as an effective route towards improving the mechanical properties of

metal/polymer (i.e. Co-Cr/PMMA) interfaces and thus providing better mechanical performance compared with conventional retention methods.

4.7 Supplementary Material

4.7.1 Shape Optimization using Stress-Induced Material Transformation

Stress-induced Material Transformation (SMT), also referred as soft kill option (SKO), was used to provide a preliminary bioinspired design. This method, originally proposed by Mattheck [29, 33], mimics the adaptive growth of biological structures such as bones and trees stimulated by mechanical loads. It is implemented through Finite Element Analysis (FEA) and the objective is to ensure homogenous stress distribution [16, 39]. Shape optimization is used to determine a rough but efficient layout of materials in a structure and thus provides a draft design from which the optimal shape could be obtained [16, 39]. The simulation model was carried out by integration of Abaqus (Dassault Systems, Providence, RI, USA) and MATLAB. Initially, the design space was filled by a T-shaped metal feature ($E_{Co-Cr} = 200 \text{ GPa}$) surrounded by PMMA ($E_{PMMA} = 2.4 \text{ GPa}$), and the corresponding 2D FE model under the anticipated loading conditions was analyzed to obtain the stress distribution in the structure. Then, FEA was repeated with setting the local E in the polymer equal to a function of the stress $f(\sigma)$ calculated in the previous FEA. Thus, the heavily loaded zones were strengthened and the lightly loaded zones were weakened. After that, the new inhomogeneous structure was subjected to the same loading conditions. The process was repeated until a converged state was achieved (i.e. until the material was iteratively redistributed within the design space). The resulting material layout provided a draft design from which an optimized shape could be obtained. A simple formula for $f(\sigma)$ was proposed by Mattheck [22] such that $E_{i+1} = E_i + k(\sigma_i - \sigma_{ref})$ where k controls the rate of change of the modulus and σ_{ref} is a reference stress which would be the failure stress of PMMA (i.e. 65 MPa).

To constrain the change of Young's modulus, E_{i+1} ranged between two values E_{PMMA} and E_{Co-Cr} such that:

$$E_{i+1} = E_{PMMA} \text{ if } E_{i+1} < E_{PMMA} \text{ and } E_{i+1} = E_{Co-Cr} \text{ if } E_{i+1} > E_{Co-Cr}$$

Figure 4-9 shows the results of shape optimization after 36 iterations. The shape of the retention feature in Figure 4-9 was optimized such that the stress in PMMA does not exceed 65 MPa. The MATLAB and Abaqus UMAT codes used for conducting the shape optimization procedures are provided in Appendix A. The same codes could be used with other examples of shape optimization of two different materials provided an Abaqus input file is supplied.

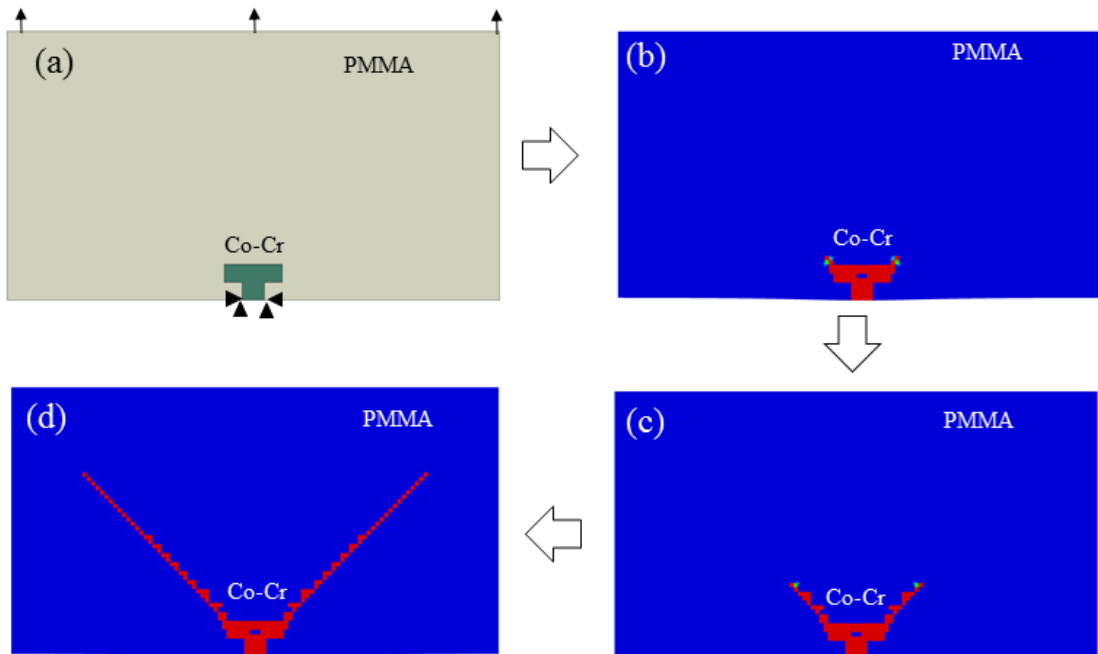


Figure 4-9: (a) Initial geometry of a retention feature with loading (10 mm/min) and boundary conditions, where green represents Co-Cr with $E_{Co-Cr} = 200 \text{ GPa}$ and white represents PMMA with $E_{PMMA} = 2.4 \text{ GPa}$. (b) Results of the shape optimization simulation model after 3 iterations, where red represents Co-Cr, blue represents PMMA, and green represents a modulus greater than E_{PMMA} and less than E_{Co-Cr} . (c) Results after 10 iterations. (d) Optimized shape after 36 iterations.

4.7.2 Mesh adaptive direct search (MADS) optimization algorithm

Optimization using MADS was conducted as described by section 2.2 in the manuscript. NOMADm v4.6 MATLAB files and functions were downloaded, including a user guide, from [28]. To use NOMADm package, users should modify only three function files to fit their specific problems. For the current manuscript, the modified function files are provided in Appendix B. An Abaqus journal file (.jnl) was coded within the first MATLAB function file. Figure 4-10 presents a performance history showing the decrease in the objective function value as the number of function evaluations increases.

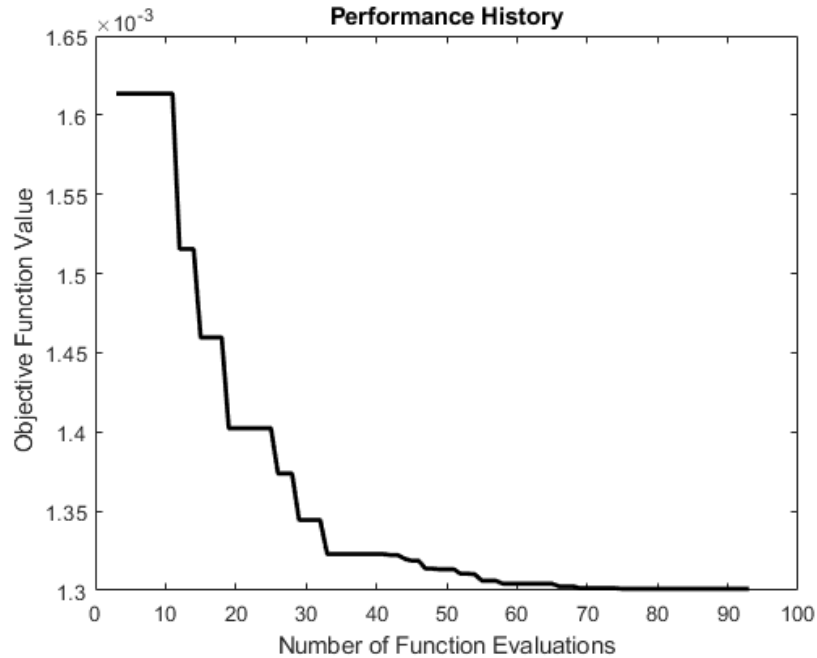


Figure 4-10: Performance History of the mesh adaptive direct search (MADS) optimization algorithm showing the objective function value (1/stiffness) versus the number of function evaluations.

4.7.3 General XPS survey spectra of control Co-Cr samples

XPS spectra was recorded using ThermoFisher Scientific K-alpha instrument equipped with a monochromatic Al K α X-ray source (1486.6 eV, $\lambda=0.834$) and an ultrahigh vacuum chamber (10^{-9} torr). Survey scans were collected with an X-ray spot size of 200 μm and energy steps of 1 eV. Peak identification was performed using the Thermo Avantage software (version 4.60). The general XPS survey spectra and surface elemental composition of control Co-Cr sample are presented in Table 4-2.

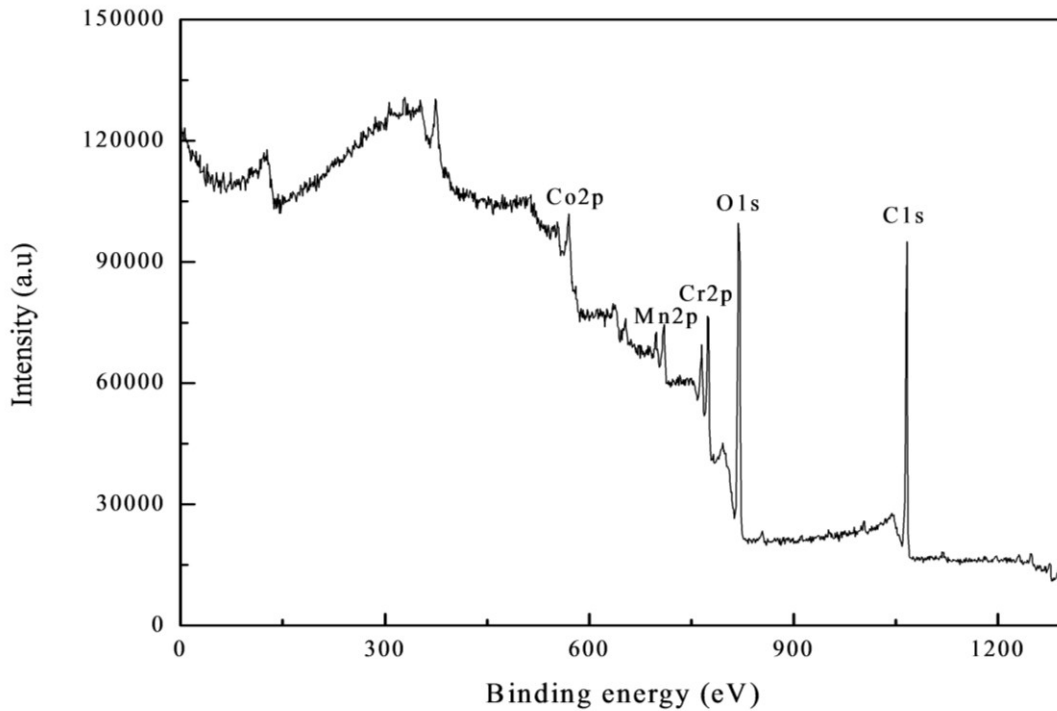


Figure 4-11: General XPS survey spectra and surface elemental composition of control Co-Cr sample.

Table 4-2: General XPS survey spectra of control Co-Cr samples

Name	Peak BE	FWHM (eV)	Area (P) CPS.eV	Atomic %
O1s	531.33	4.29	339779.6	34.13

C1s	285.32	2.79	228249.5	55.46
Cr2p	576.49	3.65	190617.1	4.86
Co2p	781.2	5.92	155236	3.09
Mn2p	641.49	4.28	96046.44	2.47

4.7.4 Tensile experiments on Co-Cr/PMMA samples

Experiments were conducted as described by section 2.5 of the manuscript. Following are few supplementary figures with a table listing experimental results.

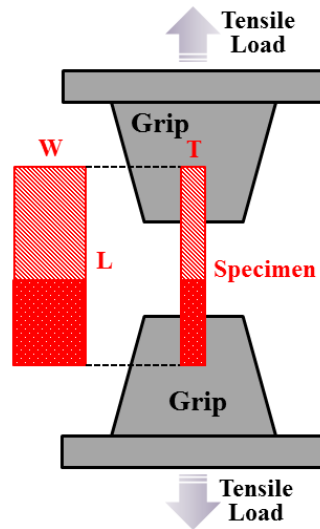
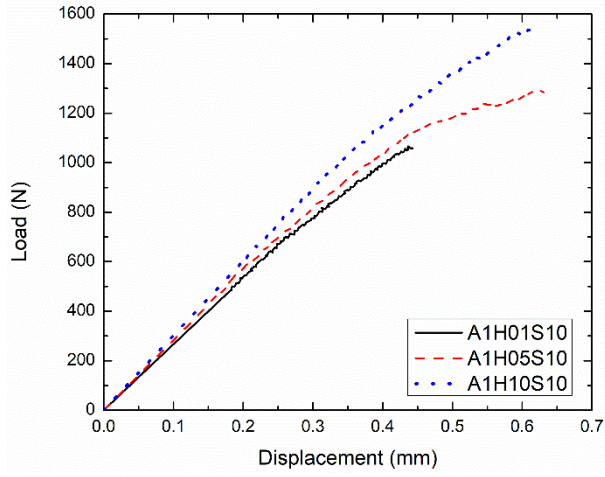
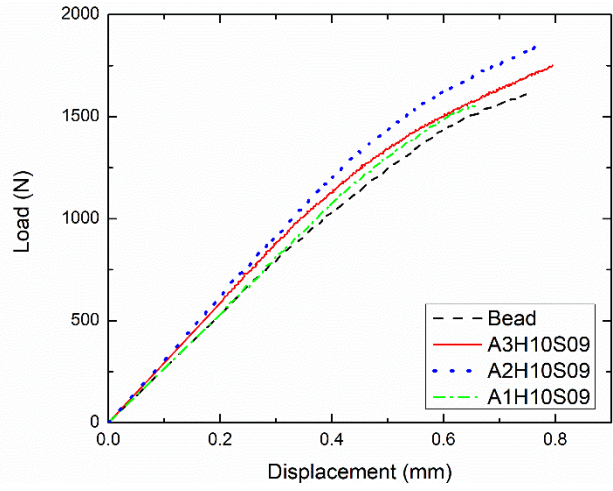


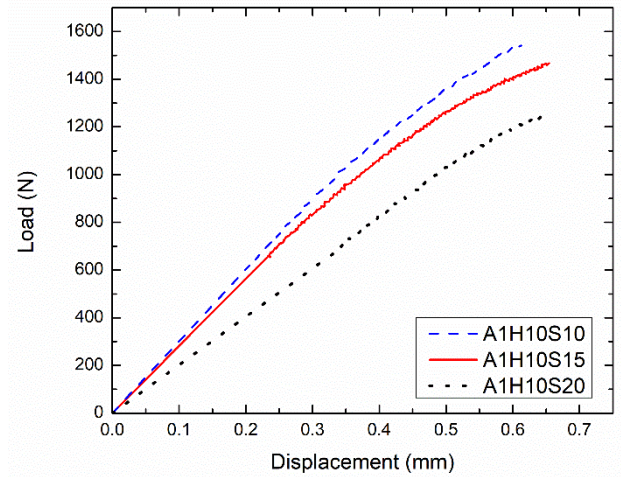
Figure 4-12: Experimental set-up of Co-Cr/PMMA sample's tensile test.



(a)



(b)



(c)

Figure 4-13: Experimental load-displacement curves of interlocking feature design groups showing the effects of (a) Height (H) at $S = 1 \text{ mm}$ and $A = 0.09 \text{ mm}^2$; (b) feature's cross-section area (A) at $S = 0.09 \text{ mm}$ and $H = 1 \text{ mm}$; and (c) spacing between features (S) at $H = 1 \text{ mm}$ and $A = 0.09 \text{ mm}^2$.

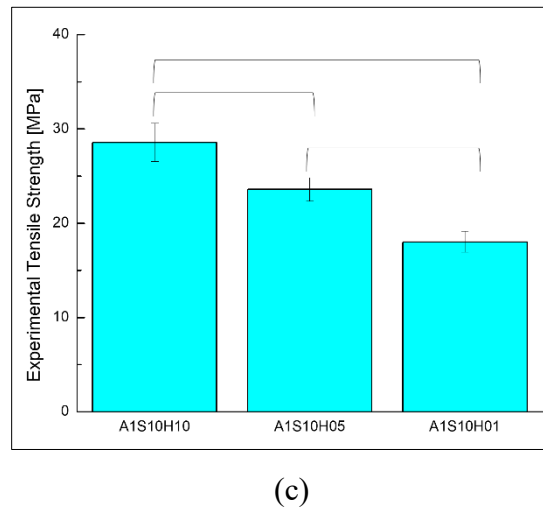
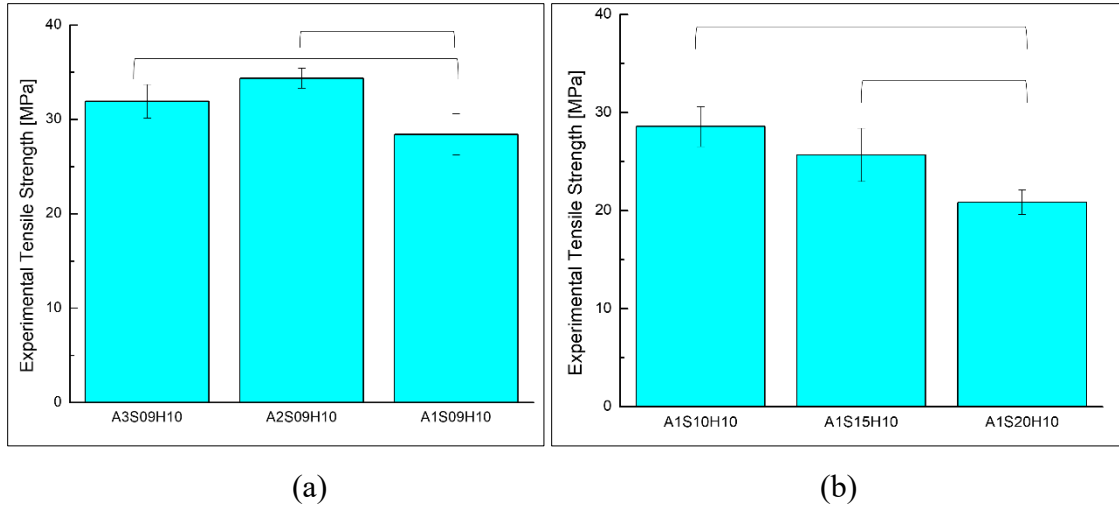


Figure 4-14: Comparison between experimental tensile strength [MPa] of interlocking feature groups showing effect of (a) feature's cross-section area; (b) spacing between features; (c) feature's neck height, with one-way analysis of variance (ANOVA) and Tukey HSD multiple comparison at significance level of $p < 0.05$.

Table 4-3: Experimental tensile strength [MPa] of design groups

Group	Average	SD	Number of samples
PMMA	40.19	1.27	6
Control	2.32	0.004	6
A1H10S09	28.41	2.20	6
A2H10S09	34.35	1.05	6
A3H10S09	31.90	1.79	6
A1H10S10	28.56	2.04	5
A1H05S10	23.58	1.23	5
A1H01S10	18.03	1.11	4
A1H01S15	25.66	2.71	3
A1H10S20	20.85	1.26	4
Bead	30.50	2.40	6

5 Topology Optimization of Lattice Structures

The previous chapter dealt with morphological shape optimization to redistribute material only where necessary in the design space. With the increasing sustainability demand for lightweight and stiff materials, the application of such algorithm to lattice structures would result in materials with high stiffness-to-weight ratio. This chapter presents a topological bioinspired design optimization framework coupled with probability distribution models to generate the initial design structure. Through this framework, space-filling and scalable bioinspired and optimized lattice structures could be designed not only for dental or biomedical prostheses, but also for various load-bearing engineering applications.

- A part of this chapter was presented on a poster on Oct 23rd, 2019 at the 13th International Conference on the Chemistry and Biology of Mineralized Tissues (ICCBMT), Montebello, Quebec, Canada. A manuscript on this chapter is under preparation to be submitted for a journal publication.
- This chapter was submitted for a journal publication.

Topological optimization of 3D lattice structures for bioinspired engineering of stiff and lightweight materials

A.A. Alsheghri^{1#}, N. Reznikov^{2#}, N. Piché², M.D. McKee^{3,4}, F. Tamimi³, J. Song^{1*}

¹Materials Engineering, McGill University, Montréal, Québec, Canada

²Object Research Systems Inc., Montréal, Québec, Canada

³Faculty of Dentistry, McGill University, Montréal, Québec, Canada

⁴Department of Anatomy and Cell Biology, McGill University, Montréal, Québec, Canada

#Equally contributing authors

*Corresponding author: Jun Song

Corresponding author complete address: Professor Jun Song, Department of Mining and Materials Engineering, McGill University, 3610 University Street, Montréal, QC, Canada, H3A 2B2

Email: jun.song2@mcgill.ca

Keywords:

Topology optimization; lattice structure; trabecular bone; additive manufacturing; bioinspired design

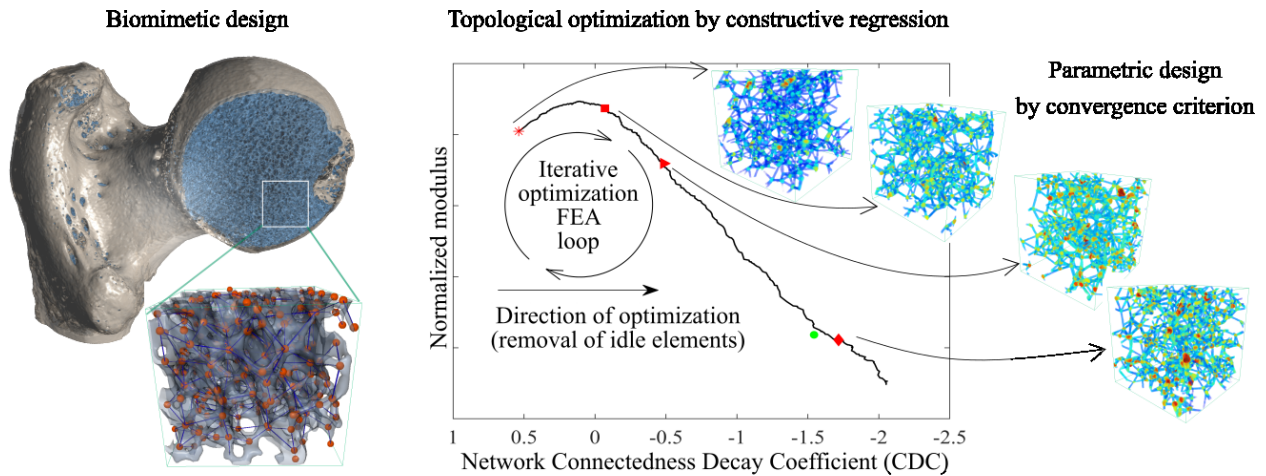
Abstract

A truly bioinspired approach to design optimization should follow Nature's paradigm of "minimum inventory with maximum diversity". One way to achieve desired properties, and to diversify the selection of attainable properties without expanding the material inventory and the fabrication toolkit, is by topological optimization. Topological optimization is concerned with the way in which the components of a whole are interrelated, regardless of their absolute size and shape. The present study was inspired by constructive regression of trabecular bone – a natural process of topological optimization occurring early in its development, involving pruning of redundant elements, and resulting in a stable structure capable of functional adaptations at the lowest metabolic cost. We have recapitulated this biological topological optimization cycle by first intentionally overdesigning in silico an excessive structure followed by simulated loading and incremental pruning of the least-loaded elements and augmentation of the over-loaded elements. Optimized structures of several generations were produced along this optimization trajectory, when pre-set convergence criteria were met. These biomimetic structures were compared to each other and to the reference structure derived from bone. Our results showed robust recapitulation of the natural optimization algorithm in uniaxial loading. However, following triaxial loading, the optimization algorithm resulted in lattice structures that were stiffer and more stretch-dominated than the reference lattice, and were therefore more capable of uniform load distribution. Finally, by 3D printing and mechanical testing, we show that although there remains a gap between the designed precision of optimized lattices and the fidelity of their manufacturing, this semi-stochastic topological optimization procedure opens new exciting possibilities for parametric design that combines flexibility, precision and resource conservation.

Statement of significance

Trabecular bone is a lightweight, load-bearing 3D structure, the architectural properties of which have been refined by millions of years of evolution. Here, we apply topological optimization principles learned from trabecular bone to biomimetic lattice design and testing. Recapitulation of the natural constructive regression of trabecular bone resulted in a generic design recipe for lattice structures; by setting different convergence criteria, diverse mechanical properties could be obtained (such as stiffness, weight reduction, and/or uniformity of stress distribution) while using the same material and fabrication method. Moreover, the built-in randomness and scale-independence of the design prototypes allow for the addition of other parameters such as anisotropy, porosity or structural gradients, for better fine-tuning of mechanical properties.

Graphical abstract



5.1 Introduction

Engineering design and structural optimization

Engineering design is a field of engineering aimed at making the best structure possible for a particular set of functional requirements in given environmental circumstances. For example, the performance of a given structure can be improved by using a different material (*e.g.*, metal versus timber), a novel manufacturing method (*e.g.*, wrought versus cast fixtures), or a new assembly approach (*e.g.*, welding versus soldering), or by a radical innovation of the design principle (*e.g.*, a suspended bridge versus an arched bridge). Most engineering design advances rely on the growth of the technological toolkit and the expansion of the materials inventory [176, 182]. Conversely, design optimization in Nature is confined to a limited inventory of materials – it is driven by finding the most energy-saving solution, and it progresses in iterative incremental improvements over the course of evolution [183]. For this reason, design principles learned from biological structures continue to amaze us with their ingenuity, and they serve as an infinite source of useful, bioinspired ideas to direct our creativity.

Topology optimization

One way to achieve better stability of a load-bearing structures without using more material and/or without resorting to a different material is to avoid nonaxial loading of the elements [184-186]. A predominance of axial deformations (tensile and compressive) renders a structure “stretch-dominated”, as opposed to “bend-dominated”, in the case where shear and bending forces are more prominent. Stretch-dominated structures – like plant parenchyma, or spider webs – are common in Nature, having triangulated structural motifs that define stability regardless of the mode of loading [187-189]. Examples of stretch-dominated engineered objects are truss structures and geodesic domes [190]. While the stiffness of a stretch-dominated structure scales linearly with its relative

density, the stiffness of a bend-dominated structure scales with the square of its relative density [64]. This means that for the same relative density and same material, a stretch-dominated structure would be five times stiffer than a bend-dominated structure [8, 64].

Topology optimization is a design strategy that is concerned with the purposeful distribution of available material in 3D to yield a desired mechanical performance. Generally, using stretch-dominated topological motifs favors a structure's resistance to loading, while using bend-dominated design is beneficial for energy-absorbing sacrificial structures [19, 64]. The desirable outcome of topology optimization can be further specified as elimination of stress concentrators, increasing rigidity, reducing weight, and so on. Earlier studies proposed various strategies for topology optimization to obtain the most cost-effective and sustainable structural design using homogenization, the "soft kill option", or evolutionary design optimization techniques [14, 16, 191]. One prominent challenge in traditional deterministic topology optimization is the rapid growth in computational cost as the size of the problem increases, sometimes causing a failure of the algorithm [18]. Bioinspired heuristic optimization usually entails iterative modifications of the original structure until a convergence of the desired and simulated properties is achieved, following a continuum trajectory [14].

Iterative topological optimization of trabecular bone in the skeleton

Trabecular bone tissue is an inspiring example of a natural, load-bearing, light-weight structure [29, 188, 192, 193]. Trabecular bone is mostly present at skeletal sites where movement occurs (for example, in articulating ends of bones at joints, in the vertebrae of the spine, and in the short bones of hands and feet) – it is therefore well optimized to withstand forces having diverse

directions and various magnitudes [194, 195]⁵. Comprised of a 3D network of tiny interconnected osseous struts, trabecular bone tissue continually undergoes cell-mediated remodeling – a dynamic biological process aimed at functional adaptation [48]. In brief, and to provide a simple description, this life-long adaptation (or structural optimization, from an engineering perspective) augments the most-loaded struts and eliminates the least-loaded struts in order to maintain the best mechanical performance at the lowest metabolic cost [41, 46]. As a result of this local, function-driven enhancement that refines and/or simplifies the 3D structure, the osseous trabeculae vary in size from being fine spicules several hundreds of micrometers thick, to larger and platy buttresses that blend with the robust compact bone. Thus, different areas of trabecular bone tissue vary in their material volume fraction from being dense to porous, and they locally acquire more-or-less anisotropic texture that reflects predominant stress trajectories [40, 46, 47]. All this variation is a “log” of bone adaptation to its loading history and biomechanical environment [45].

Besides this described morphological optimization, trabecular bone also undergoes fundamental topological optimization. As early as during fetal development, bone tissue in the growing skeleton forms in excess, and then immediately enters the process of constructive regression and refinement [196]. This is often part of normal developmental processes in organisms when some overproduced bone elements (or brain synaptic connections, for example) are pruned and eliminated over time and organismal development [46, 196, 197]. From this bone pruning process, remaining trabeculae continue morphological adaptation and optimization [196, 198]. This constructive regression and pruning of the fetal trabecular network modify its 3D structural pattern, and alters the way

⁵ Calvarial bones also contain spongy trabecular structure called diploë that is sandwiched between the outer and inner compact tables of the skull. The biomechanical role of diploë is rather that of an energy-absorbing safety structure in the case of impact; *i.e.* the functional adaptation of diploë is different from that of canonical trabecular bone exposed to constant loading as is being discussed here.

trabeculae connect with their neighbours, essentially simplifying the network. Trabecular bone is thus an example of topological optimization implemented by Nature that results in a stable fundamental blueprint that does not change much later in life (despite being remodeled/replaced over decades of life), and can accommodate local variations in size and shape of its elements [199, 200].

To recapitulate the topological principles of trabecular bone organization, the notion of a “graph” needs to be introduced, which is an abstract mathematical notion describing how the components of the whole are related to each other. In a graph of trabecular bone, every 3D osseous strut (that has a certain thickness, length and cross-sectional geometry) is represented by a unique edge (that is, a unidimensional element with two distinct sets of 3D coordinates corresponding to the origin and the terminus). In this context, a node is an abstract entity where more than two edges connect. Nodes can be classified by their coordination, or valence, according to the number of edges connecting to/emanating from it, as a 3-neighbour (3-N) node, a 4-neighbour (4-N) node, and so on. Theoretically, having only 4-N nodes with the edges maximally offset by the tetrahedral angle (109.5°) is sufficient to fill 3D volume [201]. However, the graph of mature and functional trabecular bone is more diverse than that, and its space-filling motifs include the nodes of 3, 4, 5 and (rarely) more neighbours, with their abundance decreasing as the node coordination increases. For any node coordination, the emanating edges are maximally offset from each other with the angles between the edges forming a unimodal distribution corresponding to geometrically symmetrical, idealized shapes: around 120° for a 3-N node, around 109.5° for 4-N node, and so on. Trabecular bone is thus a decentralized, nonhierarchical sparsely connected network spanning maximal 3D volume where connections of low coordination (low valence) dominate [199, 200].

This work was originally inspired by our investigation of trabecular bone’s topological properties, and it addresses the following questions: Firstly, is it possible to computationally reproduce the iterative natural process of topological refinement, following the progression from a naïve, overconnected structure to an optimized light-weight structure in which every element exists for a mechanical purpose and no material is wasted on idle elements? Secondly, can we identify the trade-off between the highest mechanical stability (stiffness) and the lowest architectural complexity and mass, and whether that combination would be reminiscent of our natural reference structure – trabecular bone? Thirdly, to address the engineering utility of this endeavor, can we manufacture such topologically optimized prototype structures using 3D printing methods?

Glossary	
Morphology	The study of the form of things (<i>e.g.</i> , size or shape).
Topology	The study of geometrical properties and spatial relations unaffected by the continuous change of shape or size of figures; the way in which constituent parts are interrelated or arranged.
Graph	An abstract mathematical construct that represents pairwise relations between objects. A graph in this context is composed of nodes, or vertices, which are connected by edges.
Node	A fundamental unit of which graphs are formed. In this context, it is a junction of three and more edges. A node possesses a unique set of three coordinates in Cartesian space. For a set of nodes, the nodes connected by edges are neighbours.
Edge	A unidimensional line that connects two nodes (<i>i.e.</i> neighbour nodes in this context).
Blueprint	A design plan, or something which acts as a plan, model or template. Topological blueprint is equivalent to graph in this context.
Lattice	An embodied graph in which the edges have an assigned cross-sectional value: thus, a lattice is a real object in the 3D domain, while its graph is abstract.
Coordination (valence)	A property of a node in a graph that describes the number of connected neighbours, akin to the coordination number of an atom in a chemical compound. For example, a node connected to four immediate neighbours has coordination 4 and is designated as 4-N.
CDC, Connectedness Decay Coefficient	A single metric that incorporates the proportions of the nodes of different coordination in a sparsely connected graph. In many natural structures, the higher the node coordination, the

	lower the node abundance. A plot of node abundance by node coordination thus follows an exponential decay.
FEA, Finite-Element Analysis	A numerical solution that approximates the response of a material to external loading. In FEA, the material domain is divided into finite regions, and the differential equation is represented by a combination of approximation functions.
Element	A part of a lattice – an embodied edge. Here, the edge is the centroid of the element.
Stiffness	The resistance of a structure or material to deformation in response to an applied force.
Compliance	The inverse of stiffness, flexibility and the ease of deformation in response to an applied force.
Axial loading	Application of force along an object’s axis. Tension and compression are axial loads.
Nonaxial loading	Application of force off the object’s axis. Bending and torsion are nonaxial combined loads that incorporate tension, compression and shear.
Uniaxial test	A mechanical test in which the applied external force acts in one direction only.
Triaxial test	A mechanical test that applies forces on three orthogonal directions of the specimen.
Convergence	Arriving at a solution that is close to the pre-specified desired criteria.
Idle element	A nonload-bearing element; an element subjected to negligible stress.
Reference lattice	A lattice that corresponds to the highly-conserved topological blueprint of trabecular bone.
Naïve biomimetic lattice	A biomimetic lattice prior to entering the iterative optimization loop. Here, the graph nodes of the naïve lattice are intentionally overconnected, and most elements are meant to be pruned.
Optimized biomimetic lattice; Generations 1, 2 and 3	A biomimetic lattice derived from the naïve lattice by removing idle elements under iterative simulated loading. Here, the three generations of the optimized biomimetic lattices correspond to different convergence criteria: Generation 1 – maximal stress uniformity; Generation 2 – weight equal to Reference lattice; Generation 3 – number of elements equal to Reference lattice.

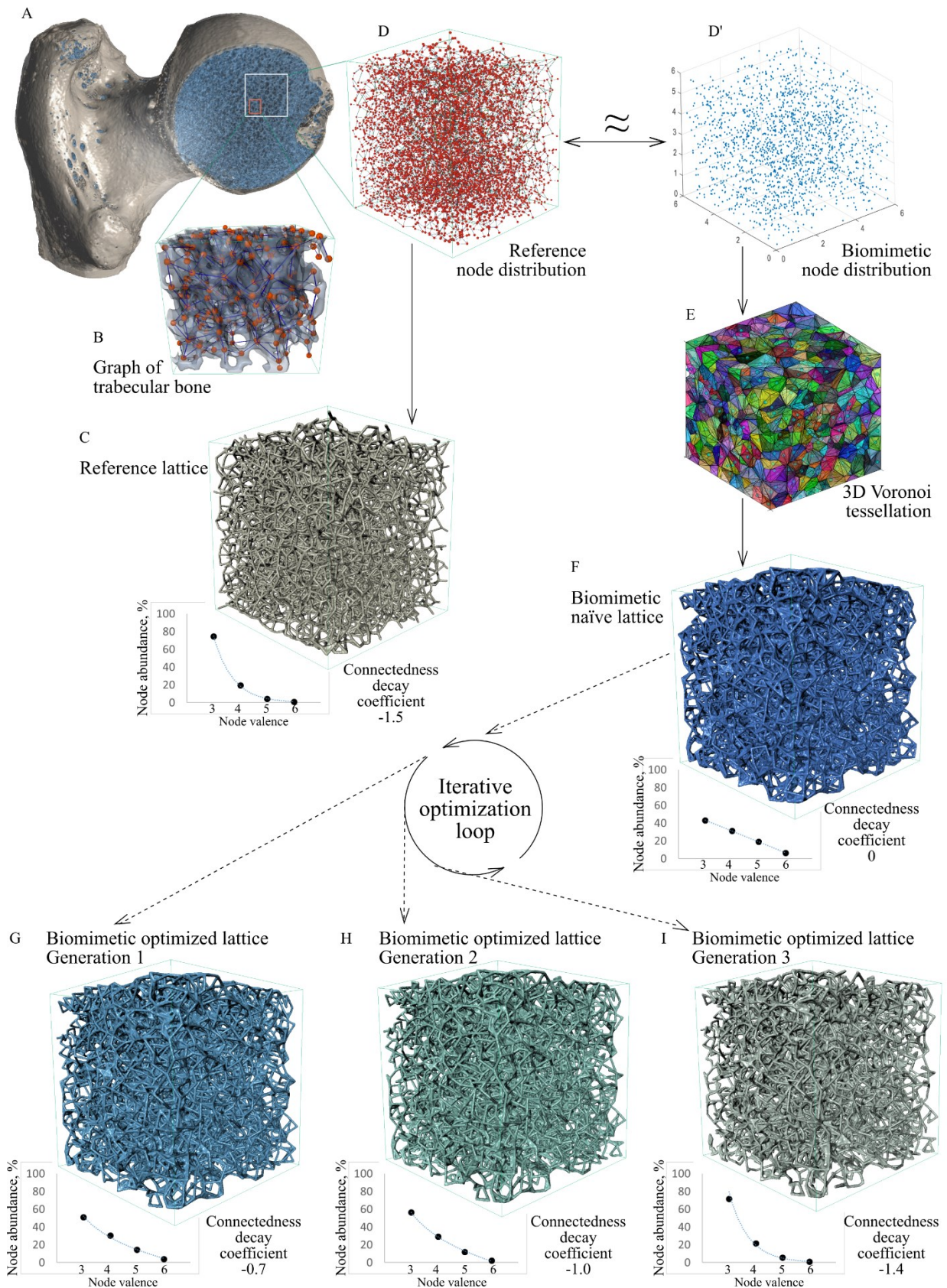


Figure 5-1: Bioinspired design and topological optimization – a general principle. (A) μ CT reconstruction of a human proximal femur. (B) Graph of trabecular bone (highlighted in blue in A) and (C) reference lattice. (D) Cloud of nodes from a graph of trabecular bone is reproduced using a probability distribution function, D' . The nodes are connected using a 3D Voronoi tessellation (E) to form a biomimetic lattice (F). The biomimetic lattice enters the optimization loop and generates three optimized lattices (G-I). All lattices are topologically analyzed in terms of the node connectedness decay coefficient, CDC (insets in C, and F-I).

5.2 Methodology

5.2.1 General principle of iterative topological optimization and validation

We started this study by analyzing the graphs of human trabecular bone samples from the proximal femur. Since all nonpathological trabecular bone samples share essentially the same topological parameters (node coordination, node type abundance, edge angular offset) [45, 46, 199, 200], any arbitrary chosen graph derived from natural trabecular bone can be used as reference graphs (in its mathematical abstract sense) or as the reference lattice (when a certain thickness value is assigned to the edges, such as in FEA or in additive manufacturing). For our optimization purpose, the graph consists of the set of nodes that is fixed, and the set of edges that are mutable. For the bioinspired design, the set of nodes of the reference graph has been closely reproduced by fitting a probability distribution function. This bioinspired set of nodes had the same randomness, and the same likelihood of finding a neighbour within a certain radius, as the set of nodes in the reference graph. Each node in the set was connected by edges to its 5 nearest neighbours using an interim step of 3D Voronoi tessellation. In the naïve biomimetic design (prior to optimization), the number of edges was intentionally higher in comparison to the reference graph. This overconnected naïve lattice was iteratively optimized via elimination of idle edges and augmentation of the nodes connected to the most stressed elements in a simulated FEA experiment in which edges were replaced with finite elements. The net effect was the decrease of the total number of edges because more edges were eliminated than added. During the iterative optimization cycle with simultaneous FEA monitoring of mechanical properties, a series of

convergence conditions was pre-defined. For every convergence condition, an optimized lattice was registered and saved. These optimized lattices were the following: Generation 1 – achievement of the most uniform stresses in the lattice, Generation 2 – the net mass of the biomimetic lattice equals the net mass of the reference lattice, and Generation 3 – the number of edges in the optimized lattice equals the number of edges of the reference lattice. The iterative optimization cycle was conducted using uniaxial and triaxial simulated loading. The uniaxial loading optimization was conducted on the lattices that corresponded to the reference lattice scale and on their scaled-up counterparts, to rule out the effect of scale/size on topological optimization. The triaxial loading optimization cycle was conducted for two independently generated biomimetic sets of nodes, to validate the reproducibility of the bioinspired optimization loop. For the five lattices – one reference lattice, and four biomimetic, of which one naïve and three optimized lattices – mesh files were produced for additive manufacturing. The lattices were 3D printed at two different scales, and their predicted (uniaxial, *in silico*) mechanical behavior was compared with their actual mechanical behavior in a displacement-controlled compression test. The mechanical parameters used for comparison were the following: effective modulus normalized by weight (uniaxial simulated test), bulk modulus normalized by weight (triaxial simulated test), maximal von Mises stress normalized by effective/bulk modulus, maximal von Mises stress variation (as its standard deviation), proportion of elements in which axial force exceeds non-axial force (FEA), and stiffness (predicted and experimentally measured). These principles of design, optimization and comparison are graphically summarized in Figure 1, and the details are given in Supplementary Materials section.

5.2.2 *CDC – a topological metric used for comparison of the reference lattice and biomimetic lattices at different stages of optimization*

To compare the topological parameters amongst the lattices using a simple metric, the abundance of nodes of different coordination was determined. The abundance of nodes of a particular type is expressed in % from the total number of nodes. For the reference graph, the node abundance was exponentially decreasing with an increase in node coordination. The naïve graphs were generated with a higher default node coordination, and following topological optimization the coordination of most nodes decreased. The single metric that stands for the proportions of the nodes of different coordination is the Connectedness Decay Coefficient (CDC). In the reference graph, the abundance of three-neighbour (3-N) nodes is the highest, followed by nodes of four (4-N), five (5-N), and six (6-N) neighbours, respectively, following an exponential decay in the form of: abundance of node type = $A \exp^{CDC * \text{node type}}$, where *CDC* is a negative connectedness decay coefficient in this case and *A* is a constant. Of note, the CDC is highly conserved amongst the graphs of normal human trabecular bone samples, regardless of their absolute density or porosity and is about -1.5.

5.3 Results

5.3.1 *Numerical reproducibility of the natural iterative topological refinement: Trade-off between mechanical stability (modulus) and architectural complexity*

The process of iterative optimization (simulated uniaxial loading) of a biomimetic lattice is accompanied by a nonlinear drop in the number of elements (as the idle elements are iteratively removed, and the removal rate exceeds the rate of node augmentation), and the decrease of the CDC from positive to negative as most nodes lose one or more of their elements (Figure 2A). The biomimetic naïve lattice design had a CDC slightly above zero, this indicating that high-coordination nodes were common within the structure along with low-coordination nodes. As both

the absolute number of elements and the CDC decreased, the topological blueprint of the evolving biomimetic lattice approximates that of the reference lattice and even became more simplified. Of note, the size- and scale-independent CDC parameter of several reference lattices varied slightly between -1.5 and -1.7, while their absolute number of elements per unit of volume varied more than two-fold (Figure 5-2A). As the optimization progressed, the normalized apparent modulus initially increased nonlinearly, this indicating that it is possible to achieve the beneficial combination of high load-bearing capacity at the lower weight around the Generation 1 lattice that also had the most uniform stress distribution, as per the first convergence condition (Figure 2B). Then, the normalized apparent modulus begins a nearly linear descent towards the values of the reference lattice (Figure 5-2B).

The maximal von Mises stress value in the lattices represents the presence of stress concentrators. Obviously, the structure performs at its best when the loads are distributed uniformly with no stress concentrations. This condition is unattainable in real life. Since the elements comprising the lattices were modeled as Timoshenko beams, each element has a range of von Mises stress values. The maximal values in each element's range were compared among all the elements in the lattice – maximal von Mises confirms the presence of the stress concentrator, and the standard deviation of the maximal von Mises value indicates how potentially detrimental that stress concentrator is at the scale of the entire structure. In the process of iterative optimization, the increase of von Mises stress was very gradual and shallow, from the naïve lattice throughout to the Generation 3 optimized lattice. However, we noticed the following phenomena: Firstly, von Mises stress of the reference lattice was higher than von Mises stress in all biomimetic naïve and optimized lattices, indicating that naturally optimized structure can forgive nonaxial stress components to a certain extent. Secondly, as the optimization proceeded for several cycles beyond

the Generation 3 lattice, there was a steep increase in von Mises stress values, probably indicating a transition from a stretch-dominated structure to a bend-dominated structure (Figure 5-2C). This last result shows that the output of naturally occurring iterative pruning (reference lattice) keeps the structure in the low range of von Mises stress values and does not allow nonaxial deformations to dominate the structure. Only excessive artificial pruning (with CDC approximating -2) brings about a sharp increase of von Mises stresses that would probably undermine the structural stability of that lattice.

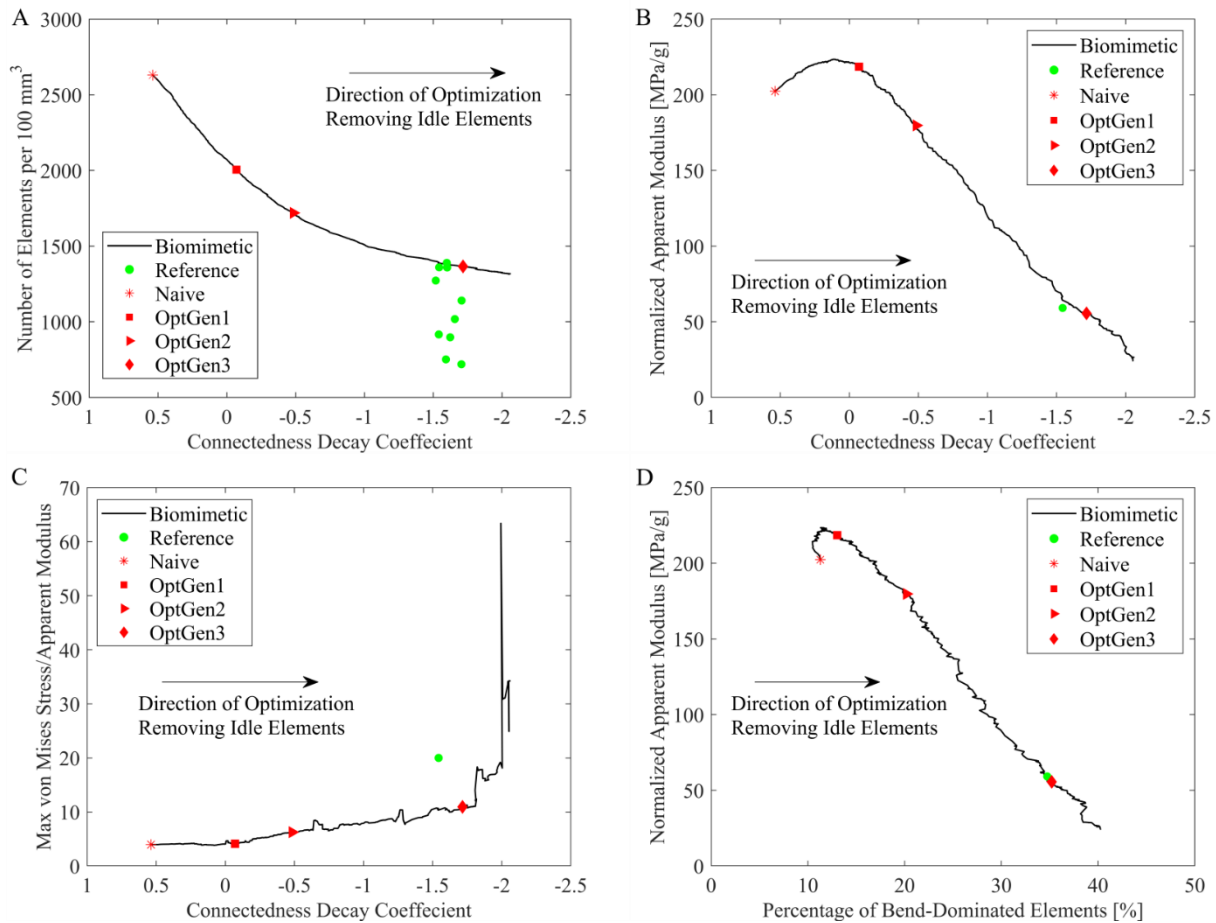


Figure 5-2: Topological design iterative optimization; uniaxial compression. (A) While all mature trabecular bone lattices have remarkably similar CDC, the bioinspired naïve lattice starts with the higher CDC and approximates the reference CDC values in the process of iterative pruning. (B) The normalized elastic modulus first increases in a nonlinear fashion reaching the maximum in the optimized lattice Generation 1. Further iterations of element pruning result in a nearly linear

decrease of the normalized modulus to the value of the reference lattice and lower. (C) Maximal von Mises stress values slowly increase in the process of iterative optimization, but the dramatic increase of the von Mises criterion occurs only when CDC drops beyond the reference lattice value and the optimized Generation 3 value. (D) Dependence between the normalized apparent modulus and the proportion of bend-dominated elements.

To summarize this part of the results, iterative numerical optimization does indeed recapitulate the naturally occurring constructive regression. However, the endpoint of the natural optimization is not the combination of the highest stiffness at the given mass; instead, the endpoint of natural optimization is the lowest stiffness and lowest mass attainable while yet avoiding the predominance of nonaxial stresses and therefore ensuring stress uniformity.

5.3.2 Independence of topological optimization on the directionality of loading, the exact coordinates of the nodes, and on the size of the lattice

To illustrate the flexibility of the proposed algorithm with regard to the nature of external loading, Figure 5-3 presents the results obtained from the iterative optimization procedure using triaxial compressive loading instead of uniaxial loading, for the lattices of cubic shape $5 \times 5 \times 5$ mm. The results show that the optimization curves follow a similar trend as in the case of uniaxial simulated compressive loading (Figure 5-2). Namely, as the number of elements per unit of volume and CDC decrease, the normalized bulk modulus first increases nonlinearly, and then descends towards the values of the reference lattice (Figure 5-3A,B). Interestingly, following this triaxial optimization protocol, the optimized lattices demonstrate better uniformity of stress distribution, as seen from the lower normalized von Mises stress values (Figure 5-3C). This mainly indicates that stresses are distributed more uniformly with the larger axial (stretch-dominated) component in the biomimetic lattices (Figure 5-3D). Note that the total number of elements in the lattice used for triaxial optimization is lower than that used for uniaxial optimization. This is because the naïve graph was modeled to mimic a different reference graph.

We repeated the iterative optimization procedure using different initial node distributions (although of the same density and randomness) while monitoring the same output parameters. We observed a nearly identical trajectory of optimization (Figure 5 4). Interestingly, when the number of elements of the evolving biomimetic lattice reached the same number of elements as in the reference lattice (Generation 3), the percentage of bend-dominated elements was consistently lower in the biomimetic lattices than in the reference lattice (Figure 5 5B).

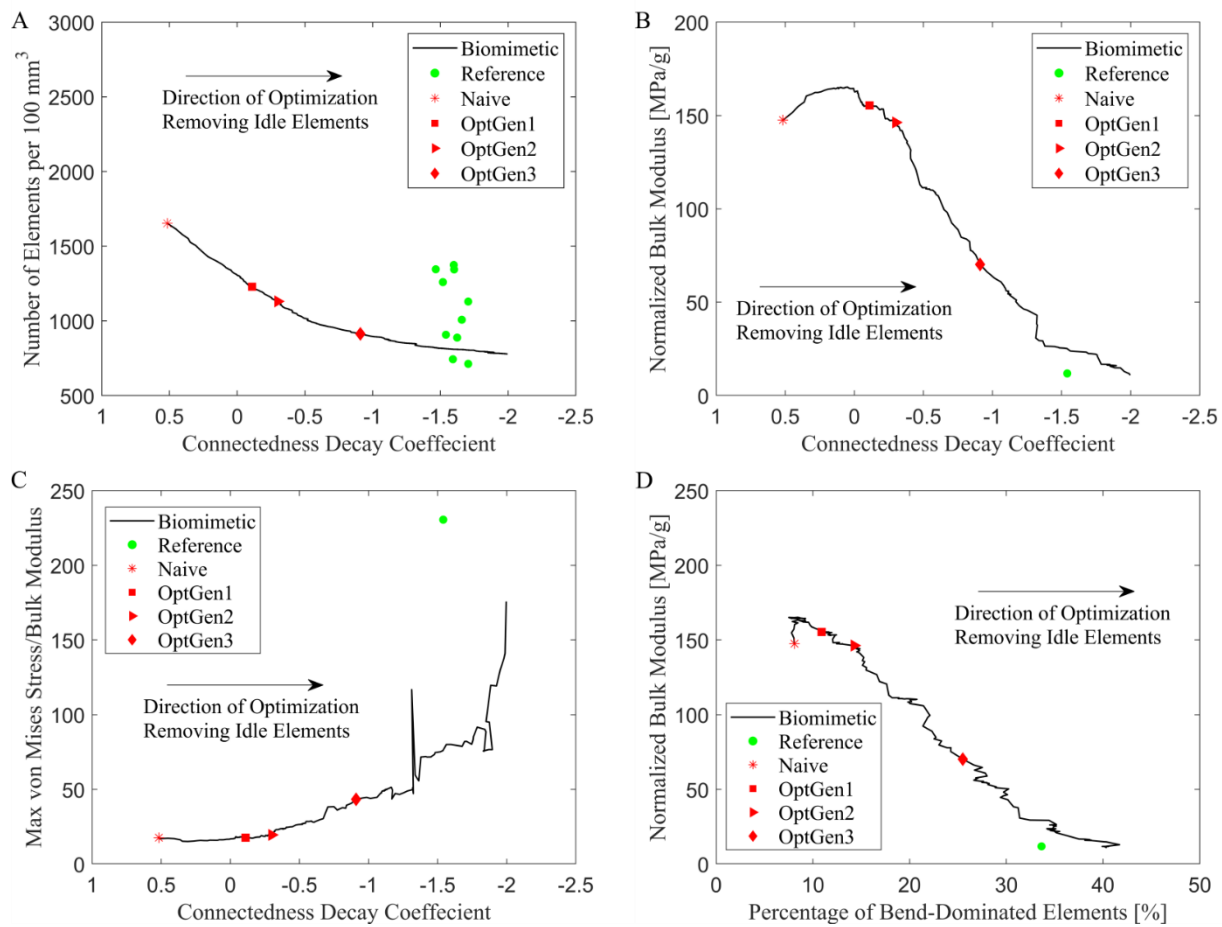


Figure 5-3: Topological design iterative optimization: triaxial compression. (A) The number of elements decreases with the optimization iterations. (B) Normalized bulk modulus follows a similar trajectory as the normalized elastic modulus in uniaxial compression (see Fig. 2B). (C) Increase in maximal von Mises stress with optimization, and (D) increase in proportion of bend-dominated elements (both panels C and D indicate that the optimized lattices have more homogeneous distribution of stresses).

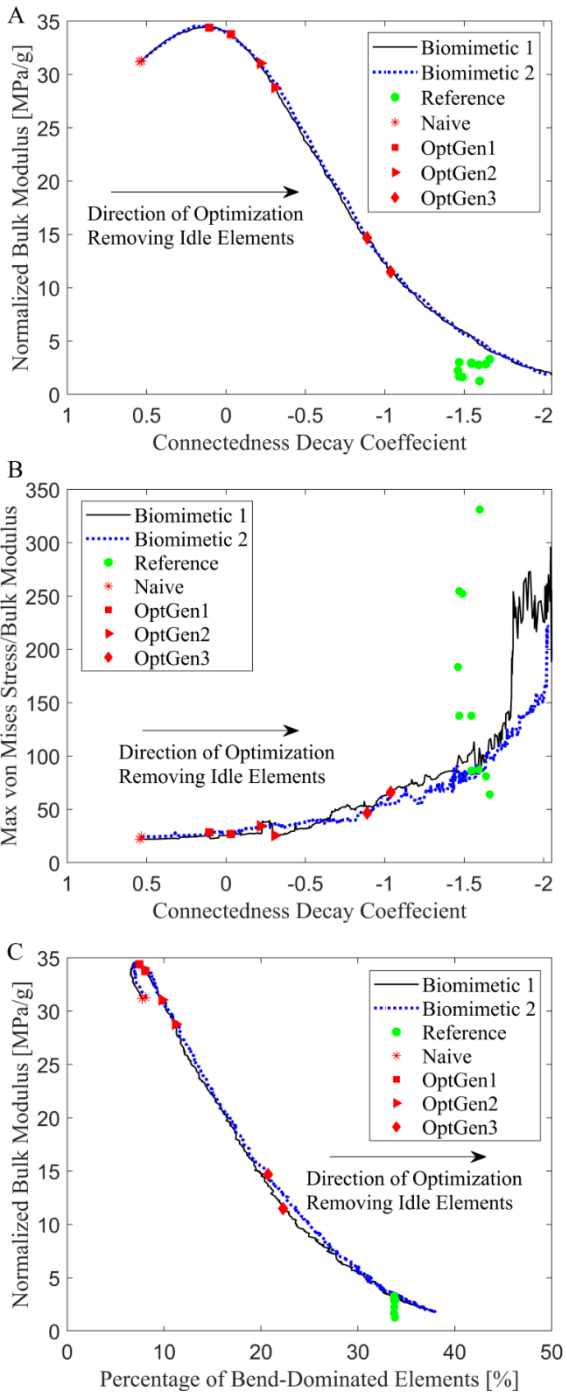


Figure 5-4: Repeated iterative optimization using different populations of nodes of the same overall volume (generated using the same probability distribution function). (A) Normalized bulk modulus versus CDC. (B) Normalized maximal von Mises stress versus CDC. (C) Normalized bulk modulus versus the proportion of bend-dominated elements.

Finally, we monitored the optimization trajectory for the biomimetic lattices of the original size ($5 \times 5 \times 5$ mm) and of the larger size ($10 \times 10 \times 10$ mm). The size difference was obtained by generating a larger 3D population of nodes. For the scaled-up lattice, the mean density of nodes per unit of volume was preserved, meaning that the number of nodes in all lattices and the number of edges in the naïve lattice was 8 times higher than in the original size lattice. Figure 5-5 illustrates essentially the same trajectories for the monitored parameters, which agrees with the concept of topological optimization: topological properties are independent of the size (and scale) of the structure in question.

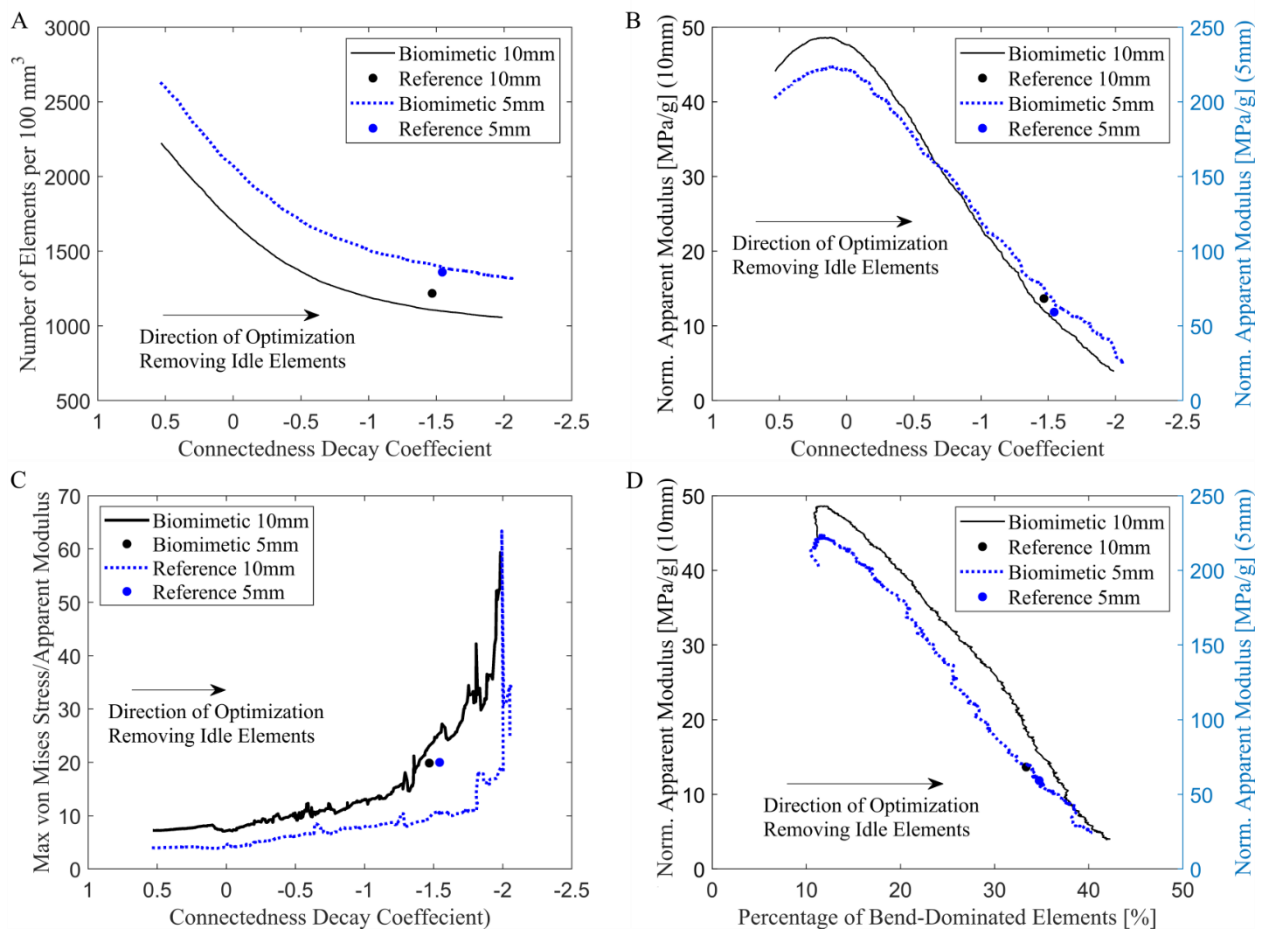


Figure 5-5: Comparison of the optimization trajectories (uniaxial optimization) of biomimetic lattices designed at 2 different 3D sizes, using the different populations of nodes of the same mean density but different volumes. Note the same shape of the optimization trajectories.

5.3.3 Feasibility of additive manufacturing of topologically optimized lattices and the effect of manufacturing method and scale on the preservation of the observed numerical trends

Additive manufacturing of reference and biomimetic lattices at the original scale (that of trabecular bone with the mean element length being in the range 0.8-1.0 mm) was assessed by superimposition of the 3D image of the surface mesh (Figure 5-6A) and the micro-computed tomography (μ CT) reconstructed 3D image (Figure 5-6B). This comparison revealed an excessive fusion of juxtaposed elements of the printed lattice (Figure 5-6B). Therefore, the original samples

were scaled by a factor of 4 to enhance their manufacturing feasibility and to evaluate the influence of the 3D printing inaccuracies and defects.

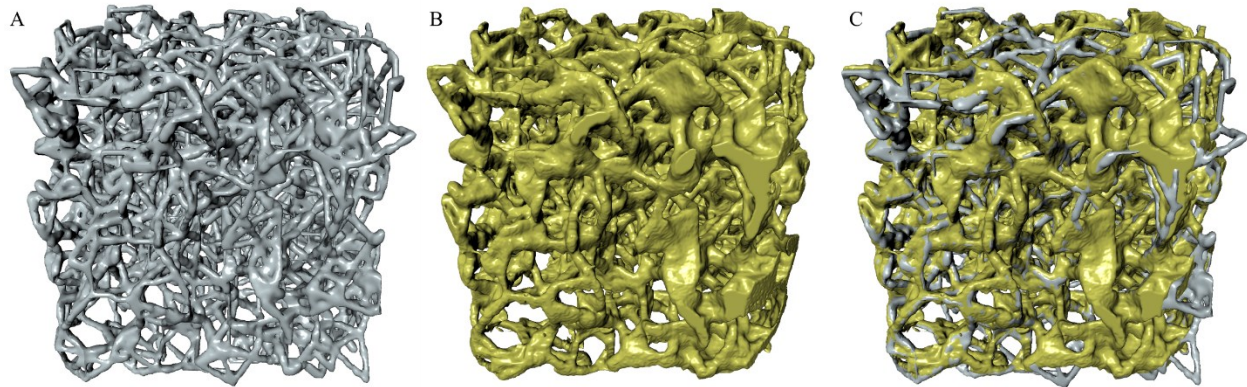


Figure 5-6: Biomimetic lattice 3D rendering. (A) Surface mesh file used for 3D printing. (B) Micro-CT reconstruction of the 3D printed lattice. (C) Superimposition of the designed and manufactured lattices.

For the prototypes manufactured at the original scale ($5 \times 5 \times 5$ mm) and $\times 4$ scale ($20 \times 20 \times 20$ mm), experimental stiffness and mass were compared with predicted thickness and mass. At the smaller manufacturing scale, the biomimetic lattices were slightly heavier than predicted which could be explained by fusion of some adjacent elements. The stiffness values of smaller (original scale) lattices were in accord with their predicted values. At the larger manufacturing scale, the reference and optimized Generation 3 lattices had their mass similar to the predicted values. Other lattices (naïve, Generation 1 and Generation 2) were lighter than predicted. All scaled-up lattices were stiffer than predicted.

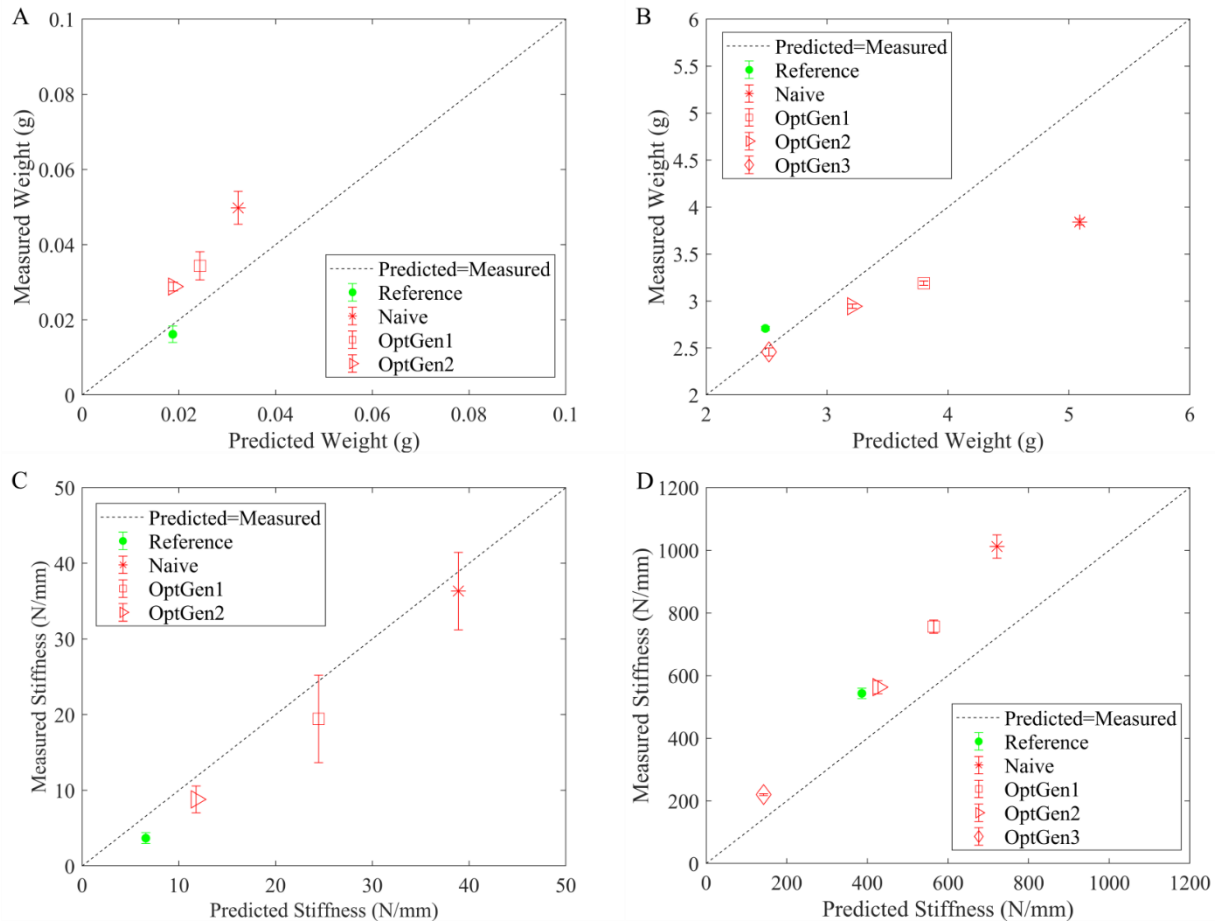


Figure 5-7: Comparison of experimentally measured and numerically predicted properties of the lattices printed at two different scales, 5 mm and 20 mm. (A) Measured and predicted mass for 5 mm lattice. (B) Measured and predicted mass for 20 mm lattice. (C) Measured and predicted stiffness for 5 mm lattice (linear fit revealed $stiffness_{measured} = stiffness_{predicted} - 3.3 N/mm$, with R-squared value of 0.99). (D) Measured and predicted stiffness for 20 mm lattice. Note the broader error bars for measured stiffness of 5 mm lattices (C) in comparison with the stiffness values of the 20 mm lattices (D).

The tables below present the results of the uniaxial compression experiments for three groups of lattices: 5 mm size uniaxially optimized (Table 5-1), 20 mm size uniaxially optimized (Table 5-2), and 20 mm size triaxially optimized (Table 5-3). To summarize this part of the results, although the outcome of mechanical testing generally converges with the trend of numerically predicted mechanical properties for each stage of optimization, a smaller scale of manufacturing renders prototypes more sensitive to fabrication defects.

Table 5-1: Experimental results for uniaxial compression testing of reference and biomimetic lattices derived from uniaxial optimization.

Uniaxial optimization original scale	Reference (n=5)	Naïve (n=5)	OptGen1 (n=5)	OptGen2 (n=5)
Weight [g]	0.016 ±0.002	0.050 ±0.004	0.034 [^] ±0.004	0.029 [^] ±0.001
Stiffness [N/mm]	3.680* ±0.707	36.326 ±5.117	19.449 ±5.781	8.809* ±1.778
Normalized stiffness [N/(mm.g)]	231.875* ±62.190	732.635 [#] ±110.651	561.093 [#] ±122.850	304.336* ±54.504

*, ^, # indicate **no** significant difference by one-way analysis of variance (ANOVA) and multiple comparison with Bonferroni correction at significance level of $p < 0.05$

Table 5-2: Experimental results for uniaxial compression testing of scaled reference and biomimetic lattices derived from uniaxial optimization

Uniaxial optimization ×4 scale	Reference (n=4)	Naïve (n=4)	OptGen1 (n=4)	OptGen2 (n=4)	OptGen3 (n=4)
Weight [g]	2.709 ±0.0217	3.841 ±0.0321	3.190 ±0.023	2.945 ±0.023	2.459 ±0.041
Stiffness [N/mm]	543.275* ±16.588	1012.116 ±37.387	756.311 ±21.194	563.066* ±20.918	220.153 ±3.126
Normalized stiffness [N/(mm.g)]	200.560* ±6.399	263.480 ±9.231	237.087 ±6.451	191.239* ±7.444	89.552 ±1.850

* indicate **no** significant difference by one-way analysis of variance (ANOVA) and multiple comparison with Bonferroni correction at significance level of $p < 0.05$

Table 5-3: Experimental results for uniaxial compression testing of scaled reference and biomimetic lattices derived from triaxial optimization.

Triaxial optimization ×4 scale	Reference (n=5)	Naïve (n=6)	OptGen1 (n=7)	OptGen2 (n=7)	OptGen3 (n=7)
Weight [g]	1.484 ^ñ ±0.079	2.023 ±0.047	1.719 [^] ±0.073	1.666 [^] ±0.064	1.505 ^ñ ±0.065
Stiffness [N/mm]	177.712 ^{*#} ±17.416	447.856 ±32.599	221.785 ^{#^} ±28.330	212.426 ^{*^} ±16.378	112.891 ±9.573
Normalized stiffness [N/(mm.g)]	119.781 ^{*#} ±11.220	221.511 ±17.008	129.687 ^{#^} ±20.803	127.552 ^{*^} ±9.125	75.148 ±7.301

^ñ, ^{*}, [#], [^] indicate **no** significant difference by one-way analysis of variance (ANOVA) and multiple comparison with Bonferroni correction at significance level of $p < 0.05$

5.4 Discussion

The purpose of this study was threefold. Firstly, we aimed to understand and recapitulate the principle of naturally occurring topological optimization. We applied the constructive regression principle in order to simplify a naïve overconnected structure, in evolutionary increments, towards an optimized structure in which no idle elements are retained. This principle of constructive regression is naturally observed in bone developmental biology and apparently it has a purpose of achieving sufficient biomechanical performance while minimizing mass and the metabolic cost of maintenance. Placing structural material where it is needed, and eliminating it where it is idle, is both economical and sustainable, and it aims at resolving the problem of overdesign – the default method of structural engineering. This objective of the study has been achieved.

Secondly, we analyzed the optimization trajectories of biomimetic lattices and compared them with the reference lattice. Since the reference lattice represents the endpoint of the biologically occurring topological optimization, the analysis of the optimization trajectories gave

us an insight into the *raison d'être* of the topological blueprint of trabecular bone. We expected from the reference lattice to illustrate the highest stiffness attainable at the lowest mass, but in fact the reference lattice had the lowest mass attainable within the low range of von Mises stress, as shown in Figure 5-2. This implies that the biomechanical rationale behind the 3D organization of the reference lattice (*e.g.* 3D layout of trabecular bone) is the uniformity of stresses and minimization of stress concentrations. This is in accord with the notion that trabecular bone is naturally adapted for fail-safe shock attenuation, rather than for withstanding maximal stress with minimal deformation. When we compared the biomimetic lattices and the reference lattice behavior in triaxial loading, the optimized biomimetic lattices serendipitously outperformed the reference lattice, both in terms of the bulk modulus and in terms of the stress uniformity. The question then remains as to whether this is attributable to the biomimetic triaxial optimization strategy being more effective than the uniaxial optimization strategy. As another possibility, perhaps this is attributable to the fact that the reference lattice (*e.g.* 3D layout of trabecular bone) is better adapted to unidirectional loading than it is adapted to triaxial loading. If the latter option is true, this means that bone is not perfectly optimized, but is merely “good enough” (functionally sufficient and energetically inexpensive) for its function in a joint. Alternatively, it may mean that the best adaptation of bone to multidirectional loading is achieved by a combination of topological and morphological adaptation, whereas the topological adaptation is the main adaptational mechanism for unidirectional loading aligned with the force of gravity.

For the biomimetic lattices, it was intriguing to see that uniaxial optimization and triaxial optimization resulted in similar trajectories for the evolution of mechanical properties. However, in the course of triaxial optimization the convergence conditions of mass equal to reference (Generation 2) and the number of elements equal to reference (Generation 3) were met earlier. As

a result, the uniaxially optimized Generation 3 lattice had the CDC value of -1.6, while the triaxially optimized Generation 3 lattice had the CDC value of around -0.8. This effectively means that triaxial optimization is more topology-preserving, less radical, and produces a structure that is more “safely” positioned within the range of stretch-dominated deformations. This particular observation can be of utility for the future design optimization approaches.

Thirdly, we tested the possibility for additive manufacturing of topologically optimized structures targeting different design endpoints. We have envisioned this topological optimization algorithm as a generic way to produce lattices with various desired properties. For example, while our convergence conditions included the highest stress uniformity, pre-defined mass and pre-defined number of elements, the other designed properties could be, for example, the highest normalized apparent (or bulk) modulus, or the maximal contribution of nonaxial loading (for sacrificial impact-damping structures). The biomimetic design method is also suitable for producing lattices with different porosities because the diameter of the elements can be deliberately matched for a specific function – the same optimized graph can be used to make a lattice of thick or thin elements, or of elements with an anisotropic cross-section, or to incorporate a gradient of element sizes or structural anisotropy. All these inputs can be fitted by the designer for any purpose, while for pre-set limitations of the manufacturing substrate, structure scale and weight, element size or shape, the overall mechanical performance would be the best possible. Such parametric tuning of the optimization trajectory, and a purposeful selection of the convergence conditions, can be very practical: for example, while having just one additive manufacturing method that uses only one substrate, an operator would still be able to diversify the properties of fabricated parts. This built-in design flexibility is in tune with Nature’s design strategy in which a minimal material inventory still results in maximal diversity. However, and importantly, this

experimental part of the study illustrated the presence of a gap between the theoretically designed properties and the feasibility of their embodiment. The quality of physical materialization of the intended design depends on the method of production and the scale/resolution of fabrication. In general, miniature lattices would be more sensitive to defects from printing, and conversely, the larger the scale of the structure with respect to a printer's resolution, the more robust and reproducible can be an expected result.

A useful property of topological design is that the embodiment of the graph edges as lattice elements remains at the operator's discretion. For example, a gradient of the elements' thickness can be assigned in a desired orientation. So far, it has been a challenge to design lattice structures for additive manufacturing such that anisotropic mechanical properties would be achieved, similar to human trabecular bone, for example [3]. Computer-aided design (CAD), image-based design, and implicit surfaces have been widely used to construct functional graded scaffolds [3, 202, 203]. Such scaffolds are commonly constructed of periodically repeating unit cells [3, 202, 203]. While the aforementioned methods enable scaffolds to obtain a desirable stiffness or porosity, they demand a vast number of attempts to achieve anticipated properties [3]. Often the resulting design is far from being optimal. One of the main challenges is to maintain a trade-off between a scaffold's porosity and stiffness [3]. Here, the built-in, nature-like randomness of our topologically optimized designs, and the possibility to modify mechanical properties without changing the substrate material or porosity, favors such parametric solutions. The inherently stochastic structure means that in any possible direction of impact there always will be a subset of elements aligned with that direction, independent of the orientation of the regularly repeating structural motifs [3, 202, 203] such as unit cells or building blocks. This feature might be of utility for unpredictable loading scenarios such as in dynamic shock-attenuating structures, or even in the absence of gravity.

Examples might include prostheses [204], athletic gear, or earthquake-resistant structures. An excellent review of the variety of additive manufacturing methods for biomedical engineering can be found here [69].

Limitations and outlook

For simulated loading and optimization, the elements of lattices were assigned a fixed length-to-cross-sectional radius ratio, *i.e.*, shorter elements were thinner and longer elements were thicker. Conversely, for additive manufacturing, the element radius was set to a constant value (regardless of the edge length). That was a technical limitation imposed by the resolution of the available 3D printing equipment. Although there is still room for improving the fidelity of the embodiment, we find it promising that these principles of bioinspired topological optimization can be numerically captured and further developed as a generic protocol for making useful, light-weight load-bearing structures for a variety of engineering purposes.

Among the key limitations of our study is the assumption of linear elastic behaviour for the polymer, which is a viscoelastic material. However, this assumption is alleviated given the comparative procedure followed among the adopted groups in this study, and that the viscoelastic effect is negligible at low strains (*i.e.* in the order of 0.5%) [181]. Another limitation is the discrepancy between simulation and experiment in terms of the cross-sectional area of the lattice elements. This could possibly explain why the scaled-up lattices were paradoxically lighter and stronger than predicted.

5.5 Conclusions

This work has demonstrated the possibility for designing and manufacturing lightweight and stiff biomimetic lattice structures following an iterative topological optimization approach based primarily on the pruning of idle elements. Since the protocol is topological, the optimized

structure can be embodied at different scales with various materials, and, it can be subject to further morphological refinement (*e.g.* adding anisotropy, stiffness gradients, combinations of materials, and others). Moreover, this frugal and resource-conserving paradigm of design and manufacturing should become a primary industrial concern for sustainability in the face of the ever-increasing ecological fragility of our Earth.

Acknowledgements

The authors thank the 3D printing facility (The Cube) at McGill University, particularly Amar Sabih and Kevin Alforque, as well as the 3D printing facility at École Polytechnique de Montréal, particularly Prof. Daniel Therriault, Kambiz Chizari, Rouhollah Farahani and Juliette Marie Lucie Pierre. The authors also wish to thank the following funding sources: NSERC-Discovery, NSERC-Engage (EGP2 537121 – 18), Object Research Systems Inc., Montréal, Québec, Canada, and McGill University. MDM is the Canada Research Chair in Biomineralization, and this research was undertaken, in part, thanks to funding from the Canada Research Chairs program. MDM and FT are members of the FRQ-S Network for Bone and Oral Health Research. AAA would like to thank a scholarship from Fonds de recherche du Québec – Nature et technologies (FRQNT), Quebec, Canada.

5.6 Supplementary Materials

5.6.1 Detailed methods

5.6.1.1 Design of biomimetic lattice structure

Analysis of the reference graph:

Trabecular bone samples for reference lattices were obtained from the Maude Abbott Medical Museum (McGill University, Montréal). They were scanned using micro-computed

tomography and the reconstructed 3D images were processed as described in our previous study [46]. To recapitulate, a cropped binary 3D image of trabecular bone tissue was post-processed by surface smoothing (kernel size 5), and by obliterating small pores that were not connected to the background (Figure 5-8a,b). Then, the image was skeletonized replacing every trabecula by a single-voxel-thick centroid. A graph (assembly of edges and nodes) was produced from this skeleton. In a graph, a node represents the intersection of two unique single-voxel-segments and every unique single-voxel-segment constitutes an edge (Figure 5-8b). Note that at this stage of graph representation, the morphological parameters of trabecular size, shape and cross-section are excluded. The graph was then pruned by trimming short dead ends and removing duplicate or isolated edges or nodes (see procedure in Bone Reports 2020) [46, 199, 200]. Then, nodes and edges were exported from each graph as a CSV file.

Generation of naïve/initial design:

The first step in producing a biomimetic naïve structure was generating a population of nodes filling a given 3D volume with their mean density and randomness similar to that of the nodes of the reference graph (Figure 5-8c). To analyze the node distribution in a reference graph, the node spherical coordinates were imported into MATLAB (Release 2018b, The MathWorks, Inc., Natick, Massachusetts, USA). The radial component of the spherical node coordinates was normalized and tested to fit a suitable probability distribution function (SPSS Statistics). A “Beta” probability distribution matched the distribution of radial coordinates. The probability distribution of the second spherical coordinate, *i.e.* φ , matched a Gaussian distribution whereas the third spherical coordinate θ approximately followed a uniform distribution. The fitted beta, Gaussian, and uniform probability distribution models were then used to create a biomimetic population of nodes for a biomimetic naïve lattice. The probability distribution functions of the coordinates of

the biomimetic design were confirmed to match those of the reference bone lattice (Figure 5-9). Also, a comparison between the spherical coordinates' distribution of the reference bone and naïve biomimetic nodes is provided in Figure 5-11, indicating similar trends. It is important to note that the biomimetic nodes were initially generated in a larger spherical volume, from which a cube was cropped (Figure 5-10). In this way, the possible boundary effects could be avoided in the node population.

After positioning nodes in a 3D volume with a desired density and randomness, these nodes were excessively connected to form the naïve graph. First, a 3D Voronoi tessellation of the nodes was generated (Figure 5-8d) [205]. Then each node n was connected to the 5 nearest nodes located within the Voronoi cells that share the boundary with the cell of the node n (Figure 5-8e). Of note, the number of cells sharing the boundary with the cell of the node n could be higher than 5. However, considering that 98% of the nodes in the reference graph are the nodes of 3, 4, and 5 neighbours, we selected 5 as the initial connectivity of the naïve graph [199, 200].

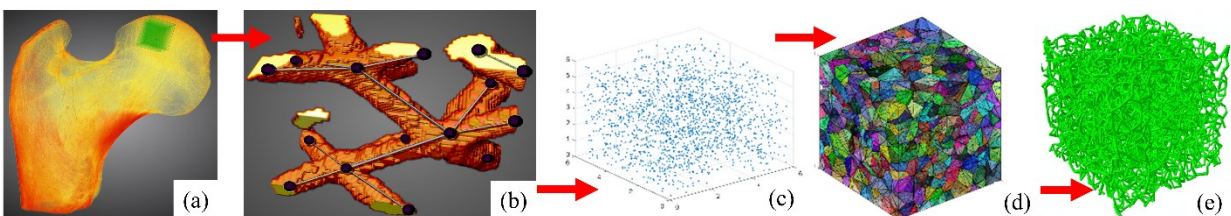


Figure 5-8: Framework of the bioinspired topological design; (a) natural material scan (i.e. femoral head of trabecular bone), (b) graph generation, (c) biomimetic node population, (d) Voronoi tessellation for biomimetic nodes, and (e) element generation for naïve lattice.

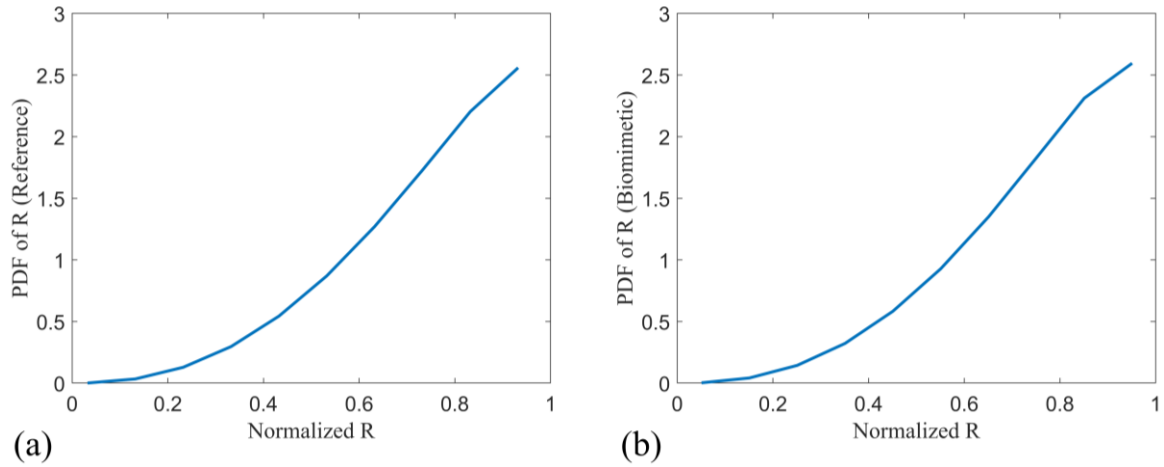


Figure 5-9: Comparison between the probability distribution functions of the radial coordinates obtained from (a) reference and (b) biomimetic naïve lattices showing agreement.

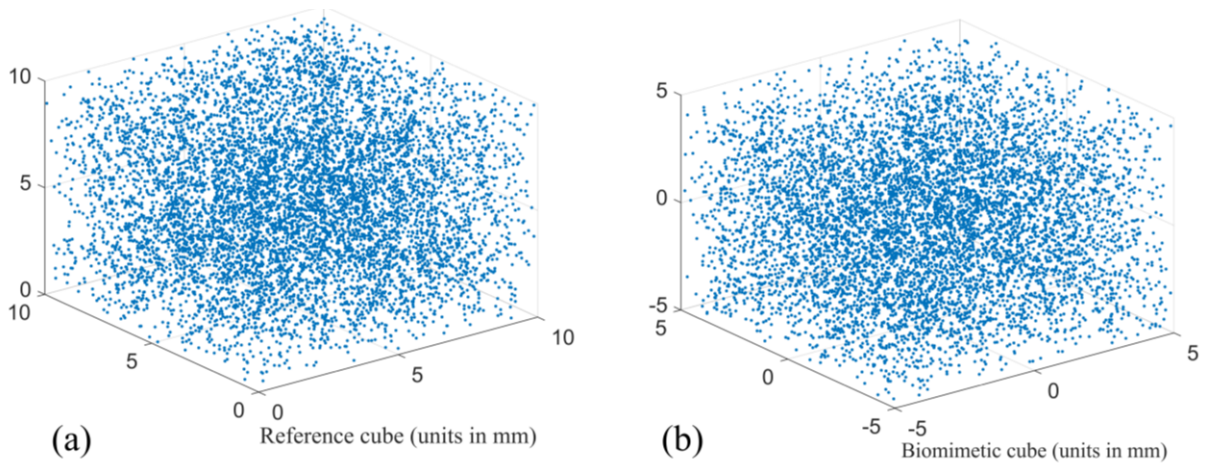


Figure 5-10: (a) Distribution of nodes from the reference cube compared with (b) distribution of nodes from the inscribed naïve biomimetic cube.

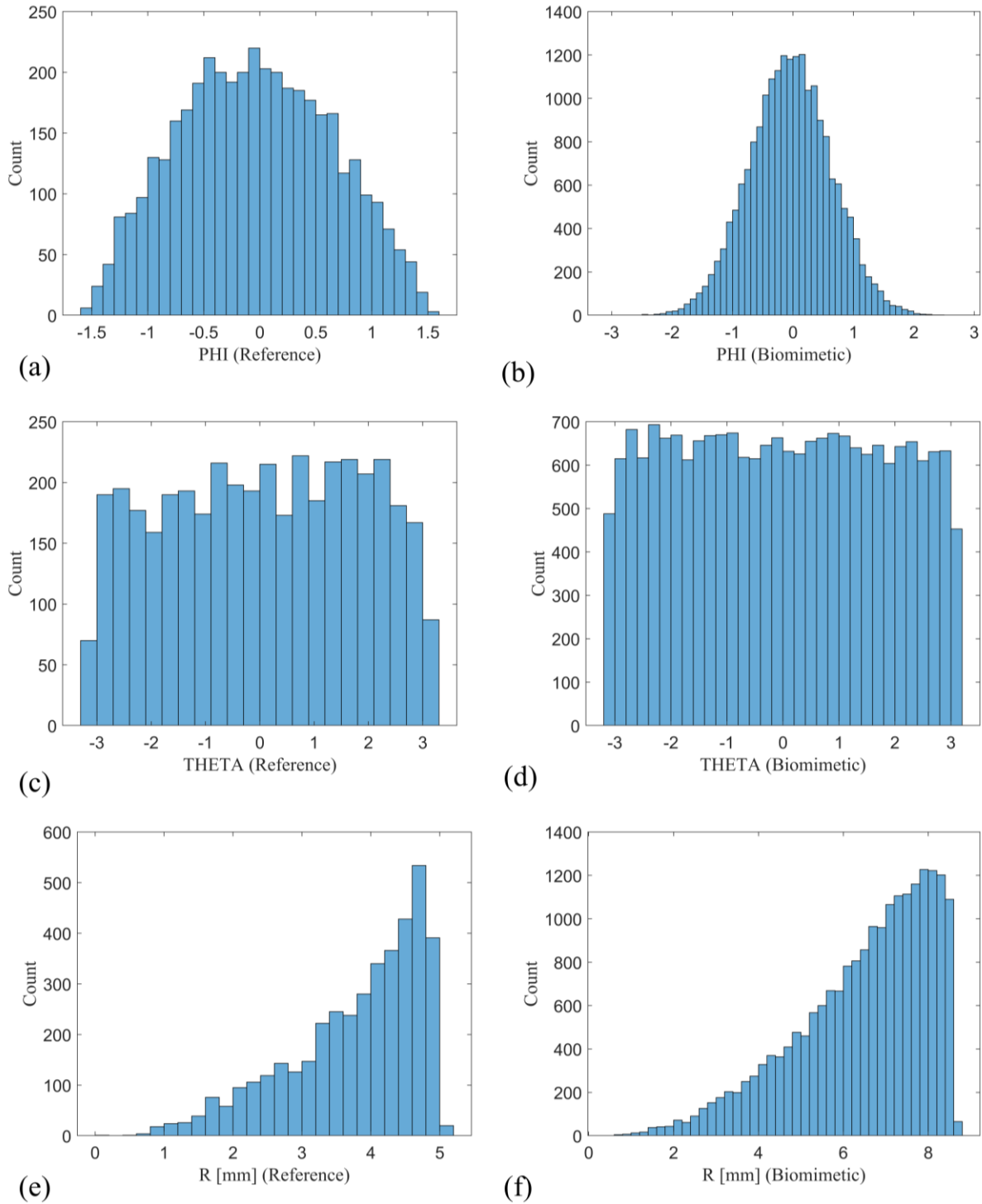


Figure 5-11: Histograms during the node generation process. Comparison between the spherical coordinates' distribution of the nodes from reference bone lattice (on the left) and naïve biomimetic lattice (on the right). (a & b) histograms showing count of spherical coordinate phi – units in Rad; (c & d) histograms showing count of spherical coordinate theta – units in Rad; (e & f) histograms showing count of spherical coordinate R.

5.6.1.2 Numerical simulation and optimization

Finite-Element Analysis (FEA) of reference lattice and biomimetic lattices:

For FEA, Abaqus (Version 6.17, Dassault Systems Simulia Corporation, Johnston, RI, USA) was used as the solver, and MATLAB was used for pre- and post-processing. Skeletonized bone samples provided as CSV files were imported into MATLAB for preprocessing where an Abaqus input file was prepared and then submitted to Abaqus solver. The output from Abaqus was imported again into MATLAB for postprocessing. Reference and biomimetic graphs were converted into lattices for FEA by adding a uniform circular cross-sectional geometry to all the graph edges based on a fixed length-to-cross-sectional radius ratio of 8:1 [62, 206]. Then, each circular beam was rendered as a Timoshenko beam in order to account for transverse shear behavior. The elastic modulus of each element was set at 1.6 GPa (based on the elastic modulus of the polymer used for 3D printing [207]) with a Poisson's ratio of 0.3 [208]. The numerical simulations of the lattices were conducted under both uniaxial and triaxial compressive loading with a linear elastic analysis. A displacement compressive loading was applied until 0.7% compression of the sample, as arbitrarily selected to correspond to bone yield compressive strength [209]. In the case of uniaxial compression, the compressive displacement was applied to the nodes located on the lattice aspect perpendicular to the z-direction and nodes on the opposite aspect were fixed in the x, y, and z directions. To simulate a multidirectional loading scenario in triaxial compression, the compressive strain was applied to the nodes of 3 lattice aspects perpendicular to the x, y, and z directions, and nodes on the opposite aspects were fixed only in the same direction of the compressive displacement (Figure 5-15).

The FEA outputs of interest were the stiffness, effective modulus (Young's modulus) normalized by weight, maximum von Mises stress (indicating stress concentrations within the

lattice) normalized by the effective modulus, standard deviation of maximum von Mises stress, and the percentage of bend-dominated elements versus stretch-dominated elements. The percentage of bend-dominated elements was obtained by dividing the number of elements that had a lateral sectional-force component greater than the axial force component by the total number of elements in the lattice. The highest maximum Mises stress and its standard deviation were normalized by the modulus because stiffer structures would build up higher stresses under displacement-controlled compression.

The milestone criterion for the optimized-Generation 1 lattice was the attainment of the minimum standard deviation for von Mises stress divided by the modulus normalized by the lattice weight. The weight of a lattice corresponds to the collective volume of elements multiplied by the specific density of the printing material. The arbitrary volume/amount of material of a lattice at each stage of optimization was calculated by multiplying the length of each element by its assigned thickness and summing that over all elements. The milestone criterion for the optimized Generation 2 lattice was achieved when the optimized lattice had the collective mass of elements equal to that of the reference lattice. Note that here the mass of elements is an abstract characteristic because the thickness, volume and density of the elements were artificially assigned to the edges in order to embody a graph for FEA. Following further optimization, the number of elements of the biomimetic lattice was reduced to achieve the number of elements in the reference lattice, and that was the optimized –Generation 3 lattice.

For all the lattices, to calculate the overall macroscopic effective stress of the structure $\bar{\sigma}$, the reaction forces F^R at fixed nodes on each face in the direction of applied displacement were summed and divided by the corresponding cross-sectional area of the face A , such that $\bar{\sigma} = \frac{\sum_i^N F_i^R}{A}$ [210]. The effective uniaxial modulus E was calculated by dividing the effective stress $\bar{\sigma}$ by the

effective compressive strain $\bar{\epsilon}$ such that $E = \frac{\bar{\sigma}}{\bar{\epsilon}}$. In the case of triaxial compression, the bulk modulus, which relates the change in pressure to the change in volume due to the triaxial compression, was considered instead of the uniaxial (*i.e.* Young's) modulus. The bulk modulus K , which measures the material's resistance to compression, was approximated by dividing the mean effective stress by the volumetric strain such that $K = \frac{(\bar{\sigma}_{xx} + \bar{\sigma}_{yy} + \bar{\sigma}_{zz})/3}{\bar{\epsilon}_{xx} + \bar{\epsilon}_{yy} + \bar{\epsilon}_{zz}}$ [210].

FEA-based iterative optimization procedure:

For the biomimetic lattice, reduction of idle elements started by iteratively subjecting it to a displacement-controlled compression of 0.7% strain through FEA (Figure 5-12). Following each iteration, a pre-defined number of elements with minimum von Mises stresses ("idle elements") were removed [29, 211] (see Table 5-4). However, in the case where removing an element would convert a 3-N node to become 2-N node (a 2-N node is essentially a kink, not a node), that element was kept intact. Following this algorithm, each loading iteration results in identification of a subpopulation of idle elements with the entire set of lattice elements, and these idle elements would be eliminated while preserving the minimal node coordination of 3. Also, for each iteration, areas of stress concentrations in the structure were identified by locating the element with the highest von Mises stress. To eliminate stress concentrations, an extra element was added to augment the regions of high stress following the concept of triangulated structures [188], which are commonly known for their stretch-dominated behaviour [64]. A triangle was formed by connecting one node belonging to a highly stressed element to the closest neighbour of the second node of that highly stressed element (Figure 5-13). The iterative procedure continued until reaching a convergence condition (*i.e.* reaching 85% of the number of elements of the reference lattice; Figure 5-12). The mechanical properties of the evolving lattices and their CDC were monitored for each optimization

steps and those of naïve, optimized Generation 1, 2, and 3 were compared to the mechanical properties of the reference lattice. The CDC was used for comparing the topology of different groups. Figure 5-14 illustrates the idea of the CDC. When nodes with different coordination equally participate in the space filling lattice in equal proportions, the DC is zero. When the nodes of lower coordination prevail (i.e. nodes of 3 and 4 neighbours), DC is negative and the network is more compliant; when the nodes of high coordination prevail (i.e. nodes of 5 and 6 neighbours), DC is positive and the network is more rigid.

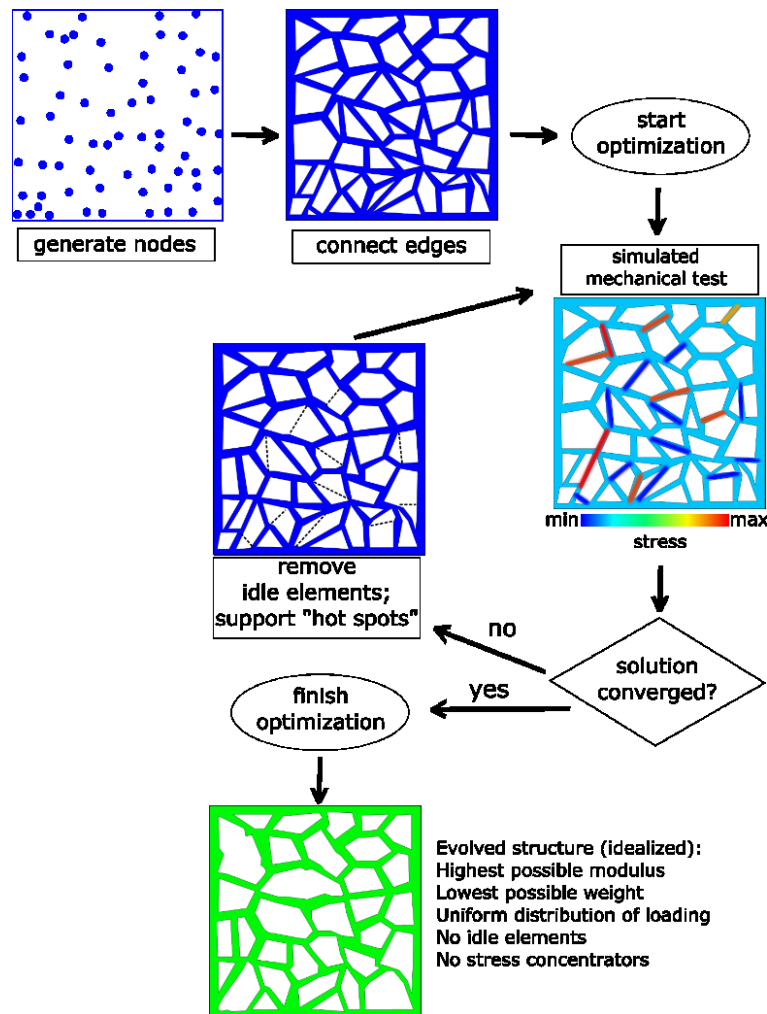


Figure 5-12: 2D representation of optimization procedure; after nodes are generated and connected by edges, the iterative optimization procedure starts with subjecting the naïve structure to a compressive loading using FEA. In each iteration the elements with the minimum equivalent stress were removed and a supporting element was inserted to strengthen regions of high stress and

alleviate hot spots in the structure following the concept of triangulation with relatively short elements.

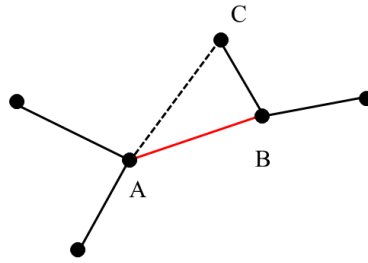


Figure 5-13: Augmentation of elements through the concept of triangulation: A new element is added between nodes A and C to support the highly stressed element AB forming triangle ABC.

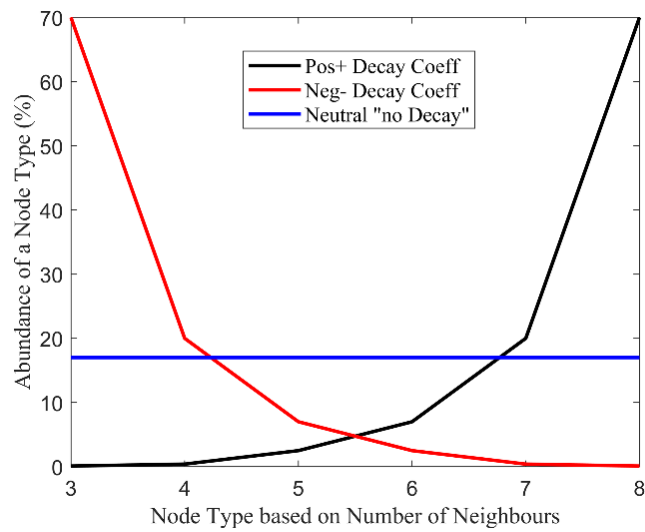


Figure 5-14: Relationship between node type based on the number of neighbours and the connectedness decay coefficient of the abundance of each node type. The black curve represents an exponential decay with a positive decay coefficient whereas the red curve represents an exponential decay with a negative decay coefficient.

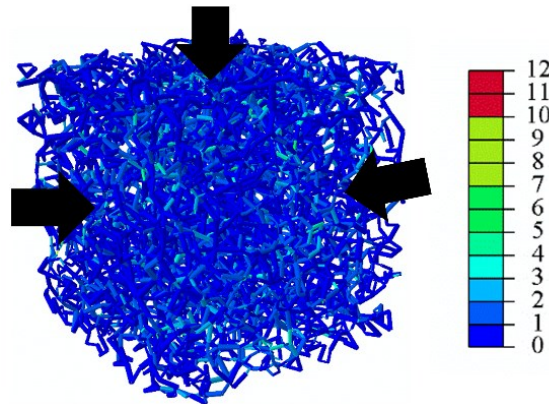


Figure 5-15: Compressive loading of Contours of triaxial compression during topology optimization showing contours of maximum von Mises stress in [MPa] generated through finite element analysis for the biomimetic OptGen2 indicating uniform stress distribution, with black arrows indicating the direction of applied compressive displacements on the loading surfaces. Note that surfaces opposite to the loading surfaces were fixed in the direction of the compressive displacements.

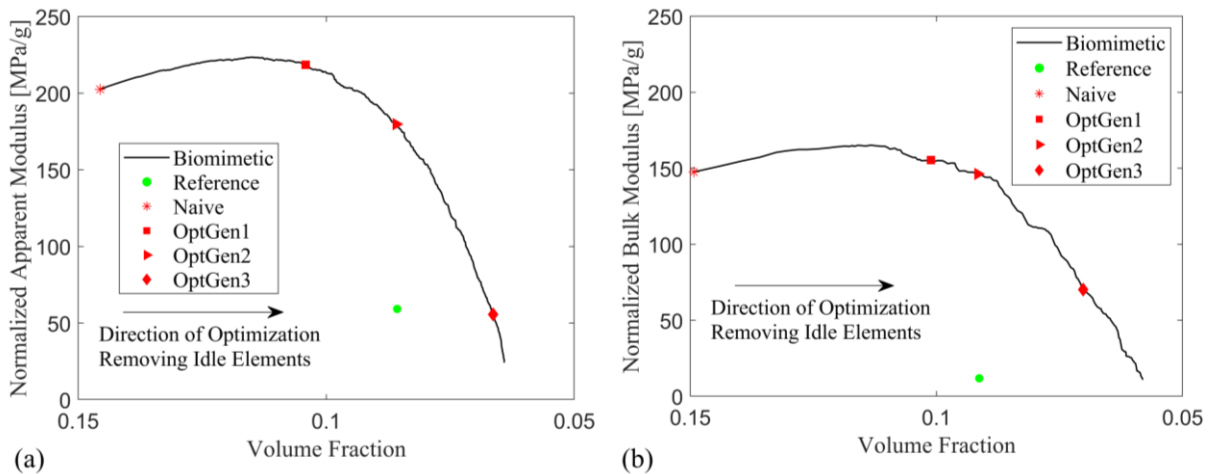


Figure 5-16: Normalized modulus versus volume fraction for (a) uniaxial-based optimization; (b) triaxial-based optimization.

5.6.1.3 Validation of repeatability, size, and scale independence

Biomimetic optimization was repeated on different lattice sizes to investigate the effect of size on the overall trend of optimization. Cubic lattices with edge sizes of 5 and 10 mm were considered. The optimization procedure was repeated on the 10 mm lattices to test the effect of

changing the exact coordinates of the nodes while preserving their probability distribution and randomness. Then, experimental testing was conducted on original 5 mm cubic lattices as well as on scaled up 5 mm lattice by a factor of 4 (*i.e.* edge size of 20 mm).

5.6.1.4 Validation of topologically-optimized architecture using 3D additive manufacturing.

Sample preparation for experimental test:

The reference lattice, naïve biomimetic lattice and the optimized lattices of 3 generations were 3D printed and tested experimentally under uniaxial compression. Since lattices – as opposed to the dimensionless graphs – have a certain element thickness attributed to the interconnected edges, such structures can be surface-meshed and exported for additive manufacturing. Surface-meshed files of 5 lattices were exported as STL files as shown in Figure 5-17 (Dragonfly™, ORS, Montréal, Québec, Canada) and were printed using a Form2 3D printer (Formlabs, Somerville, Massachusetts, USA) and photo-polymerized methacrylate resin with a Young's Modulus of 1.6 GPa [207] and a deposition layer thickness of 0.025 mm (see Figure 5-18 for images of 3D printed samples). Uncured resin was removed from the printed prototypes in an isopropyl alcohol bath for 20 minutes, and then the prototypes were post-cured under UV light for 15 minutes at 60° C.

Experimental compressive test:

A displacement-controlled uniaxial compression test was conducted using a Mach-1 mechanical tester (Biomomentum Inc, Montréal, Québec, Canada) with a load cell of 250 N to test original samples and MTS-Insight machine (MTS Systems Corporation, Eden Prairie, MN, USA) with a load cell of 1 kN to test scaled-up samples. Both machines applied a strain rate of 0.007/sec. Before the test, each prototype was weighed, and its external volume was measured 3 times. Each cubic prototype was positioned exactly at the center of the lower anvil. The stiffness of the

structure was obtained by calculating the slope of the linear portion of the load-displacement curve generated from the experiment. The uniaxial modulus was calculated by multiplying stiffness by the sample's height and dividing that by the cross-sectional area perpendicular to the direction of compression.

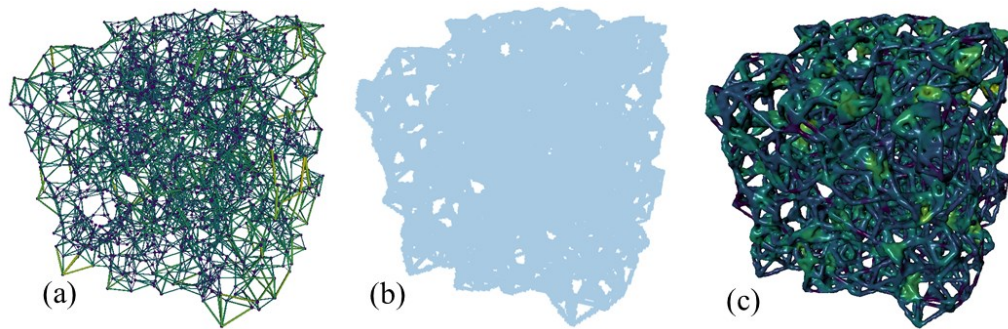


Figure 5-17: Generation of stereolithography (STL) mesh files for synthetic graphs (Dragonfly™, Object Research Systems, Montreal, QC, Canada). (a) Biomimetic graph; (b) every edge in the graph is replaced with a segment of one-voxel thick (voxel representation of a graph); (c) STL mesh file obtained from the voxel representation.

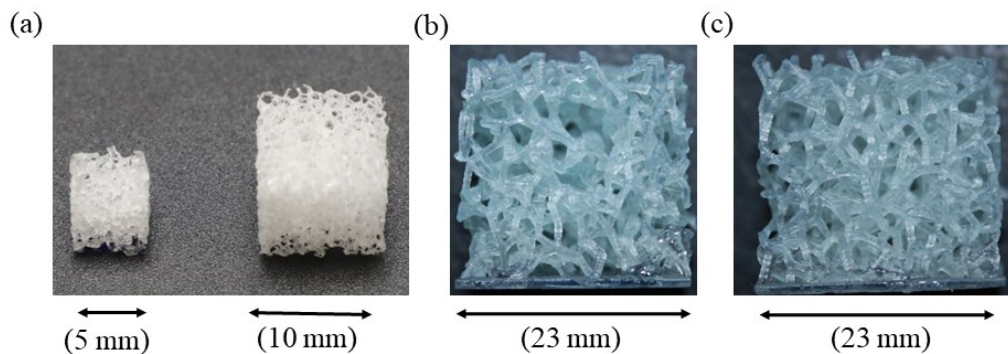


Figure 5-18: (a) images of 3D printed biomimetic lattices with different sizes; (b) image of scaled and 3D printed OptGen3 biomimetic lattice; (c) image of scaled and 3D printed reference lattice.

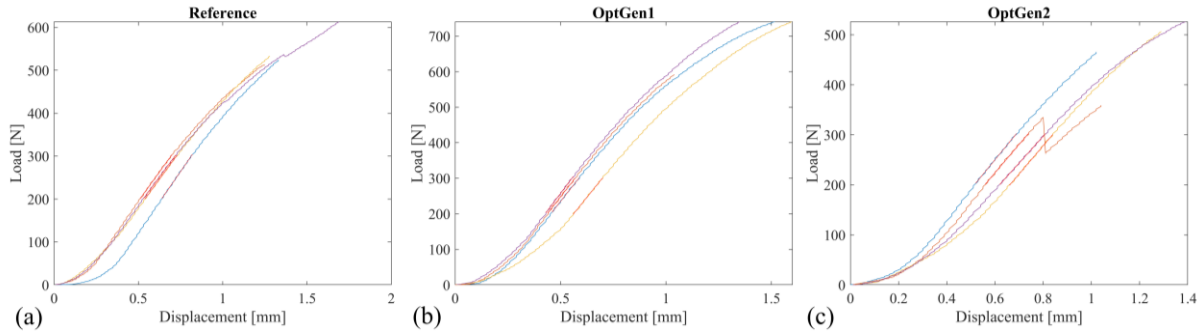


Figure 5-19: load-displacement curves for uniaxial compression of reference and biomimetic lattices generated from uniaxial-based optimization.

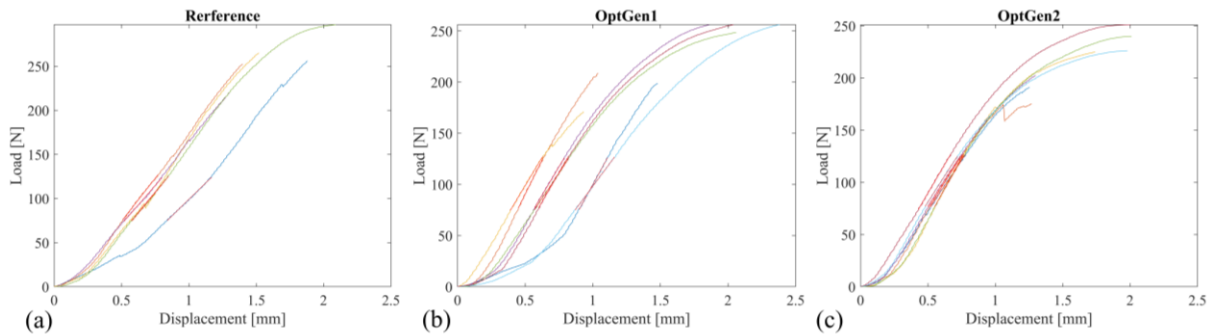


Figure 5-20: load-displacement curves for uniaxial compression of reference and biomimetic lattices generated from triaxial-based optimization.

5.6.2 Sensitivity study on the effect of the optimization increment size

The increment size refers to the number of elements being removed in each iteration. According to the results presented in Table 5-4, it was concluded that increasing the speed of optimization by removing more elements each iteration and reducing the number of iterations from 895 to 167 (68.5 % reduction) led to a 2.8% decrease in the effective uniaxial modulus and 4.2% in the normalized effective uniaxial modulus of OptGen2 lattices. For OptGen1, the normalized effective modulus was decreased only by 0.2%. Accordingly, the algorithm is not very sensitive to removing more elements each iteration, which indicates its robustness and flexibility to accommodate fast optimization. In addition, removing more element each iteration affects OptGen2 greater than OptGen1.

Table 5-4: The effect of number of elements to remove each iteration and the element removal increment on the speed of optimization and mechanical properties of the synthetic lattice.

	Reference	Naïve	OptGen2 Attempt 1	OptGen2 Attempt 2	Percentage Difference (Design 1 & Design 2) [%]
Number of elements to remove each iteration	-	-	50	200	-
Element removal increment	-	-	0.2 x Num of Elements to remove	0.5 x Num of Elements to remove	-
Sample volume [mm ³]	200	200	200	200	0.0
Number of elements	2720	5226	2665	2644	0.4
Number of nodes	1761	1761	1761	1761	0.0
Avg element length [mm]	0.417	0.440	0.426	0.428	0.2
Number of iterations until end of optimization	-	-	895	167	68.5
Volume of elements [mm ³]	9.7	19.6	9.7	9.7	0.0
Decay Coefficient	-1.5	0.56	-1.0	-1.0	0.0
Uniaxial Effective Modulus [MPa]	27.9	75.7	23.9	22.6	2.8
Normalized Uniaxial Modulus [MPa/ mm ³]	2.9	3.9	2.5	2.3	4.2
Max von Mises stress [MPa]	118.4	176.5	141.6	133.5	2.9
SD of von Mises Stress [MPa]	17.1	17.3	15.8	16.2	1.3

6 General Discussion

The main objectives of this dissertation were to optimize the surface and bulk designs of additively manufactured dentures and cellular structures, respectively. For optimizing surface design, the goal was to strengthen metal/polymer interfaces in removable partial dentures (chapter 4) whereas for optimizing bulk design the goal was to achieve cellular structures of high stiffness-to-weight ratio (chapter 5). A bioinspired optimization approach that favors a uniform stress distribution was followed to achieve both goals. The main rationale was that natural materials often possess optimized structures offering combinations of mechanical properties that often surpass those of their synthetic counterparts [29, 188, 192, 193].

Although the design optimization of structures adopted in this dissertation focused on a bioinspired approach (i.e. chapters 4 and 5), chapter 3 investigated the design optimization problem through analytical modeling. This is because the author intended to highlight the range of required assumptions and necessary simplifications to obtain a closed form solution for the design optimization problem. A relevant problem was selected, which was the design optimization of a circumferential clasp, a critical component of RPDs. Even for the case of a circumferential clasp, which is considered relatively simple, several assumptions were necessary to simplify the problem (chapter 3). Examples included limiting the mode of loading to a pull-out force instead of cyclic loading. Although, sometimes failure in the clasp could occur due to a pull-out force caused by certain types of food such as caramel candy, chewing gum, or toasted bread [105], it would be more comprehensive to consider a cyclic load to account for fatigue failure of the clasp due to mastication. Moreover, the simplified model did not allow for twisting which might be significant during the mastication process. Although the retention force may not be very sensitive to twisting, the stresses at the shoulder caused by the torque could still be quite high. Finally, it was also

necessary to assume that the deflection at the clasp free end approximates the undercut engaged by the circumferential clasp. Given such limitations of the analytical modeling approach, besides other shortcomings detailed in chapter 3, bioinspired design optimization, based on iterative FEA, mimicking natural iterative process of development, reproduction, and selection [18] was the main focus of this dissertation. The bioinspired design optimization approach was explicitly investigated in chapters 4 and 5.

It was intriguing that the bioinspired shape optimization technique in chapter 4 suggested a Y-shaped interlocking metal design, to strengthen metal/polymer interfaces, similar to the roots of mangrove trees. However, it is important to highlight that the root-shape design for the interlock may not be as superior when different objective function or constraints are considered. For example, stress in the polymer could be chosen as the objective function and a constraint could be imposed on the volume of material in metal. However, for the considered analysis, the goal was to maximize the interfacial strength and stiffness. Since the applied strain was fixed, the strength correlates with the stiffness. Hence, the compliance was considered for the objective function. In addition, the initial design was selected as a T-bar to begin the search because it provides a naïve interlocking behaviour. Selecting a different initial design by the user would also affect the final result. This issue was ameliorated in chapter 5 by developing an algorithm for providing the initial design, which reduces the effect of user input.

In chapter 5, the influence of user input on the initial design was more constrained. Most of topology and shape optimization techniques focus on the optimization stage and disregard the initial design, which is well-known to affect the end results of optimization [20]. Chapter 5 proposed a novel method for initial (naïve) design inspired by the architecture of natural materials. The bioinspired initial design procedure starts with populating a set of nodes in the design space

based on the probability distribution of nodes extracted from natural materials. A 3D Voronoi tessellation of the nodes was then established. Nodes belonging to Voronoi cells that share a boundary were connected by an edge producing a redundantly interconnected lattice. Starting from that naïve design, the topology optimization procedure applies an iterative compressive loading and removes idle elements to motivate a uniform distribution of stresses. The optimization curves in Figure 5-2 and Figure 5-3 show that mechanical properties of the biomimetic structures located between the naïve and OptGen2 are not much affected by removing the idle elements. This has also been reflected in Figure 5-15, which shows the distribution of the maximum values of von Mises stresses within the elements of the optimized biomimetic structure OptGen2. As seen in the figure, red spots indicating localized stress are rarely found, which highlights the efficiency of the iterative methodology use to develop the biomimetic structure. We may see further avenues for improvement in the design by applying an alternative method for the initial design formation, e.g. a Turing reaction-diffusion pattern, instead of a Voronoi pattern. Moreover, other loading conditions such as pure shear could be investigated to provide further validation of the independence of the results provided by the optimization algorithm on the mode of loading.

For the biomimetic design optimization of lattices in chapter 5, it was interesting to see that for the same amount of material, bone has a lower connectedness in its lattice indicating different topology (Figure 5-2 and Figure 5-3). The lower connectedness of bone lattice indicates lower percentage of simple nodes (i.e. majority of nodes with 3-neighbours). The prevalence of low valence nodes apparently makes the network robust against random impacts, as opposed to hierarchical networks where destruction of the hub would result in disintegration of the whole [199, 200]. Hence, trabecular bone network is decentralized, non-hierarchical, and sparsely connected spanning maximal 3D volume [199, 200]. It is important to highlight that, while the

local morphological features vary from one site to another, the network topology of trabecular bone is seemingly invariant among anatomical sites and it presents a stable fundamental basis for functional adaptations [199, 200]. The same topological blueprint can accommodate thicker or thinner elements (i.e., different local morphologies) to serve different functions such as load-bearing or shock absorbing. The high connectedness of the optimized biomimetic structure emerged as a result of tuning the optimization algorithm towards achieving a structure with a high stiffness-to-weight ratio for load-bearing application, which led to the development of some complex nodes (i.e. nodes with high connectivity). Another implication of that observation could also be that trabecular bone does not necessarily use Voronoi tessellation to form its elements.

Despite the aforementioned limitations of the bioinspired design optimization procedures followed in chapters 4 and 5, the established methodologies presented in this dissertation constitute practical frameworks that could be easily adjustable according to the user's requirement. The optimized designs suggested for both bulk and interfaces were additively manufactured successfully using metal and polymer materials, respectively. Moreover, these frameworks are based on extrapolation of the design optimization principles learnt from natural structures, such as trabecular bone, and they provide a design recipe for structures and interfaces with enhanced mechanical properties that can be optimized to serve various biomedical and engineering applications.

7 Conclusions and Future Perspectives

7.1 Conclusions

Specific conclusions are listed as follows:

- Design optimization through analytical modeling was explored and used for designing circumferential clasps in additively manufactured RPDs for molar and premolar teeth. It was concluded that circumferential clasps constructed in laser-sintered Co-Cr alloys are more susceptible to fail in premolars compared with molars, given that both clasps are subjected to the same load
- Morphological bioinspired shape optimization (particularly stress-induced material transformation) was explored and used besides the mesh adaptive direct search algorithm for the first time to propose optimized interlocking feature design that can be additively manufactured on laser-sintered dental and biomedical prostheses to improve the strength and stiffness of metal/polymer (i.e. Co-Cr/PMMA) interfaces. The newly proposed interlocking retention design provided better mechanical performance compared with a conventional retention method.
- A topological bioinspired design optimization framework for cellular structures was developed and coupled with probability distribution models to generate a naïve biomimetic design, which was then optimized through an iterative bioinspired algorithm. Through this framework, space-filling lattice structures with various properties could be designed for various engineering applications.

7.2 Future perspectives

Specific future perspectives are listed as follows:

- For optimization of metal/polymer interfaces (i.e. chapter 4), it is crucial to note that further studies should be conducted to assess the behaviour of the interlocking mechanical features with state-of-the-art chemical bonding agents. Other modes of loading should also be investigated such as compression, pure shear, and cyclic loading to evaluate the performance of the proposed Y interlock.
- Similarly, for topological optimization of cellular structures (i.e. chapter 5), other modes of loading should be investigated in particular pure shear to evaluate the performance of the proposed bioinspired algorithm. The use of different building materials and additive manufacturing technologies, such as 3D printing with metals, should be experimentally investigated. In addition, further investigation should be conducted to assess the suitability of the proposed algorithm for producing structures with variable anisotropy.
- It is important to highlight that the proposed design optimization methods, for interfaces and bulk, in this dissertation are not limited to applications in dental or orthopedic prostheses and could be extended to various biomedical and engineering applications. The models incorporate multiple parameters that could be tuned and optimized to serve various functions. Moreover, the fabrication of such structures becomes more feasible with the advancement of additive manufacturing. Placing structural material where it is needed and eliminating it where it is idle is economical and sustainable.
- Particularly for chapter 5, benefits of lightweight and stiff structures under multidirectional loading can be best appreciated in the aerospace and transportation industries. Reducing the weight of structural designs is considered among the primary goals of global sustainability

because it leads to less material consumption and processing and better environmental performance. In addition, reducing weight is highly linked with reducing fuel consumption [1]. Improving environmental sustainability has been a key focus for scientists, engineers, and policy makers. Additively manufactured components have proven to be highly valuable in cutting down not only the operation costs of transportation vehicles (i.e. fuel consumption), but also the initial manufacturing costs. Since their conception decades ago, additive manufacturing techniques have not been fully exploited because traditional design methodologies remained unchanged. Reducing the weight of a structure leads to introducing holes and voids in unloaded regions resulting in very complex geometry. In general, highly complex structures are difficult to design because of the large number of variables a designer must select. Computer-aided design methods, particularly topology optimization, have proven to be the most efficient for designing additively manufactured complex structures. Therefore, topology optimization makes the production of stronger lightweight parts possible. However, particularly in the aerospace industry, there exists little application to real-world design problems, including all the complexities required to convince industry leaders to abandon their design heritage and start the design process afresh. This dissertation proposed a novel initial (i.e. naïve) design strategy for structures, able to mimic a reference design, to inform the topology optimization algorithm. The reference design could be a natural design or an existing traditional design close to optimal. In other words, the optimization process in industry could start with guessing the available traditional design, and then topology optimization could be used to reduce its weight by removing unnecessary material. This concept may be appealing to industry decision makers because they will be able to exploit their design heritage to reduce the weight of parts while preserving the strength and the overall external shape.

8 Appendices

8.1 Appendix A: MATLAB and Abaqus UMAT codes for shape optimizing using Finite Element Analysis in Chapter 4

Overview: MATLAB was used to initiate the iterative simulation process with an initial elastic modulus assigned for elements in metal and polymer. So, MATLAB builds and submits the Abaqus input file to UMAT, where the stress-strain relationship (i.e. material model) was executed and the von Mises stress as well as the elastic modulus for each element were treated as state variables. UMAT writes an output file containing the von Mises stress in each element and this file is then read by MATLAB to update the elastic modulus based on the stresses.

If you use these codes, please cite our manuscript “Bioinspired and optimized interlocking features for strengthening metal/polymer interfaces in additively manufactured prostheses”

MATLAB code

```
% MATLAB Code for Shape Optimization of Two Materials Based on FEA %
% This code is to be used with Abaqus Standard and user subroutine UMAT %
% Written by : Ammar Alsheghri %
% McGill University %
%%%%%%%%%%%%%%%%%%%%%%%%%%%%%%%%%%%%%%%%%%%%%%%%%%%%%%%%%%%%%%%%%%%%%%%%
% Important: to use this code you MUST do the following first:
% 1- Specify the number of mesh elements for each material in lines 17 & 18
% 2- Prepare an Abaqus input file and replace the material properties by
% UMAT specific properties such as:
%*USER MATERIAL,CONSTANTS=1
%0.3
%*DEPVAR
%6
% 3- Specify the total number of elements in the UMAT .for file: line 58 in
% the provided .for file.
close all; clear all; clc;
%
```

```

No_Ele = 0;
K = 20000; % Parameter for optimization model
E_CoCr = 200000.000000; % Elastic Modulus of CoCr (MPa)
E_PMMA = 2400.000000; % Elastic Modulus of PMMA (MPa)
Ref_Stress = 65; % Reference Stress (MPa)
Noel_PMMA = 6588; % Number of Elements in PMMA
Noel_CoCr = 88; % Number of Elements in CoCr
Noel = Noel_PMMA + Noel_CoCr;
Iteration = 0; % Number of Iterations of code
Terminate_value = 0; % This value is used to terminate the loop
Number_Elements = 1;
%
% Define the Initial Elastic Modulus
%
for i =1:Noel_CoCr
    E(i) = E_CoCr;
end
%
for i = i+1:Noel
    E(i) = E_PMMA;
end
E = E';
%
%% Start of Simulation Iterations
%
while Terminate_value < 2
%
% Write the Initial Elastic Modulus to File 'Modulus1' AND 'Modulus2'
%
INITIAL_MODULUS_FILE = fopen('Modulus.dat','w');
fprintf(INITIAL_MODULUS_FILE, '%f\n',E);
fclose(INITIAL_MODULUS_FILE);
%
% Submit Abaqus Job through UMAT
%
dos('cd "C:\Temp\simulation directory File " && "C:\Program Files
(x86)\Microsoft Visual Studio 9.0\VC\bin\vcvars32.bat" & "C:\Program Files
(x86)\Intel\Compiler\11.1\048\bin\intel64\ifortvars_intel64.bat" & "C:\Temp\

```

```

simulation directory File\CommandFile.bat" && "C:\WINDOWS\system32\cmd.exe"
/k exit')
%
% Reading The stress from previous step and saving into Mises_Int
% where Mises_Int is Mises Stress at every integration point
%
STRESS_FILE = fopen('Stress.dat','r');
formatSpec = '%f %f %f';
Size = [3 Inf];
Stress_i = fscanf(STRESS_FILE,formatSpec,Size); % Previous Stress File
fclose(STRESS_FILE);
Stress_i = Stress_i';
Mises_Int = Stress_i(:,1); % Mises stress at Integration Points
%
% Calculating Average Mises Stress for Each Element: Every consecutive four
% integration points are averaged into an equivalent Mises for the element
%
k = 0;
for j = 1:size(Mises_Int)/4
    Mises_El(j) = 0;
    for i=1:4
        k = k + 1;
        Mises_El(j) = Mises_El(j) + Mises_Int(k);
    end
    Mises_El(j) = Mises_El(j)/4; % Mises stress at Each Element
end
%
% Calculate and update The NEW Elastic Modulus for each element
%
for i = 1:1:Noel
    Current_Stress = Mises_El(i);
    E(i) = E(i) + K .* ( Current_Stress - Ref_Stress );
% Check the limits
    if E(i) > E_CoCr
        E(i) = E_CoCr;
    elseif E(i) < E_PMMA
        E(i) = E_PMMA;
    end
end

```

```

    end
end
% Update the number of iterations
No_Ele = 0; % Number of elements whose Modulus different than E_PMMA,E_CoCr
Iteration = Iteration + 1
%
% Renaming the ODB File to maintain mutliple odb files
newName = sprintf('%03d.odb',Iteration);
movefile('Job-UMAT.odb',newName);
%
% Convergence check: check if any element has a modulus value different
% than E_Co-Cr or E_PMMA. If no element was found, then terminate
%
for j=1:1:Noel
    if ( E(j)~= E_CoCr ) && ( E(j)~= E_PMMA )
        Terminate_value = 0;
        Modulus = E(j)
        No_Ele = No_Ele + 1;
    end
end
end
%
Number_Elements = No_Ele
%
% Convergence check: if no element has a different modulus, then
% terminate by making value = 2
%
if Number_Elements == 0
    Terminate_value = Terminate_value + 1;
elseif Number_Elements ~= 0
    Terminate_value = 0;
end
end
end

```

UMAT Code

```
C =====
C ===== U M A T =====
C =====
C *****
C *
C *
C *           - McGill University -
C *
C *
C *           Written by : AMMAR ALSHEGHRI
C *
C *
C *           Last Updated: June 26 2018
C *
C *****
C
C           SUBROUTINE UMAT (STRESS, STATEV, DDSDE, SSE, SPD, SCD,
C           1 RPL, DDSDDT, DRPLDE, DRPLDT,
C           2 STRAN, DSTRAN, TIME, DTIME, TEMP, DTEMP, PREDEF, DPRED, CMNAME,
C           3 NDI, NSHR, NTENS, NSTATV, PROPS, NPROPS, COORDS, DROT, PNEWDT,
C           4 CELENT, DFGRD0, DFGRD1, NOEL, NPT, LAYER, KSPT, KSTEP, KINC)
C
C *****
C           THIS SUBROUTINE IS PART OF SHAPE OPTIMIZATION ALGORITHM C
C           IT IS FOR USE IN ABAQUS/STANDARD SOFTWARE C
C *****
C           INCLUDE 'ABA_PARAM.INC'
C           CHARACTER*80 CMNAME
C           DIMENSION STRESS (NTENS), STATEV (NSTATV),
C           + DDSDE (NTENS, NTENS), DDSDDT (NTENS), DRPLDE (NTENS),
C           + STRAN (NTENS), DSTRAN (NTENS), TIME (2), PREDEF (1), DPRED (1),
C           + PROPS (NPROPS), COORDS (3), DROT (3, 3), DFGRD0 (3, 3), DFGRD1 (3, 3)
C
C --- DIMENSION, COMMON, DATA, AND PARAMETER VARIABLES THAT ARE
```

```

C     INTERNAL TO THE UMAT SUBROUTINE
C
C     DIMENSION COEF (NTENS) , ESTRESS (NTENS) , MODULUS (18311)
C     COMMON /OUT_NONL/I_TEST
C
C     DATA ZERO, HALF, ONE, TWO, THREE, FOUR/0.0D0, 0.5D0, 1.0D0, 2.0D0,
+3.0D0, 4.0D0/
C
C     PARAMETER (nwrite=1)
C
C --- OPEN THE MESSAGE FILE WHERE WRITE STATEMENTS WILL BE EXECUTED
C
C     I_TEST = 7
C     MODULUS_FILE = 9
C     STRESS_FILE = 10
C     J = ZERO;
C
C --- READING ELASTIC MODULUS VALUES INTO MODULUS(K)
C --- NOTE: KEEP THE LONG YELLO LINE COMMAND BELOW AS IT IS , OTHERWISE ,
SYNTAX ERROR
C
C     OPEN (UNIT=MODULUS_FILE, FILE='C:\Temp\directory\Modulus.dat',
+ ACTION='READ', STATUS='OLD')
C     DO K = 1 , 6676
C         READ (9,*, IOSTAT=IODT) MODULUS ( K )
C         IF (IODT.NE.0) THEN
C             EXIT
C         END IF
C     END DO
C     CLOSE (9)
C
C --- GET THE MATERIAL PROPERTIES
C
C --- POISSON'S RATIO FROM INPUT FILE
C     COEF ( 1 ) = PROPS ( 1 )
C --- YOUNG'S MODULUS: ASSIGNED FROM MODULUS2 FILE

```

```

C
      COEF( 2 ) = MODULUS( NOEL )
      STATEV(6) = COEF( 2 )
C
C --- COEFFECIENT
      COEF( 3 ) = COEF( 2 ) / ((ONE+COEF( 1 ))*(ONE-TWO*COEF( 1 )))
C
C --- RECOVERING THE INTERNAL STATE VARIABLE VALUES AT THE BEGINING
C OF THE INCREMENT. THE FIRST FOUR STATE VARIABLES REPRESENT
C STRESSES AND THE 5TH STATE VARIABLE REPRESENTS MISES STRESS
C
      DO I = 1 , NTENS
          ESTRESS( I ) = STATEV( I )
      END DO
C
C --- CALCULATING THE STRESSES
C
      STRESS( 1 ) = ESTRESS( I ) + COEF( 3 ) * ( (ONE-COEF( 1 ) ) *
+ DSTRAN( 1 ) + COEF( 1 ) * DSTRAN( 2 ) )
C
      STRESS( 2 ) = ESTRESS( I ) + COEF( 3 ) * ( (ONE-COEF( 1 ) ) *
+ DSTRAN( 2 ) + COEF( 1 ) * DSTRAN( 1 ) )
C
      STRESS( 3 ) = ESTRESS( I ) + COEF( 3 ) * ( COEF( 1 ) * DSTRAN( 1 )
+ + COEF( 1 ) * DSTRAN( 2 ) )
C
      STRESS( 4 ) = ESTRESS( I ) + DSTRAN( 4 ) *
+ COEF( 2 ) / ( TWO * (ONE+COEF( 1 ) ) )
C
C --- CALCULATING THE STRESSES
C
C --- VON MISES
C
      MISES = SQRT( STRESS( 1 )**TWO + STRESS( 2 )**TWO +
+ STRESS( 3 )**TWO - STRESS( 1 )*STRESS( 2 ) - STRESS(1)*STRESS(3)

```

```

+ - STRESS( 2 )*STRESS( 3 ) + 3*STRESS( 4 )**TWO )
C
C --- RE-DEFINING THE SOLUTION-DEPENDENT STATE VARIABLE FIELDS
C
DO I = 1 , NTENS
STATEV( I ) = STRESS( I )
END DO
STATEV( 5 ) = MISES
C --- IF STATEMENT IS ADDED TO AVOID THE FIRST ITERATION OF UMAT THAT GIVES
THE ZERO STRESS
IF ((NOEL.EQ.1).AND.(NPT.EQ.1)) THEN
OPEN (UNIT=10, FILE='C:\Temp\directory\Stress.dat',
+ STATUS='REPLACE')
ELSE
OPEN (UNIT=10, FILE='C:\Temp\directory\Stress.dat',
+ STATUS='OLD', POSITION='APPEND')
END IF
WRITE (10,*) STATEV( 5 ), noel,npt
CLOSE (10)
C --- UPDATING THE JACOBIAN MATRIX FOR ACCELERATING CONVERGENCE
DO I = 1 , NTENS
DO J = 1 , NTENS
DDSDDE(I , J) = ZERO
END DO
END DO
DDSDDE(1 , 1) = COEF(3) * (ONE-COEF( 1 ))
DDSDDE(1 , 2) = COEF(3) * COEF( 1 )
DDSDDE(2 , 1) = DDSDDE (1 , 2)
DDSDDE(2 , 2) = DDSDDE (1 , 1)
DDSDDE(3 , 1) = DDSDDE (1 , 2)
DDSDDE(3 , 2) = DDSDDE (3 , 1)
DDSDDE(4 , 4) = COEF( 2 ) / (TWO*(ONE+COEF( 1 )))
RETURN
END
C =====
C I I

```

```
C I THIS SUBROUTINE IS CALLED BY ABAQUS AND USED TO DEFINE INITIAL I
C I SOLUTION-DEPENDENT STATE VARIABLE FIELDS, WHICH IS CALLED I
C I WHENEVER THE "*INITIAL CONDITIONS, TYPE=SOLUTION, USER" OPTION I
C I IS USED. I
C I HERE THE STATE VARIABLES ARE INITIALIZED I
C I I
C =====
```

```
SUBROUTINE SDVINI (STATEV, COORDS, NSTATV, NCRDS, NOEL, NPT,  
1 LAYER, KSPT)  
INCLUDE 'ABA_PARAM.INC'  
DIMENSION STATEV (NSTATV) , COORDS (NCRDS)  
DATA ZERO /0.0D0/  
DO I = 1 , NSTATV  
STATEV ( I ) = ZERO  
END DO  
RETURN  
END
```

8.2 Appendix B: MATLAB function files used for MADS in Chapter 4

```
%*****
% User-supplied function for writing an Abaqus journal file with specifying
% the design variables, submitting the script to Abaqus solver, and
% importing results into MATLAB for post processing.
%*****
%           Written by : Ammar Alsheghri , McGill University           %
%*****

function [fx,cx] = myproblem(x)
T = x(1); % Thickness
An = x(2); % Angle
L = x(3); % Length

%%%%%%%%%%%%%%%%%%%%%%%%%%%%%%%%%%%%%%%%%%%%%%%%%%%%%%%%%%%%%%%%%%%%%%%%
%% Write Abaqus journal file to be used with the optimization algorithm %%
fileID = fopen('runfile.py','w');
fprintf(fileID,'from abaqus import *\n');
fprintf(fileID,'from abaqusConstants import *\n');
fprintf(fileID,'from caeModules import *\n');
fprintf(fileID,'from driverUtils import executeOnCaeStartup\n');
fprintf(fileID,'executeOnCaeStartup()\n');
fprintf(fileID,'openMdb(''MyModel.cae'')\n');
fprintf(fileID,'p = mdb.models[''Model-1''].parts[''Part-CoCr'']\n');
fprintf(fileID,'s = p.features[''Shell planar-1''].sketch\n');
fprintf(fileID,'mdb.models[''Model-1''].ConstrainedSketch(name='''__edit__'',
objectToCopy=s)\n');
fprintf(fileID,'s1 = mdb.models[''Model-1''].sketches['''__edit__'']\n');
fprintf(fileID,'g, v, d, c = s1.geometry, s1.vertices, s1.dimensions,
s1.constraints\n');
fprintf(fileID,'s1.setPrimaryObject(option=SUPERIMPOSE)\n');
fprintf(fileID,'p.projectReferencesOntoSketch(sketch=s1,\n');
fprintf(fileID,'    upToFeature=p.features[''Shell planar-1''],
filter=COPLANAR_EDGES)\n');
%%%%%%%%%%%%%%%%%%%%%%%%%%%%%%%%%%%%%%%%%%%%%%%%%%%%%%%%%%%%%%%%%%%%%%%%
%% Specifying design variables %%%%%%%%%%%%%%%%%%%%%%%%%%%%%%%%%%%%%%%%%%%%%%%%%%%%%%%%%%%%%%%%%%%%%%%%%
fprintf(fileID,'d[36].setValues(value=%d, )\n',L);
fprintf(fileID,'d[35].setValues(value=%d, )\n',An);
fprintf(fileID,'d[26].setValues(value=%d, )\n',T);
```

```

fprintf(fileID, 'd[27].setValues(value=%d, )\n',T);
fprintf(fileID, 's1.unsetPrimaryObject()\n');
fprintf(fileID, 'p = mdb.models[''Model-1''].parts[''Part-CoCr'']\n');
fprintf(fileID, 'p.features[''Shell planar-1''].setValues(sketch=s1)\n');
fprintf(fileID, 'del mdb.models[''Model-1''].sketches[''__edit__']\n');
fprintf(fileID, 'p = mdb.models[''Model-1''].parts[''Part-CoCr'']\n');
fprintf(fileID, 'p.regenerate()\n');
fprintf(fileID, 'p1 = mdb.models[''Model-1''].parts[''Part-PMMA'']\n');
fprintf(fileID, 'session.viewports[''Viewport:
1''].setValues(displayedObject=p1)\n');
fprintf(fileID, 'p = mdb.models[''Model-1''].parts[''Part-PMMA'']\n');
fprintf(fileID, 's = p.features[''Shell planar-1''].sketch\n');
fprintf(fileID, 'mdb.models[''Model-1''].ConstrainedSketch(name='''__edit__'',
objectToCopy=s)\n');
fprintf(fileID, 's2 = mdb.models[''Model-1''].sketches[''__edit__']\n');
fprintf(fileID, 'g, v, d, c = s2.geometry, s2.vertices, s2.dimensions,
s2.constraints\n');
fprintf(fileID, 's2.setPrimaryObject(option=SUPERIMPOSE)\n');
fprintf(fileID, 'p.projectReferencesOntoSketch(sketch=s2,\n');
fprintf(fileID, '    upToFeature=p.features[''Shell planar-1''],
filter=COPLANAR_EDGES)\n');
%% Specifying design variables %%%%%%%%%%%%%%%%%%%%%%%%%%%%%%%%%%%%%%%%%%%
fprintf(fileID, 'd[14].setValues(value=%d, )\n',L);
fprintf(fileID, 'd[13].setValues(value=%d, )\n',An);
fprintf(fileID, 'd[4].setValues(value=%d, )\n',T);
fprintf(fileID, 's2.unsetPrimaryObject()\n');
fprintf(fileID, 'p = mdb.models[''Model-1''].parts[''Part-PMMA'']\n');
fprintf(fileID, 'p.features[''Shell planar-1''].setValues(sketch=s2)\n');
fprintf(fileID, 'del mdb.models[''Model-1''].sketches[''__edit__']\n');
fprintf(fileID, 'p = mdb.models[''Model-1''].parts[''Part-PMMA'']\n');
fprintf(fileID, 'p.regenerate()\n');
fprintf(fileID, 'a = mdb.models[''Model-1''].rootAssembly\n');
fprintf(fileID, 'a.regenerate()\n');
fprintf(fileID, 'a = mdb.models[''Model-1''].rootAssembly\n');
fprintf(fileID, 'a = mdb.models[''Model-1''].rootAssembly\n');
fprintf(fileID, 'partInstances =(a.instances[''Part-CoCr-1''],
a.instances[''Part-PMMA-1''], )\n');

```

```

fprintf(fileID, 'a.generateMesh(regions=partInstances)\n');
fprintf(fileID, 'mdb.jobs[''Job-1''].submit(consistencyChecking=OFF)\n');
fprintf(fileID, 'mdb.save()\n');
fclose(fileID);

%% Run Abaqus Job without generating CAE %%%%%%%%%%%%%%%%%%%%%%%%%%%%%%%%%%%%%%%%%%%%%%%%%%%%%%%%%%%%%%%%%%%%%%%%%
dos('abaqus cae nogui=runfile')

% Message to indicate the progress and track errors
Progress = 'myfile.py is generated and called'

%% ===== Read Output from ODB file =====
% Use python scripts to read the required output from the ODB file and
% write the output into .dat files.
% To read Nodal Separations
dos('abaqus python getOutput-SepNodes_Disp.py')
% To read Maximum Mises Stress in Polymer part
dos('abaqus python getStressPolymer.py')
% Max Mises in Metal
dos('abaqus python getStressMetal.py')
% To read Reaction Forces
dos('abaqus python getOutput-RF.py')
% To read Nodal Separations
dos('abaqus python getOutput-TopNodes_Disp.py')
%% ===== Save outputs into MATLAB for post processing =====
% Read the outputs from the .dat file into MATLAB
fileID = fopen('MisesMetal.dat', 'r');
MisesMetal= fscanf(fileID, '%f');
MisesMetal=mean(MisesMetal)
fileID = fopen('MisesPolymer.dat', 'r');
Mises_Polymer= fscanf(fileID, '%f');
MaxMises_Polymer=mean(Mises_Polymer)
fileID = fopen('SepNodesDisp.dat', 'r');
C = fscanf(fileID, '%f', [2 Inf]); C = C';
SepNodeDisp= C(:,2);
Ave_SepNodeDisp = mean(SepNodeDisp);
fileID = fopen('TopNodesDisp.dat', 'r');
A = fscanf(fileID, '%f', [2 Inf]); A = A';

```

```

TopNodeDisp = A(:,2);
Ave_TopNodeDisp = mean(TopNodeDisp);
fileID = fopen('RF.dat','r');
B = fscanf(fileID,'%f',[2 Inf]); B = B';
RF = B(:,2);
Sum_RF = sum(RF);
% Calculate the stiffness
Stiffness = Sum_RF./Ave_TopNodeDisp.*(-1);
% Display the values for design variable while executing the code
T = T
An = An
L = L
%%
fx = 1/Stiffness
cx(1) = MaxMises_Polymer./40 - 1
cx(2) = MisesMetal./400 - 1
cx(3) = Ave_SepNodeDisp./0.006 - 1
% Save results in a text file
fileID = fopen('results.txt','w');
fprintf(fileID, 'Design Variables\n\n');
fprintf(fileID,'%f %f %f\n\n',T, An, L );
fprintf(fileID, 'MaxMises_Polymer\n');
fprintf(fileID,'%f\n\n',MaxMises_Polymer);
fprintf(fileID, 'MisesMetal\n');
fprintf(fileID,'%f\n\n', MisesMetal);
fprintf(fileID, 'Ave_SepNodeDisp\n');
fprintf(fileID,'%f\n\n', Ave_SepNodeDisp );
fprintf(fileID, 'Stiffness\n');
fprintf(fileID,'%f\n',1/fx);
fclose(fileID);
%
return

%*****

```

```

% User-supplied function for defining the following variables:
%   A = Coefficient matrix for bound and linear constraints
%   l = Lower bounds for A*x for any iterate x
%   u = Upper bounds for A*x for any iterate x
%*****
function [A,l,u] = myproblem_Omega(n)
A = eye(n);
l = [0.35;50;0.5];
u = [0.55;80;2];
return

%*****
% User-supplied function for defining the initial values for the three
% design variables
%*****
function iterate = myproblem_x0
iterate(1).x = [0.5;75;1.5];
iterate(1).p = [136];
return;

```

9 References

- [1] J. Wu, Topology optimization studies for light weight acoustic panels, Master's dissertation, University of Toronto, Toronto, ON (2016).
- [2] A.S. Dalaq, D.W. Abueidda, R.K.A. Al-Rub, Mechanical properties of 3D printed interpenetrating phase composites with novel architected 3D solid-sheet reinforcements, *Composites Part A: Applied Science and Manufacturing* 84 (2016) 266-280.
- [3] X. Wang, S. Xu, S. Zhou, W. Xu, M. Leary, P. Choong, M. Qian, M. Brandt, Y.M. Xie, Topological design and additive manufacturing of porous metals for bone scaffolds and orthopaedic implants: A review, *Biomaterials* 83 (2016) 127-141.
- [4] N. Hu, P. Feng, G. Dai, The gift from nature: bio-inspired strategy for developing innovative bridges, *Journal of Bionic Engineering* 10(4) (2013) 405-414.
- [5] L.J. Bonderer, A.R. Studart, L.J. Gauckler, Bioinspired design and assembly of platelet reinforced polymer films, *Science* 319(5866) (2008) 1069-1073.
- [6] F. Barthelat, H. Tang, P. Zavattieri, C.-M. Li, H.D. Espinosa, On the mechanics of mother-of-pearl: a key feature in the material hierarchical structure, *Journal of the Mechanics and Physics of Solids* 55(2) (2007) 306-337.
- [7] R. Huang, M. Riddle, D. Graziano, J. Warren, S. Das, S. Nimbalkar, J. Cresko, E. Masanet, Energy and emissions saving potential of additive manufacturing: the case of lightweight aircraft components, *Journal of Cleaner Production* 135 (2016) 1559-1570.
- [8] S. Arabnejad, R.B. Johnston, J.A. Pura, B. Singh, M. Tanzer, D. Pasini, High-strength porous biomaterials for bone replacement: A strategy to assess the interplay between cell morphology, mechanical properties, bone ingrowth and manufacturing constraints, *Acta biomaterialia* 30 (2016) 345-356.
- [9] J.W. Stansbury, M.J. Idacavage, 3D printing with polymers: Challenges among expanding options and opportunities, *Dental Materials* 32(1) (2016) 54-64.
- [10] G. Ma, L. Wang, A critical review of preparation design and workability measurement of concrete material for largescale 3D printing, *Frontiers of Structural and Civil Engineering* 12(3) (2018) 382-400.
- [11] B. Lu, D. Li, X. Tian, Development trends in additive manufacturing and 3D printing, *Engineering* 1(1) (2015) 85-89.
- [12] M.F. Ashby, D. Cebon, Materials selection in mechanical design, *Le Journal de Physique IV* 3(C7) (1993) C7-1-C7-9.
- [13] D. Melancon, Z. Bagheri, R. Johnston, L. Liu, M. Tanzer, D. Pasini, Mechanical characterization of structurally porous biomaterials built via additive manufacturing: experiments, predictive models, and design maps for load-bearing bone replacement implants, *Acta biomaterialia* 63 (2017) 350-368.
- [14] M.P. Bendsøe, N. Kikuchi, Generating optimal topologies in structural design using a homogenization method, *Computer methods in applied mechanics and engineering* 71(2) (1988) 197-224.

- [15] Y.M. Xie, G.P. Steven, A simple evolutionary procedure for structural optimization, *Computers & structures* 49(5) (1993) 885-896.
- [16] A. Baumgartner, L. Harzheim, C. Mattheck, SKO (soft kill option): the biological way to find an optimum structure topology, *International Journal of Fatigue* 14(6) (1992) 387-393.
- [17] U.G. Wegst, H. Bai, E. Saiz, A.P. Tomsia, R.O. Ritchie, Bioinspired structural materials, *Nature materials* 14(1) (2015) 23-36.
- [18] S. Binitha, S.S. Sathya, A survey of bio inspired optimization algorithms, *International journal of soft computing and engineering* 2(2) (2012) 137-151.
- [19] J.-H. Zhu, W.-H. Zhang, L. Xia, Topology optimization in aircraft and aerospace structures design, *Archives of Computational Methods in Engineering* 23(4) (2016) 595-622.
- [20] K. Maute, O. Sigmund, Topology optimization approaches: A comparative review, *Structural and Multidisciplinary Optimization* 6 (2013).
- [21] L. Shi, H. Li, A. Fok, C. Ucer, H. Devlin, K. Horner, Shape optimization of dental implants, *The International journal of oral & maxillofacial implants* 22(6) (2006) 911-920.
- [22] C.-L. Chang, C.-S. Chen, C.-H. Huang, M.-L. Hsu, Finite element analysis of the dental implant using a topology optimization method, *Medical engineering & physics* 34(7) (2012) 999-1008.
- [23] M. Lawry, K. Maute, Level set topology optimization of problems with sliding contact interfaces, *Structural and Multidisciplinary Optimization* 52(6) (2015) 1107-1119.
- [24] M.P. Bendsoe, O. Sigmund, *Topology optimization, Theory, Methods, and Applications* (2003).
- [25] J. Patel, S.-K. Choi, Classification approach for reliability-based topology optimization using probabilistic neural networks, *Structural and Multidisciplinary Optimization* 45(4) (2012) 529-543.
- [26] A.G. Evans, J.W. Hutchinson, N.A. Fleck, M. Ashby, H. Wadley, The topological design of multifunctional cellular metals, *Progress in Materials Science* 46(3-4) (2001) 309-327.
- [27] O. Sigmund, A 99 line topology optimization code written in Matlab, *Structural and multidisciplinary optimization* 21(2) (2001) 120-127.
- [28] K. Svanberg, The method of moving asymptotes—a new method for structural optimization, *International journal for numerical methods in engineering* 24(2) (1987) 359-373.
- [29] C. Mattheck, *Design in nature: learning from trees*, Springer Science & Business Media 1998.
- [30] Y. Yoon, X. Sun, J.-K. Huang, G. Hou, K. Rechowicz, F.D. McKenzie, Designing natural-tooth-shaped dental implants based on soft-kill option optimization, *Computer-Aided Design and Applications* 10(1) (2013) 59-72.
- [31] L. Shi, A.S. Fok, A. Qualtrough, A two-stage shape optimization process for cavity preparation, *dental materials* 24(11) (2008) 1444-1453.
- [32] G. Couegnat, S.L. Fok, J.E. Cooper, A.J. Qualtrough, Structural optimization of dental restorations using the principle of adaptive growth, *Dental Materials* 22(1) (2006) 3-12.

- [33] C. Mattheck, S. Burkhardt, A new method of structural shape optimization based on biological growth, *International Journal of Fatigue* 12(3) (1990) 185-190.
- [34] S.J. Hollister, Porous scaffold design for tissue engineering, *Nature materials* 4(7) (2005) 518.
- [35] N. Chandra, H. Li, C. Shet, H. Ghonem, Some issues in the application of cohesive zone models for metal–ceramic interfaces, *International Journal of Solids and Structures* 39(10) (2002) 2827-2855.
- [36] A.A. Alsheghri, R.K.A. Al-Rub, Thermodynamic-based cohesive zone healing model for self-healing materials, *Mechanics Research Communications* 70 (2015) 102-113.
- [37] A.A. Alsheghri, R.K.A. Al-Rub, Finite element implementation and application of a cohesive zone damage-healing model for self-healing materials, *Engineering Fracture Mechanics* 163 (2016) 1-22.
- [38] B. Blackman, H. Hadavinia, A.J. Kinloch, J. Williams, The use of a cohesive zone model to study the fracture of fibre composites and adhesively-bonded joints, *International Journal of Fracture* 119(1) (2003) 25-46.
- [39] C. Mattheck, Engineering components grow like trees, *Materialwissenschaft und Werkstofftechnik* 21(4) (1990) 143-168.
- [40] T.M. Keaveny, E.F. Morgan, G.L. Niebur, O.C. Yeh, Biomechanics of trabecular bone, *Annual Review of Biomedical Engineering* 3(1) (2001) 307-333.
- [41] E. Seeman, P.D. Delmas, Bone quality—the material and structural basis of bone strength and fragility, *New England Journal of Medicine* 354(21) (2006) 2250-2261.
- [42] N. Reznikov, J. Steele, P. Fratzl, M. Stevens, A materials science vision of extracellular matrix mineralization, *Nature Reviews Materials* 1(8) (2016) 16041.
- [43] J. Currey, Bone strength: what are we trying to measure?, *Calcified Tissue International* 68(4) (2001) 205-210.
- [44] W.-L. Hsu, C.-Y. Chen, J.-Y. Tsao, R.-S. Yang, Balance control in elderly people with osteoporosis, *Journal of the Formosan Medical Association* 113(6) (2014) 334-339.
- [45] N. Reznikov, C. Phillips, M. Cooke, A. Garbout, F. Ahmed, M.M. Stevens, Functional adaptation of the calcaneus in historical foot binding, *Journal of Bone and Mineral Research* 32(9) (2017) 1915-1925.
- [46] N. Reznikov, A.A. Alsheghri, N. Piche, M. Gendron, C. Desrosiers, I. Morozova, J.M.S. Siles, D.G.-. Quevedo, I. Tamimi, J. Song, F. Tamimi, Altered topological blueprint of trabecular bone associates with skeletal pathology in humans, *Bone Reports* (In press) (2020).
- [47] M.L. Buxsein, S.K. Boyd, B.A. Christiansen, R.E. Guldberg, K.J. Jepsen, R. Müller, Guidelines for assessment of bone microstructure in rodents using micro-computed tomography, *Journal of Bone and Mineral Research* 25(7) (2010) 1468-1486.
- [48] J.D. Currey, *Bones: structure and mechanics*, Princeton University Press 2006.
- [49] J. Wolff, *Das Gesetz der Transformation der Knochen*, A Hirshwald 1 (1892) 1-152.

- [50] I.G. Jang, I.Y. Kim, Computational study of Wolff's law with trabecular architecture in the human proximal femur using topology optimization, *Journal of Biomechanics* 41(11) (2008) 2353-2361.
- [51] A. Tovar, W. Quevedo, N. Patel, J. Renaud, Hybrid cellular automata with local control rules: a new approach to topology optimization inspired by bone functional adaptation, *Proceedings of the 6th World Congress on Structural and Multidisciplinary Optimization (WCSMO6)*. Rio de Janeiro, Brazil, 2005.
- [52] F. Naddeo, N. Cappetti, A. Naddeo, Novel "load adaptive algorithm based" procedure for 3D printing of cancellous bone-inspired structures, *Composites Part B: Engineering* 115 (2017) 60-69.
- [53] A. Tovar, G. Niebur, M. Sen, J. Renaud, B. Sanders, Bone structure adaptation as a cellular automaton optimization process, 45th AIAA/ASME/ASCE/AHS/ASC Structures, Structural Dynamics & Materials Conference, 2004, p. 1914.
- [54] J. Wang, *Trabecular topology: computational structural design inspired by bone remodeling*, Massachusetts Institute of Technology, 2017.
- [55] A. Nazir, K.M. Abate, A. Kumar, J.-Y. Jeng, A state-of-the-art review on types, design, optimization, and additive manufacturing of cellular structures, *The International Journal of Advanced Manufacturing Technology* (2019) 1-22.
- [56] R.M. Gorgularslan, U.N. Gandhi, R. Mandapati, S.-K. Choi, Design and fabrication of periodic lattice-based cellular structures, *Computer-Aided Design and Applications* 13(1) (2016) 50-62.
- [57] G. Rozvany, M. Bendsee, Addendum-Layout optimization of structures, *Applied Mechanics Reviews* 48(2) (1995) 41-119.
- [58] L.J. Gibson, M.F. Ashby, *Cellular solids: structure and properties*, Cambridge university press 1999.
- [59] O. Al-Ketan, R. Rowshan, R.K.A. Al-Rub, Topology-mechanical property relationship of 3D printed strut, skeletal, and sheet based periodic metallic cellular materials, *Additive Manufacturing* 19 (2018) 167-183.
- [60] V.S. Deshpande, N.A. Fleck, M.F. Ashby, Effective properties of the octet-truss lattice material, *Journal of the Mechanics and Physics of Solids* 49(8) (2001) 1747-1769.
- [61] R.M. Sullivan, L.J. Ghosn, B.A. Lerch, A general tetrakaidecahedron model for open-celled foams, *International Journal of Solids and Structures* 45(6) (2008) 1754-1765.
- [62] P. Terriault, V. Brailovski, Modeling and simulation of large, conformal, porosity-graded and lightweight lattice structures made by additive manufacturing, *Finite Elements in Analysis and Design* 138 (2018) 1-11.
- [63] S. Khaderi, V. Deshpande, N. Fleck, The stiffness and strength of the gyroid lattice, *International Journal of Solids and Structures* 51(23-24) (2014) 3866-3877.
- [64] V. Deshpande, M. Ashby, N. Fleck, Foam topology: bending versus stretching dominated architectures, *Acta materialia* 49(6) (2001) 1035-1040.
- [65] D. Weaire, *The Kelvin Problem*, CRC Press 1997.

- [66] L. Mullen, R.C. Stamp, W.K. Brooks, E. Jones, C.J. Sutcliffe, Selective Laser Melting: A regular unit cell approach for the manufacture of porous, titanium, bone in-growth constructs, suitable for orthopedic applications, *Journal of Biomedical Materials Research Part B: Applied Biomaterials: An Official Journal of The Society for Biomaterials, The Japanese Society for Biomaterials, and The Australian Society for Biomaterials and the Korean Society for Biomaterials* 89(2) (2009) 325-334.
- [67] D.W. Abueidda, R.K.A. Al-Rub, A.S. Dalaq, D.-W. Lee, K.A. Khan, I. Jasiuk, Effective conductivities and elastic moduli of novel foams with triply periodic minimal surfaces, *Mechanics of Materials* 95 (2016) 102-115.
- [68] A. International, F2792-12a-Standard Terminology for Additive Manufacturing Technologies, *Rapid Manuf. Assoc.* (2013) 10-12.
- [69] S. Bose, S. Vahabzadeh, A. Bandyopadhyay, Bone tissue engineering using 3D printing, *Materials today* 16(12) (2013) 496-504.
- [70] O. Alageel, M.N. Abdallah, A. Alsheghri, J. Song, E. Caron, F. Tamimi, Removable partial denture alloys processed by laser-sintering technique, *Journal of Biomedical Materials Research Part B: Applied Biomaterials* 106(3) (2018) 1174-1185.
- [71] R. Soenen, G.J. Olling, *Advanced CAD/CAM Systems: State-of-the-art and Future Trends in Feature Technology*, Springer 2016.
- [72] G. Davidowitz, P.G. Kotick, The Use of CAD/CAM in Dentistry, *Dental Clinics of North America* 55(3) (2011) 559-570.
- [73] R. van Noort, The future of dental devices is digital, *Dental Materials* 28(1) (2012) 3-12.
- [74] R.J. Williams, R. Bibb, D. Eggbeer, J. Collis, Use of CAD/CAM technology to fabricate a removable partial denture framework, *The Journal of Prosthetic Dentistry* 96(2) (2006) 96-99.
- [75] A. Örtorp, D. Jönsson, A. Mouhsen, P. Vult von Steyern, The fit of cobalt–chromium three-unit fixed dental prostheses fabricated with four different techniques: A comparative in vitro study, *Dental Materials* 27(4) (2011) 356-363.
- [76] M.C. Bortoluzzi, J. Traebert, R. Lasta, T.N. Da Rosa, D.L. Capella, A.A. Presta, Tooth loss, chewing ability and quality of life, *Contemporary Clinical Dentistry* 3(4) (2012) 393-397.
- [77] A.E. Gerritsen, P.F. Allen, D.J. Witter, E.M. Bronkhorst, N.H. Creugers, Tooth loss and oral health-related quality of life: a systematic review and meta-analysis, *Health and quality of life outcomes* 8(1) (2010) 1.
- [78] D.A. Felton, Edentulism and comorbid factors, *Journal of Prosthodontics* 18(2) (2009) 88-96.
- [79] E.B. Øzhayat, K. Gotfredsen, Effect of treatment with fixed and removable dental prostheses. An oral health-related quality of life study, *Journal of oral rehabilitation* 39(1) (2012) 28-36.
- [80] R.W. Loney, *Removable partial denture manual*, (2011).
- [81] A.B. Carr, D.T. Brown, *McCracken's removable partial prosthodontics*, Twelfth ed., Elsevier Health Sciences, St. Louis, 2010.
- [82] K.J. Anusavice, C. Shen, H.R. Rawls, *Phillips' science of dental materials*, Twelfth ed., Saunders, an imprint of Elsevier Inc., Philadelphia, 2013.

- [83] M. Saito, K. Notani, Y. Miura, T. Kawasaki, Complications and failures in removable partial dentures: a clinical evaluation, *Journal of Oral Rehabilitation* 29(7) (2002) 627-633.
- [84] J.F. McCabe, A.W. Walls, *Applied dental materials*, John Wiley & Sons 2013.
- [85] F. Tannous, M. Steiner, R. Shahin, M. Kern, Retentive forces and fatigue resistance of thermoplastic resin clasps, *Dental Materials* 28(3) (2012) 273-278.
- [86] E. Hofmann, M. Behr, G. Handel, Frequency and costs of technical failures of clasp-and double crown-retained removable partial dentures, *Clinical oral investigations* 6(2) (2002) 104-108.
- [87] P.K. Vallittu, V.P. Lassila, R. Lappalainen, Evaluation of damage to removable dentures in two cities in Finland, *Acta Odontologica Scandinavica* 51(6) (1993) 363-369.
- [88] E. Nagai, K. Otani, Y. Satoh, S. Suzuki, Repair of denture base resin using woven metal and glass fiber: effect of methylene chloride pretreatment, *The Journal of prosthetic dentistry* 85(5) (2001) 496-500.
- [89] D. Lamb, B. Ellis, R. Van Noort, The fracture topography of acrylic dentures broken in service, *Biomaterials* 6(2) (1985) 110-112.
- [90] A. Hargreaves, The prevalence of fractured dentures. A survey, *British dental journal* 126(10) (1969) 451.
- [91] E. Budtz-Jørgensen, G. Bochet, M. Grundman, S. Borgis, Aesthetic considerations for the treatment of partially edentulous patients with removable dentures, *Practical periodontics and aesthetic dentistry: PPAD* 12(8) (2000) 765-72.
- [92] H. Maruyama, T. Hamano, C. Kishita, Y. Nishi, S. Kawamoto, E. Nagaoka, Stress Analysis of clasps made of glass fiber-reinforced composite material using three-dimensional finite element method: influence of shape in cross and longitudinal sections of circumferential clasp arms, *Dental materials journal* 26(4) (2007) 534-544.
- [93] A.J. Lewis, Failure of removable partial denture castings during service, *The Journal of Prosthetic Dentistry* 39(2) (1978) 147-149.
- [94] A. Chiba, K. Kumagai, N. Nomura, S. Miyakawa, Pin-on-disk wear behavior in a like-on-like configuration in a biological environment of high carbon cast and low carbon forged Co–29Cr–6Mo alloys, *Acta materialia* 55(4) (2007) 1309-1318.
- [95] S.-H. Sun, Y. Koizumi, S. Kurosu, Y.-P. Li, H. Matsumoto, A. Chiba, Build direction dependence of microstructure and high-temperature tensile property of Co–Cr–Mo alloy fabricated by electron beam melting, *Acta Materialia* 64 (2014) 154-168.
- [96] J.A. Warr, Numerical system of clasp design, *The Journal of Prosthetic Dentistry* 11(6) (1961) 1105-1111.
- [97] J. Warr, An analysis of clasp design in partial dentures, *Physics in medicine and biology* 3(3) (1959) 212.
- [98] P. Brockhurst, A new design for partial denture circumferential clasp arms, *Australian dental journal* 41(5) (1996) 317-323.

- [99] Y. Sato, K. Tsuga, Y. Abe, S. Asahara, Y. Akagawa, Analysis of stiffness and stress in I-bar clasps, *Journal of oral rehabilitation* 28(6) (2001) 596-600.
- [100] L. Sandu, F. Topala, S. Porojan, Stress distribution in retentive arms of combination clasps used on premolars, *Journal of Applied Biomaterials & Biomechanics* 8(2) (2010).
- [101] K. Shirasu, N. Wakabayashi, T. Yoneyama, Y. Igarashi, Non-linear finite element stress analysis of plastic deformation in Co–Cr wrought-wire clasps, *dental materials* 24(11) (2008) 1518-1524.
- [102] H. Morris, J. Farah, R. Craig, J. Hood, Stress distribution within circumferential clasp arms, *Journal of oral rehabilitation* 3(4) (1976) 387-394.
- [103] M. Šćepanović, L. Tihacek-Šojić, M. Tasić, R. Mitrović, A. Todorović, B. Trifković, Finite element analysis in defining the optimal shape and safety factor of retentive clasp arms of a removable partial denture, *Vojnosanitetski preglod* 70(11) (2013) 999-1005.
- [104] U. Darbar, R. Huggett, A. Harrison, Denture fracture--a survey, *British dental journal* 176(9) (1994) 342-345.
- [105] O. Alageel, A.A. Alsheghri, S. Algezani, E. Caron, F. Tamimi, Determining the retention of removable partial dentures, *The Journal of Prosthetic Dentistry* 122(1) (2019) 55-62. e3.
- [106] F. Beer, E.R. Jr. Johnston, J. DeWolf, D. Mazurek, *Mechanics of Materials*, Sixth ed., McGraw-Hill Education, New York, 2011.
- [107] R.G. Budynas, J.K. Nisbett, J.E. Shigley, *Shigley's mechanical engineering design*, McGraw-Hill, New York, 2011.
- [108] T.A. Imbery, E.G. Eshelman, Resin-bonded fixed partial dentures: a review of three decades of progress, *The Journal of the American Dental Association* 127(12) (1996) 1751-1760.
- [109] P. Vallittu, V. Lassila, Effect of metal strengthener's surface roughness on fracture resistance of acrylic denture base material, *Journal of oral rehabilitation* 19(4) (1992) 385-391.
- [110] G. Livaditis, V.P. Thompson, Etched castings: an improved retentive mechanism for resin-bonded retainers, *The Journal of prosthetic dentistry* 47(1) (1982) 52-58.
- [111] J.A. Dunny, G.E. King, Minor connector designs for anterior acrylic resin bases: a preliminary study, *The Journal of prosthetic dentistry* 34(5) (1975) 496-502.
- [112] M.G. Swenson, W.R. Laney, L.G. Terkla, *Partial dentures*, (1963) 134.
- [113] R.W. Dykema, D.M. Cunningham, J.F. Johnston, *Modern practice in removable partial prosthodontics*, Saunders 1969.
- [114] O.C. Applegate, *Essentials of removable partial denture prosthesis*, Saunders (WB) Co Ltd 1965.
- [115] A.R. Ruffino, Effect of steel strengtheners on fracture resistance of the acrylic resin complete denture base, *The Journal of Prosthetic Dentistry* 54(1) (1985) 75-78.
- [116] T. Ikeda, N. Wakabayashi, M. Ona, T. Ohyama, Effects of polymerization shrinkage on the interfacial stress at resin–metal joint in denture-base: a non-linear FE stress analysis, *Dental Materials* 22(5) (2006) 413-419.

- [117] H. Shimizu, T. Ikeda, N. Wakabayashi, T. Ohyama, Effect of metal strengthener length on stress distribution in acrylic denture bases: a finite element study, *Journal of oral rehabilitation* 31(9) (2004) 879-883.
- [118] T. Ikeda, H. Shimizu, N. Wakabayashi, T. Ohyama, Effect of cross section shape of metal strengthener on stress distribution in acrylic denture bases, *Prosthodontic Research & Practice* 3(1) (2004) 1-7.
- [119] D. Mahler, L. Terkla, Analysis of stress in dental structures, *Dent Clin North Am* 2 (1958) 789-98.
- [120] M. Preetham, Metal mesh dentures-A case report, *INDIAN JOURNAL OF DENTAL RESEARCH* 2012 (2012).
- [121] P.K. Vallittu, V.P. Lassila, R. Lappalainen, Transverse strength and fatigue of denture acrylic-glass fiber composite, *Dental Materials* 10(2) (1994) 116-121.
- [122] A.M. El-Sheikh, S.B. Al-Zahrani, Causes of denture fracture: A survey, *Saudi dental journal* 18(3) (2006) 149-154.
- [123] E. Lin, Y. Li, C. Ortiz, M.C. Boyce, 3D printed, bio-inspired prototypes and analytical models for structured suture interfaces with geometrically-tuned deformation and failure behavior, *Journal of the Mechanics and Physics of Solids* 73 (2014) 166-182.
- [124] M.A. Meyers, P.-Y. Chen, A.Y.-M. Lin, Y. Seki, Biological materials: structure and mechanical properties, *Progress in Materials Science* 53(1) (2008) 1-206.
- [125] J.W. Dunlop, R. Weinkamer, P. Fratzl, Artful interfaces within biological materials, *Materials Today* 14(3) (2011) 70-78.
- [126] F. Barthelat, Architected materials in engineering and biology: fabrication, structure, mechanics and performance, *International Materials Reviews* 60(8) (2015) 413-430.
- [127] F. Barthelat, Z. Yin, M.J. Buehler, Structure and mechanics of interfaces in biological materials, *Nature Reviews Materials* 1 (2016) 16007.
- [128] P. Fratzl, Biomimetic materials research: what can we really learn from nature's structural materials?, *Journal of the Royal Society Interface* 4(15) (2007) 637-642.
- [129] Y. Zhang, H. Yao, C. Ortiz, J. Xu, M. Dao, Bio-inspired interfacial strengthening strategy through geometrically interlocking designs, *Journal of the mechanical behavior of biomedical materials* 15 (2012) 70-77.
- [130] L. Xu, H. Kuai, S. Sengupta, Dissimilar material joints with and without free-edge stress singularities: Part I. A biologically inspired design, *Experimental mechanics* 44(6) (2004) 608-615.
- [131] H. Bruck, G. Fowler, S. Gupta, T. Valentine, Using geometric complexity to enhance the interfacial strength of heterogeneous structures fabricated in a multi-stage, multi-piece molding process, *Experimental Mechanics* 44(3) (2004) 261-271.
- [132] S.A. Khanoki, D. Pasini, Multiscale design and multiobjective optimization of orthopedic hip implants with functionally graded cellular material, *Journal of biomechanical engineering* 134(3) (2012) 031004.

- [133] A. Myśliński, M. Wróblewski, Structural optimization of contact problems using Cahn–Hilliard model, *Computers & Structures* (2016).
- [134] J.N. Reddy, *An introduction to the finite element method*, New York (1993).
- [135] S. Bhavikatti, *Finite element analysis*, New Age International 2005.
- [136] S.K. Hummel, M.A. Wilson, V.A. Marker, M.E. Nunn, Quality of removable partial dentures worn by the adult US population, *The Journal of prosthetic dentistry* 88(1) (2002) 37-43.
- [137] T.E. Donovan, K. Derbabian, L. Kaneko, R. Wright, Esthetic considerations in removable prosthodontics, *Journal of Esthetic and Restorative Dentistry* 13(4) (2001) 241-253.
- [138] L. Sandu, N. Faur, C. Bortun, Finite element stress analysis and fatigue behavior of cast circumferential clasps, *The Journal of prosthetic dentistry* 97(1) (2007) 39-44.
- [139] B. Almufleh, E. Emami, O. Alageel, F. de Melo, F. Seng, E. Caron, S.A. Nader, A. Al-Hashedi, R. Albuquerque, J. Feine, Patient satisfaction with laser-sintered removable partial dentures: a crossover pilot clinical trial, *The Journal of prosthetic dentistry* 119(4) (2018) 560-567. e1.
- [140] J. Davenport, R. Basker, J. Heath, J. Ralph, P. Glantz, P. Hammond, Clasp design, *British dental journal* 190(2) (2001) 71-81.
- [141] D.N. Firtell, Effect of clasp design upon retention of removable partial dentures, *The Journal of prosthetic dentistry* 20(1) (1968) 43-52.
- [142] E. Sun, Shear locking and hourglassing in msc nastran, abaqus, and ansys, *Msc software users meeting* (2006).
- [143] J.D. Stanitz, An analysis of the part played by the fluid film in denture retention, *The Journal of the American Dental Association* 37(2) (1948) 168-172.
- [144] P.-G. De Gennes, F. Brochard-Wyart, D. Quéré, *Capillarity and wetting phenomena: drops, bubbles, pearls, waves*, Springer Science & Business Media 2013.
- [145] M.D. Murray, B.W. Darvell, The evolution of the complete denture base. Theories of complete denture retention—a review. Part 4, *Australian dental journal* 38(6) (1993) 450-455.
- [146] J. Barber, A. Cardou, *Intermediate mechanics of materials*, *Applied Mechanics Reviews* 54 (2001) B104.
- [147] A.F.R. Abdel-Rahman, E.A.B. Salah, *Engineering Solid Mechanics: Fundamentals And Applications*, CRC Press, Boca Raton, Fl., 1999.
- [148] M. Ali, The measurement of co-efficient of friction between cast Co-Cr alloy and guiding plane materials - A pilot study. , *Pakistan Oral & Dent. Jr.* 22(1) (2002).
- [149] K.L. Ohashi, R.H. Dauskardt, Effects of fatigue loading and PMMA precoating on the adhesion and subcritical debonding of prosthetic-PMMA interfaces, *Journal of biomedical materials research* 51(2) (2000) 172-183.
- [150] 3TRPD, Material Specification Cobalt Chrome Alloy Co28Cr6Mo, <http://www.3trpd.co.uk/wp-content/uploads/2013/03/cobalt-chrome-alloy-co28-cr6mo-2012.pdf>, (accessed 13 Jan 2016).

- [151] R.C. Wheeler, A textbook of dental anatomy and physiology, WB Saunders 1950.
- [152] Y. Sato, K. Tsuga, Y. Abe, Y. Akagawa, Finite element analysis of the effect of vertical curvature on half-oval cast clasps, *Journal of oral rehabilitation* 26(7) (1999) 554-558.
- [153] A.A.A. Mahmoud, N. Wakabayashi, H. Takahashi, Prediction of permanent deformation in cast clasps for denture prostheses using a validated nonlinear finite element model, *Dental Materials* 23(3) (2007) 317-324.
- [154] D. Simulia, ABAQUS 6.13 User's manual, Dassault Systems Simulia Corporation, Johnston, RI, USA (2013).
- [155] D. Kim, C. Park, Y. Yi, L. Cho, Comparison of cast Ti-Ni alloy clasp retention with conventional removable partial denture clasps, *The Journal of prosthetic dentistry* 91(4) (2004) 374-382.
- [156] A. Takaichi, Suyalatu, T. Nakamoto, N. Joko, N. Nomura, Y. Tsutsumi, S. Migita, H. Doi, S. Kurosu, A. Chiba, N. Wakabayashi, Y. Igarashi, T. Hanawa, Microstructures and mechanical properties of Co-29Cr-6Mo alloy fabricated by selective laser melting process for dental applications, *Journal of the Mechanical Behavior of Biomedical Materials* 21 (2013) 67-76.
- [157] J.C. Davenport, R.M. Basker, J.R. Heath, J.P. Ralph, P.O. Glantz, *Prosthetics: Retention*, *Br Dent J* 189(12) (2000) 646-657.
- [158] S. Ramakrishna, J. Mayer, E. Wintermantel, K.W. Leong, Biomedical applications of polymer-composite materials: a review, *Composites science and technology* 61(9) (2001) 1189-1224.
- [159] M. Jasty, W. Maloney, C. Bragdon, D. O'connor, T. Haire, W. Harris, The initiation of failure in cemented femoral components of hip arthroplasties, *Bone & Joint Journal* 73(4) (1991) 551-558.
- [160] C.G. Mohler, C. Eugene, D.K. Collis, R.C. Johnston, Early loosening of the femoral component at the cement-prosthesis interface after total hip replacement, *Journal of Bone and Joint Surgery* 77(9) (1995) 1315-1322.
- [161] R. Gautam, R.D. Singh, V.P. Sharma, R. Siddhartha, P. Chand, R. Kumar, Biocompatibility of polymethylmethacrylate resins used in dentistry, *Journal of Biomedical Materials Research Part B: Applied Biomaterials* 100(5) (2012) 1444-1450.
- [162] J. Davies, W.H. Harris, Tensile bonding strength of the cement-prosthesis interface, *Orthopedics* 17(2) (1994) 171-173.
- [163] J. Watts, S. Leadley, J. Castle, C. Blomfield, Adsorption of PMMA on oxidized Al and Si substrates: An investigation by high-resolution X-ray photoelectron spectroscopy, *Langmuir* 16(5) (2000) 2292-2300.
- [164] O. Alageel, M.-N. Abdallah, Z.Y. Luo, J. Del-Rio-Highsmith, M. Cerruti, F. Tamimi, Bonding metals to poly (methyl methacrylate) using aryldiazonium salts, *Dental Materials* 31(2) (2015) 105-114.
- [165] Y. Tsuchimoto, Y. Yoshida, M. Atsushi, M. Nakamura, N. Nishiyama, B. Van Meerbeek, K. Suzuki, T. Kuboki, Effect of 4-MET-and 10-MDP-based primers on resin bonding to titanium, *Dental materials journal* 25(1) (2006) 120-124.

- [166] U. Gbureck, S. Grübel, R. Thull, J. Barralet, Modified PMMA cements for a hydrolysis resistant metal–polymer interface in orthopaedic applications, *Acta biomaterialia* 1(6) (2005) 671-676.
- [167] L.H. Sperling, Mechanical behavior of polymers. Introduction to physical polymer science, Fourth ed., John Wiley & Sons, New Jersey, 2005.
- [168] C.F. Lee, H.P. Pierpont, E.R. Strickler, The effect of bead attachment systems on casting patterns and resultant tensile bond strength of composite resin veneer cast restorations, *The Journal of prosthetic dentistry* 66(5) (1991) 623-630.
- [169] R.D. Crowninshield, J.D. Jennings, M.L. Laurent, W.J. Maloney, Cemented femoral component surface finish mechanics, *Clinical orthopaedics and related research* 355 (1998) 90-102.
- [170] P. Ausiello, A. Apicella, C.L. Davidson, Effect of adhesive layer properties on stress distribution in composite restorations—a 3D finite element analysis, *Dental Materials* 18(4) (2002) 295-303.
- [171] A. Lion, B. Yagimli, G. Baroud, U. Goerke, Constitutive modelling of PMMA-based bone cement: a functional model of viscoelasticity and its approximation for time domain investigations, *Archives of Mechanics* 60(3) (2008) 221-242.
- [172] W.L. Murphy, J. Black, G.W. Hastings, *Handbook of biomaterial properties*, (2016).
- [173] N. Nuno, M. Amabili, R. Groppetti, A. Rossi, Static coefficient of friction between Ti-6Al-4V and PMMA for cemented hip and knee implants, *Journal of biomedical materials research* 59(1) (2002) 191-200.
- [174] M.A. Abramson, C. Audet, J. Dennis, S. Le Digabel, *NOMADm Optimization Software*, 2015, <http://www.afit.edu/en/enc/Faculty/MAbramson/abramson.html>, (accessed on 26 June 2018).
- [175] C. Audet, J.E. Dennis Jr, Mesh adaptive direct search algorithms for constrained optimization, *SIAM Journal on optimization* 17(1) (2006) 188-217.
- [176] P.Y. Papalambros, D.J. Wilde, *Principles of optimal design: modeling and computation*, Cambridge university press 2000.
- [177] R. Van Noort, M.E. Barbour, *Introduction to Dental Materials*, Elsevier Health Sciences, St. Louis, 2013.
- [178] K. Brymora, J. Fouineau, A. Eddarir, F. Chau, N. Yaacoub, J.-M. Grenèche, J. Pinson, S. Ammar, F. Calvayrac, Grafting of diazonium salts on oxides surface: formation of aryl-O bonds on iron oxide nanoparticles, *Journal of Nanoparticle Research* 17(11) (2015) 438.
- [179] A. Kannarath, *Mimicking Nature: A Solution for Sustainable Development*, Partridge Publishing, India, 2014.
- [180] P.J. Hogarth, *The biology of mangroves and seagrasses*, Third ed., Oxford University Press, Oxford, 2015.
- [181] T.A. Osswald, *Understanding polymer processing: processes and governing equations*, Second ed., Carl Hanser Verlag GmbH Co KG, Munich, 2017.

- [182] A.R. Parkinson, R. Balling, J.D. Hedengren, Optimization methods for engineering design: Applications and Theory, Brigham Young University 2013.
- [183] S.A. Wainwright, W. Biggs, J. Gosline, J. Currey, Mechanical design in organisms, Princeton University Press 1982.
- [184] M.F. Ashby, The properties of foams and lattices, *Phil Trans: Math Phys Eng Sci* 364(1838) (2006) 15-30.
- [185] X. Zheng, H. Lee, T.H. Weisgraber, M. Shusteff, J. DeOtte, E.B. Duoss, J.D. Kunz, M.M. Biener, Q. Ge, J.A. Jackson, S.O. Kucheyev, N.X. Fang, C.M. Spadaccini, Ultralight, ultrastiff mechanical metamaterials, *Science* 344(6190) (2014) 1373-1377.
- [186] M. Kaur, T.G. Yun, S.M. Han, E. Thomas, W.S. Kim, 3D printed stretching-dominated micro-trusses, *Materials & Design* 134(15) (2017) 272-280.
- [187] S.C. Han, K. Kang, Another stretching-dominated micro-architected material, shellular, *Materials Today* 31 (2019) 31-38.
- [188] D. Thompson, A. Wentworth, *On growth and form*, 1917, Cambridge [Eng.]: University press. xv (1970).
- [189] S. Deshpande, A. Fleck, F. Ashby, Effective properties of the octet-truss lattice material, *Journal of the Mechanics and Physics of Solids* 49(8) (2001) 1747-1769.
- [190] E. van der Giessen, Bending Maxwell's rule, *Nature Physics* 7(12) (2011) 923-924.
- [191] D. Cvetkovic, I. Parmee, Evolutionary design and multi-objective optimization, 6th European Congress on Intelligent techniques and Soft Computing EUFIT'98, 1998.
- [192] P. Fratzl, R. Weinkamer, Nature's hierarchical materials, *Progress in materials Science* 52(8) (2007) 1263-1334.
- [193] J. Aizenberg, P. Fratzl, Biological and biomimetic materials, *Advanced Materials* 21(4) (2009) 387-388.
- [194] J. Currey, The many adaptations of bone, *Journal of biomechanics* 36(10) (2003) 1487-1495.
- [195] J.H.C. Lee, B. Ondruschka, L. Falland-Cheung, M. Scholze, N. Hammer, D.C. Tong, J.N. Waddell, An investigation on the correlation between the mechanical properties of human skull bone, its geometry, microarchitectural properties, and water content, *J Health Eng* 2019 (2019).
- [196] F. Acquaah, K.A. Robson Brown, F. Ahmed, N. Jeffery, R.L. Abel, Early trabecular development in human vertebrae: overproduction, constructive regression, and refinement, *Frontiers in endocrinology* 6 (2015) 67.
- [197] T.M. Ryan, G.E. Krovitz, Trabecular bone ontogeny in the human proximal femur, *Journal of human evolution* 51(6) (2006) 591-602.
- [198] C. Boyle, I.Y. Kim, Three-dimensional micro-level computational study of Wolff's law via trabecular bone remodeling in the human proximal femur using design space topology optimization, *Journal of biomechanics* 44(5) (2011) 935-942.
- [199] Y. Ben-Zvi, N. Reznikov, R. Shahar, S. Weiner, 3D architecture of trabecular bone in the pig mandible and femur: inter-trabecular angle distributions, *Frontiers in Materials* 4 (2017) 29.

- [200] N. Reznikov, H. Chase, Y.B. Zvi, V. Tarle, M. Singer, V. Brumfeld, R. Shahar, S. Weiner, Inter-trabecular angle: a parameter of trabecular bone architecture in the human proximal femur that reveals underlying topological motifs, *Acta biomaterialia* 44 (2016) 65-72.
- [201] X.-Y. Zhang, G. Fang, S. Leeftang, A.A. Zadpoor, J. Zhou, Topological design, permeability and mechanical behavior of additively manufactured functionally graded porous metallic biomaterials, *Acta biomaterialia* 84 (2019) 437-452.
- [202] S. Giannitelli, D. Accoto, M. Trombetta, A. Rainer, Current trends in the design of scaffolds for computer-aided tissue engineering, *Acta biomaterialia* 10(2) (2014) 580-594.
- [203] N. Reznikov, O.R. Boughton, S. Ghose, A.E. Weston, L. Collinson, G.W. Blunn, J.R. Jeffers, J.P. Cobb, M.M. Stevens, Individual response variations in scaffold-guided bone regeneration are determined by independent strain-and injury-induced mechanisms, *Biomaterials* 194 (2019) 183-194.
- [204] S. Ghose, N. Reznikov, O.R. Boughton, S. Babu, K.G. Ng, G. Blunn, J.P. Cobb, M.M. Stevens, J.R. Jeffers, The design and in vivo testing of a locally stiffness-matched porous scaffold, *Applied Materials Today* 15 (2019) 377-388.
- [205] H. Park, Polytope bounded Voronoi diagram in 2D and 3D, <https://www.github.com/hyongju/Polytope-bounded-Voronoi-diagram>, (accessed 5 Sep 2018).
- [206] L. Liu, P. Kamm, F. García-Moreno, J. Banhart, D. Pasini, Elastic and failure response of imperfect three-dimensional metallic lattices: the role of geometric defects induced by Selective Laser Melting, *Journal of the Mechanics and Physics of Solids* 107 (2017) 160-184.
- [207] M.d.s. Formlab, Materials data sheet, <https://archive-media.formlabs.com/upload/XL-DataSheet.pdf>, (accessed 22 June 2019).
- [208] P.K. Zysset, X.E. Guo, C.E. Hoffler, K.E. Moore, S.A. Goldstein, Elastic modulus and hardness of cortical and trabecular bone lamellae measured by nanoindentation in the human femur, *Journal of biomechanics* 32(10) (1999) 1005-1012.
- [209] D.L. Kopperdahl, T.M. Keaveny, Yield strain behavior of trabecular bone, *Journal of biomechanics* 31(7) (1998) 601-608.
- [210] A.S. Dalaq, D.W. Abueidda, R.K.A. Al-Rub, I.M. Jasiuk, Finite element prediction of effective elastic properties of interpenetrating phase composites with architected 3D sheet reinforcements, *International Journal of Solids and Structures* 83 (2016) 169-182.
- [211] A.A. Alshegri, O. Alageel, M.A. Mezour, B. Sun, S. Yue, F. Tamimi, J. Song, Bio-inspired and optimized interlocking features for strengthening metal/polymer interfaces in additively manufactured prostheses, *Acta biomaterialia* 80 (2018) 425-434.